REVIEW ARTICLE

Electromagnetic structure of the deuteron

R. Gilman[†‡] **and Franz Gross**[‡§]

[†] Rutgers University, 126 Frelinghuysen Rd, Piscataway, NJ 08855 USA

[‡] Jefferson Lab, 12000 Jefferson Ave, Newport News, VA 23606 USA

[§] College of William and Mary, Williamsburg, VA 23187 USA

E-mail: `gilman@jlab.org`, `gross@jlab.org`

Abstract. Recent measurements of the deuteron electromagnetic structure functions A, B, and T_{20} extracted from high energy elastic ed scattering, and the cross sections and asymmetries extracted from high energy photodisintegration $\gamma + d \rightarrow n + p$, are reviewed and compared to theory. The theoretical calculations range from nonrelativistic and relativistic models using the traditional meson and baryon degrees of freedom, to effective field theories, to models based on the underlying quark and gluon degrees of freedom of QCD, including nonperturbative quark cluster models and perturbative QCD. We review what has been learned from these experiments, and discuss why elastic ed scattering and photodisintegration seem to require very different theoretical approaches, even though they are closely related experimentally.

PACS numbers: 21.45.+v,25.20.-x,13.40.Gp, 24.70.+s

Contents

1. Introduction

The deuteron, the only $A = 2$ nucleus, provides the simplist microscopic test of the *conventional nuclear model*, a framework in which nuclei and nuclear interactions are explained as baryons interacting through the exchange of mesons. With improved nucleon-nucleon force models from the 1990s [1], and advances in our understanding of relativistic bound state techniques, more accurate calculations of deuteron structure are possible.

During the 1990s there have also been revolutionary improvements in our experimental knowledge of deuteron electromagnetic structure. The start of experiments at the Thomas Jefferson National Accelerator Facility (JLab) has now made available continuous high energy beams, with high currents and large polarization, along with new detector systems. Several experiments have now significantly extended the energy and momentum transfer range of deuteron electromagnetic studies, including A and t_{20} for elastic ed scattering, and photodisintegration cross sections and polarizations. Existing experimental proposals promise to continue this trend. Other laboratories have also made several important measurements, generally at lower momentum transfer.

In this context, a review of the deuteron electromagnetic studies, examining the current status of the agreement between experiments and theory, is appropriate. We attempt to cover our current knowledge of the deuteron electromagnetic structure, focussing on the recent JLab results, and prospects for the future. We do not consider experiments that use the deuteron as a neutron target, for example, or for studies of the (extended) Gerasimov-Drell-Hearn sum rule, deep inelastic scattering, or baryon resonance production in nuclei. Our interest is on experiments that probe the conventional picture of a nucleus as composed of baryons and mesons, and that probe how far models with these effective degrees of freedom can be extended. Table 1 is a summary of some of the JLab exeriments that fit this description, and that we will review in the sections below.

The high precision, large momentum transfer measurements may be sensisitive to effects not incorporated in the conventional nuclear model. It seems self-evident that probes of short distances, well below the size of the nucleon, should require explicit consideration of the quark substructure of the nucleons. Our review suggests that evidence for the appearance of these effects seems to depend on the nature of the reaction. In elastic scattering, where only the NN chanel is expicitly excited, a successful description is obtained using a relativistic description of the NN channel together with a minor modification of the short-range structure of the nucleon current (see Sec. 3). In photodisintegration by 4 GeV photons, where hundreds of N^*N^* channels are explicitly excited, an efficient explanation seems to require the explicit use of quark degrees of freedom (see Sec. 5).

This review begins with a survey of deuteron wave functions, and then discusses the deuteron form factors, threshold electrodisintegration, and high energy deuteron photodisintegration. We also call attention to recent reviews by Garçon and Van Orden

Table 1. Some JLab deuterium experiments.

Experiment	Reaction / Observables	Status
	elastic scattering	
91-026	A	paper published [2]
	B	analysis in progress
94-018	A	paper published [3]
	t_{20}	paper published [4]
	electrodisintegration	
89-028	recoil proton polarization	analysis in progress
94-004	in-plane response functions	analysis in progress
94-102	high momentum structure	awaiting beam time
00-103	threshold $d(e, e')pn$	proposal
	photodisintegration	
89-012	cross sections	paper published [5]
89-019	p_y, $C_{x'}$, $C_{z'}$	paper published [6]
96-003	cross sections	paper published [7]
93-017	cross sections	analysis in progress
99-008	cross sections	analysis in progress
00-007	p_y, $C_{x'}$, $C_{z'}$	awaiting beam time
00-107	p_y, $C_{x'}$, $C_{z'}$	awaiting beam time

[8], and by Sick [9]. These reviews contain a discussion of the static properties of the deuteron and a survey of recent models of the nucleon form factors, two topics we have decided to omit from this work. Both also have an extensive discussion of the deuteron form factors.

2. Deuteron Wave Functions

Calculations of deuteron form factors and photo and electrodisintegration to the NN final state require a deuteron wave function, the final state NN scattering amplitude (if the transition is inelastic), and the current operator, all of which should be consistently determined from the underlying dynamics. Deuteron wave functions used in the *conventional nuclear model* will be reviewed in this section.

2.1. Nonrelativistic wave functions

The nonrelativistic NN wave function of the deuteron can be written in terms of two scalar wave functions. In coordinate space the full wave function is

$$\Psi^+_{abm}(\mathbf{r}) = \sum_\ell \sum_{m_s} \frac{z_\ell(r)}{r} Y_{\ell\, m-m_s}(\hat{\mathbf{r}})\, \chi^{1m_s}_{ab} \langle \ell\, 1\, m - m_s\, m_s | 1\, m \rangle$$

$$= \frac{u(r)}{r} Y_{00}(\hat{\mathbf{r}})\, \chi^{1m}_{ab} + \frac{w(r)}{r} \sum_{m_s} Y_{2\, m-m_s}(\hat{\mathbf{r}})\, \chi^{1m_s}_{ab} \langle 2\, 1\, m - m_s\, m_s | 1\, m \rangle \qquad (1)$$

where $Y_{\ell m_\ell}$ are the spherical harmonics normalized to unity on the unit sphere, $z_0 = u$ and $z_2 = w$ are the reduced S and D-state wave functions, and the $+$ distinguishes this from other (relativistic) components of the wave function to be described below. The spin part of the wave function is

$$\chi_{ab}^{1m_s} = \begin{cases} |+\rangle_a |+\rangle_b & m_s = + \\ \dfrac{1}{\sqrt{2}} \left\{ |+\rangle_a |-\rangle_b + |-\rangle_a |+\rangle_b \right\} & m_s = 0 \\ |-\rangle_a |-\rangle_b & m_s = - \end{cases} \tag{2}$$

Introducing the familar compact notation for matrix operations on each of the two nucleon subspaces 1 and 2

$$A_{aa'} |+\rangle_{a'} = A_1 |+\rangle_1 , \tag{3}$$

where A is any 2×2 operator, we can show that

$$Y_{00} \, \chi_{ab}^{1m} = \frac{1}{\sqrt{4\pi}} \, \sigma_1 \cdot \sigma_2 \, \chi_{12}^{1m} = \frac{1}{\sqrt{4\pi}} \, \chi_{12}^{1m_s}$$

$$\sum_{m_s} Y_{2\,m-m_s}(\hat{\mathbf{r}}) \, \chi_{ab}^{1m_s} \langle 2\,1\,m - m_s\, m_s | 1\,m \rangle = \frac{1}{\sqrt{32\pi}} (3\,\sigma_1 \cdot \hat{\mathbf{r}}\, \sigma_2 \cdot \hat{\mathbf{r}} - \sigma_1 \cdot \sigma_2) \, \chi_{12}^{1m} . \tag{4}$$

These identities permit us to write the wave function (1) in a convenient operator form [10]:

$$\Psi_{abm}^{+}(\mathbf{r}) = \frac{1}{\sqrt{4\pi}\, r} \left[u(r)\, \sigma_1 \cdot \sigma_2 + \frac{w(r)}{\sqrt{8}} (3\,\sigma_1 \cdot \hat{\mathbf{r}}\, \sigma_2 \cdot \hat{\mathbf{r}} - \sigma_1 \cdot \sigma_2) \right] \chi_{12}^{1m} \tag{5}$$

In momentum space the deuteron wave function becomes

$$\Psi_{abm}^{+}(\mathbf{p}) \equiv \frac{1}{\sqrt{(2\pi)^3}} \int d^3r\, e^{-i\mathbf{p}\cdot\mathbf{r}} \, \Psi_{abm}^{+}(\mathbf{r})$$

$$= \frac{1}{\sqrt{4\pi}} \left[u(p)\, \sigma_1 \cdot \sigma_2 - \frac{w(p)}{\sqrt{8}} (3\,\sigma_1 \cdot \hat{\mathbf{p}}\, \sigma_2 \cdot \hat{\mathbf{p}} - \sigma_1 \cdot \sigma_2) \right] \chi_{12}^{1m} . \tag{6}$$

We use the same notation for both coordinate and momentum space wave functions. If $u(p) = z_0(p)$ and $w(p) = z_2(p)$, then

$$z_\ell(p) = \sqrt{\frac{2}{\pi}} \int_0^\infty r dr \, z_\ell(r) \, j_\ell(pr)$$

$$\frac{z_\ell(r)}{r} = \sqrt{\frac{2}{\pi}} \int_0^\infty p^2 dp \, z_\ell(p) \, j_\ell(pr) . \tag{7}$$

Note the appearance of the factors $\sqrt{2/\pi}$, a feature of the symmetric definition (6).

The normalization condition

$$\int d^3r \, \Psi_{abm'}^{+\dagger}(\mathbf{r}) \, \Psi_{abm}^{+}(\mathbf{r}) = \delta_{m'm} \tag{8}$$

implies

$$1 = \int_0^\infty dr \left[u^2(r) + w^2(r) \right] = \int_0^\infty p^2 \, dp \left[u^2(p) + w^2(p) \right] \tag{9}$$
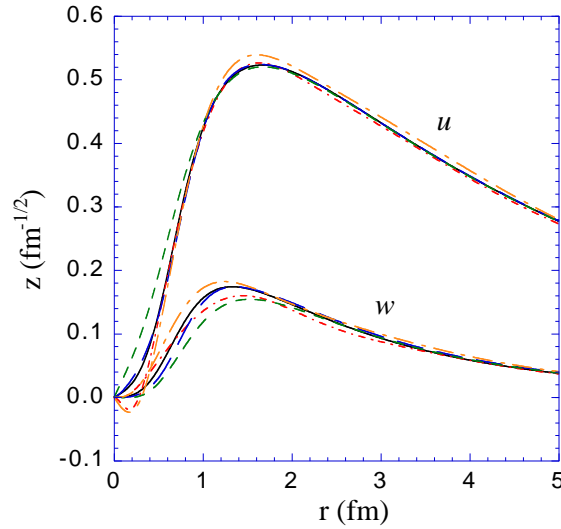
Figure 1. Reduced coordinate space wave functions for five models discussed in the text: AV18 (solid), Paris (long dashed), CD Bonn (short dashed), IIB (short dot-dashed), and W16 (long dot-dashed).

The D-state probability,

$$P_D = \int_0^\infty dr\, w^2(r) \tag{10}$$

is an interesting measure of the strength of the tensor component of the NN force, even though it is a model dependent quantity with no unique measurable value [11].

The best nonrelativistic wave functions are calculated from the Schrödinger equation using a potential adjusted to fit the NN scattering data for lab energies from 0 to 350 MeV. The quality of realistic potentials have improved steadily, and now the best potentials give fits to the NN data with a $\chi^2/\text{d.o.f} \simeq 1$. The Paris potential [12] was among the first potentials to be determined from such realistic fits, and it has since been replaced by the Argonne V18 potential (denoted by AV18) [13], the Nijmegen potentials [14], and most recently by the CD Bonn potentials [15, 16]. The S and D-state wave functions determined from three of these models are shown in Figs. 1 and 2. These figures also show S and D wave functions from two relativistic models to be discussed shortly. In the right panel of the second figure we plot the dimensionless ratios $u(p)/u_s(p)$ and $w(p)/w_s(p)$, where the scaling functions, in units of GeV$^{-3/2}$, are

$$u_s(p) = \frac{16m\epsilon}{(m\epsilon + p^2)(1 + p^2/p_0^2)}$$
$$w_s(p) = \frac{16m\epsilon\, p^2/p_1^2}{(m\epsilon + p^2)(1 + p^2/p_0^2)^2} \;. \tag{11}$$

Here ϵ is the deutreron binding energy and m the nucleon mass (we used $m\epsilon = 940\times2.224$ MeV^2), $p_0^2 = 0.15$ GeV^2, and $p_1^2 = 0.1$ GeV^2. We emphasize that these scaling functions *have absolutely no theoretical significance* and were introduced merely to remove the
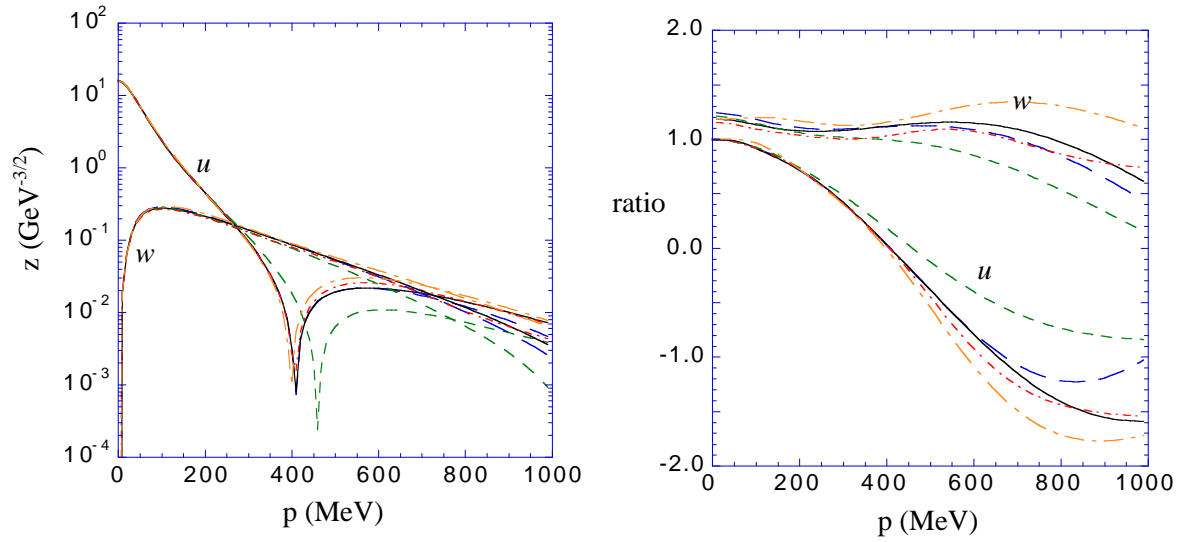
Figure 2. Momentum space wave functions for five models discussed in the text (see the caption to Fig. 1). The wave functions in the right panel have been divided by the scaling functions $u_s(p)$ and $w_s(p)$.

most rapid momentum dependence so that the percentage difference between models can be more easily read from the ratio graph. We conclude that the five models shown are almost identical (i.e.variations of less than 10%) for momenta below about 400 MeV, and that they vary by less than a factor of 2 as the momenta reaches 1 GeV (except near the zeros).

2.2. Relativistic wave functions

The definition of the relativistic deuteron wave function depends in large part on the formalism used to treat relativity. In formalisms based on hamiltonian dynamics (discussed in Sec. 3.6.6) the wave function in the deuteron rest frame can be taken to be identical to the nonrelativistic wave function, and no further discussion is necessary until the wave function in a moving frame is needed. In formalisms based on the Bethe-Salpeter equation [17], the covariant spectator equation [18], or on some other quasi-potential equation [19, 20], the wave functions usually have additional components which do not vanish in the rest frame.

In the relativistic spectator formalism [18], where one of the two bound nucleons is off-mass shell, the wave function is a sum of a positive energy component and a negative energy component [10]

$$\Psi_{a\alpha m}(\mathbf{p}) = \sum_{b} \left\{ \Psi^{+}_{abm}(\mathbf{p})\, u_{\alpha}(-\mathbf{p}, b) + \Psi^{-}_{abm}(\mathbf{p})\, v_{\alpha}(\mathbf{p}, b) \right\}, \tag{12}$$

where $u_{\alpha}(-\mathbf{p}, b)$ and $v_{\alpha}(\mathbf{p}, b)$ are nucleon spinors for the off-shell particle (particle 2 in this case) with Dirac index α. The positive energy part has the same structure as the

nonrelativistic wave function, with an S and D-state component. The new negative energy wave function has the form

$$\Psi_{abm}^-(\mathbf{p}) = v_t(p) \sum_{m_s} Y_{1\,m-m_s}(\hat{\mathbf{p}})\,\chi_{ab}^{1m_s}\,\langle 1\,1\,m-m_s\,m_s|1\,m\rangle - v_s(p)\,Y_{1\,m}(\hat{\mathbf{p}})\,\chi_{ab}^0$$

$$= \sqrt{\frac{3}{4\pi}}\frac{1}{2}\left[\frac{v_t(p)}{\sqrt{2}}\,(\sigma_1+\sigma_2)\cdot\hat{\mathbf{p}} + v_s(p)\,(\sigma_1-\sigma_2)\cdot\hat{\mathbf{p}}\right]\chi_{ab}^{1m}, \tag{13}$$

where $v_t(p)$ and $v_s(p)$ are two additional P-state components of the wave function, and

$$\chi_{ab}^0 = \frac{1}{\sqrt{2}}\left\{|+\rangle_a\,|-\rangle_b - |-\rangle_a\,|+\rangle_b\right\} \tag{14}$$

is the nuclear spin 0 wave function. The names of the P-state wave functions follow from the fact that v_t couples to the spin triplet ($S = 1$) and v_s to the spin singlet ($S = 0$) wave function. The equivalence of the two forms given in Eq. (13) follows from identities like those given in Eq. (4).

Two model relativistic S and D-state wave functions were shown in Figs. 1 and 2. Both models are based on relativistic one boson exchange model developed in Ref. [21]. Model IIB is a revised version of the model of the same name originally described in Ref. [21] and Model W16 is one of a family of models with varying amounts of off-shell sigma coupling that were introduced in connection the relativistic calculations of the triton binding energy described in Ref. [22]. These models are described further in a number of conference talks [23]. The relativistic P-state components are small, but can make important contributions to the deuteron magnetic form factor. As Figs. 1 and 2 show, the large S and D-state components of these relativistic wave functions are very close to their nonrelativistic counterparts.

3. Elastic Electron Deuteron Scattering

3.1. Deuteron Form Factors and Structure Functions

Because of the very small value of the electromagnetic fine structure constant ($\alpha = e^2/4\pi\hbar c \simeq 1/137$), elastic electron–deuteron scattering is described to high precision by assuming that the electron exchanges a single virtual photon when scattering from the deuteron. In this one-photon exchange approximation [24] elastic scattering is fully described by three deuteron form factors [25, 26, 27]. In its most general form, the relativistic deuteron current can be written [28, 25]

$$\langle d'|J^\mu|d\rangle = -\left(\left\{G_1(Q^2)\,[\xi'^*\cdot\xi] - G_3(Q^2)\frac{(\xi'^*\cdot q)(\xi\cdot q)}{2m_d^2}\right\}(d^\mu+d'^\mu)\right.$$

$$\left. + G_M(Q^2)\,[\xi^\mu(\xi'^*\cdot q) - \xi'^{*\mu}(\xi\cdot q)]\right), \tag{15}$$

where the form factors $G_i(Q^2)$, $i = 1-3$, are all functions of Q^2, the square of the four-momentum transferred by the electron, with $q = d'-d$ and $Q^2 = -q^2$. [In most of

the following discussion we will suppress the explicit Q^2 dependence of the form factors.] In practice, G_1 and G_3 are replaced by a more physical choice of form factors

$$G_C = G_1 + \frac{2}{3}\eta\, G_Q$$
$$G_Q = G_1 - G_M + (1+\eta)G_3\,, \tag{16}$$

with $\eta = Q^2/4m_d^2$. At $Q^2 = 0$, the form factors G_C, G_M, and G_Q give the charge, magnetic and quadrupole moments of the deuteron

$$
\begin{aligned}
G_C(0) &= 1 && \text{(in units of } e) \\
G_Q(0) &= Q_d && \text{(in units of } e/m_d^2) \\
G_M(0) &= \mu_d && \text{(in units of } e/2m_d)\,.
\end{aligned}
\tag{17}
$$

The form factors can also be related to the helicity amplitudes of the deuteron current (where helicity is the projection of the spin in the direction of the particle three-momentum). In the Breit frame (where the energy transfer ν is zero) the polarizations of the incoming (ξ) and outgoing (ξ') deuteron are

$$
\xi_\lambda = \begin{cases} (0, \pm 1, -i, 0)/\sqrt{2} & \lambda = \pm \\ (-Q/2, 0, 0, D_0)/m_d & \lambda = 0 \end{cases}
$$
$$
\xi'_{\lambda'} = \begin{cases} (0, \mp 1, -i, 0)/\sqrt{2} & \lambda' = \pm \\ (Q/2, 0, 0, D_0)/m_d & \lambda' = 0\,, \end{cases}
\tag{18}
$$

(where the phases for the incoming deuteron follow the conventions of Jacob and Wick [29] for particle 2) and the virtual photon polarization is

$$
\epsilon_{\lambda_\gamma} = \begin{cases} (0, \mp 1, -i, 0)/\sqrt{2} & \lambda_\gamma = \pm \\ (1, 0, 0, 0) & \lambda_\gamma = 0\,. \end{cases}
\tag{19}
$$

Hence, denoting the helicity amplitudes by $G^{\lambda_\gamma}_{\lambda'\lambda}$, the three independent amplitudes are

$$G^0_{00}(Q^2) = 2D_0\left(G_C + \frac{4}{3}\eta G_Q\right)$$
$$G^0_{+-}(Q^2) = G^0_{-+}(Q^2) = 2D_0\left(G_C - \frac{2}{3}\eta G_Q\right)$$
$$G^+_{+0}(Q^2) = -G^+_{0-}(Q^2) = G^-_{-0}(Q^2) = -G^-_{0+}(Q^2) = 2D_0\sqrt{\eta}\, G_M\,, \tag{20}$$

where $2D_0 = \sqrt{4m_d^2 + Q^2}$.

The scattering amplitude in the one-photon approximation is

$$\mathcal{M} = -\frac{e^2}{Q^2}\left[\bar{u}(k',\lambda')\,\gamma^\mu\, u(k,\lambda)\right]\langle d'|J_\mu|d\rangle\,, \tag{21}$$

where u and $\bar{u}$ are electron spinors with k, λ (k', λ') the momentum and helicity of the incoming (outgoing) electron, respectively. Squaring (21), summing over the final spins, and averaging over initial spins give the following result for the unpolarized differential cross section

$$\frac{d\sigma}{d\Omega} = \frac{d\sigma}{d\Omega}\bigg|_{NS}\left[A(Q^2) + B(Q^2)\tan^2(\theta/2)\right] = \frac{d\sigma}{d\Omega}\bigg|_{NS} S(Q^2, \theta) \tag{22}$$

where $S(Q^2, \theta)$ is defined by this relation, and

$$\left.\frac{d\sigma}{d\Omega}\right|_{NS} = \frac{\alpha^2 E' \cos^2(\theta/2)}{4E^3 \sin^4(\theta/2)} = \sigma_M \frac{E'}{E} = \sigma_M \left(1 + \frac{2E}{m_d} \sin^2 \tfrac{1}{2}\theta\right)^{-1}, \qquad (23)$$

is the cross section for scattering from a particle without internal structure (σ_M is the Mott cross section), and θ, E, E', and $d\Omega$ are the electron scattering angle, the incident and final electron energies, and the solid angle of the scattered electron, all in the lab system. The structure functions A and B depend on the three electromagnetic form factors

$$A(Q^2) = G_C^2(Q^2) + \frac{8}{9}\eta^2 G_Q^2(Q^2) + \frac{2}{3}\eta G_M^2(Q^2)$$
$$\equiv A_C(Q^2) + A_Q(Q^2) + A_M(Q^2)$$
$$B(Q^2) = \frac{4}{3}\eta(1+\eta)G_M^2(Q^2), \qquad (24)$$

where the definitions of A_C, A_Q, and A_M should be clear from the context.

While cross section measurements can determine A, B, and G_M, separating the charge G_C and quadrupole G_Q form factors requires polarization measurements. The polarization of the outgoing deuteron can be measured in a second, analyzing scattering. The cross section for the double scattering process can be written [26]

$$\frac{d\sigma}{d\Omega d\Omega_2} = \left.\frac{d\sigma}{d\Omega d\Omega_2}\right|_0 \Big[1 + \tfrac{3}{2}h\,p_x A_y \sin\phi_2$$
$$+ \tfrac{1}{\sqrt{2}}t_{20}A_{zz} - \tfrac{2}{\sqrt{3}}t_{21}A_{xz}\cos\phi_2 + \tfrac{1}{\sqrt{3}}t_{22}(A_{xx} - A_{yy})\cos 2\phi_2\Big], \qquad (25)$$

where $h = \pm 1/2$ is the polarization of the incoming electron beam, ϕ_2 the angle between the two scattering planes (defined in the same way as the ϕ shown in Fig. 24), and A_y and the A_{ij} are the vector and tensor analyzing powers of the second scattering. Although there is a p_z component to the vector polarization, the term is omitted from Eq. (25) as there is no longitudinal vector analyzing power; without spin precession, this term can not be determined. The polarization quantities p_i and t_{2m_ℓ} (sometimes denoted T_{2m_ℓ}, but we will reserve capital letters for target asymmetries) are functions of the form factors and the electron scattering angle

$$S\,p_x = -\tfrac{4}{3}\big[\eta(1+\eta)\big]^{1/2} G_M(G_C + \tfrac{1}{3}\eta G_Q)\tan\tfrac{1}{2}\theta$$
$$S\,p_z = \tfrac{2}{3}\eta\big[(1+\eta)(1+\eta\sin^2\tfrac{1}{2}\theta)\big]^{1/2} G_M^2 \tan\tfrac{1}{2}\theta\sec\tfrac{1}{2}\theta$$
$$-\sqrt{2}S\,t_{20} = \tfrac{8}{3}\eta\,G_C G_Q + \tfrac{8}{9}\eta^2 G_Q^2 + \tfrac{1}{3}\eta\big[1 + 2(1+\eta)\tan^2\tfrac{1}{2}\theta\big]G_M^2$$
$$\sqrt{3}\,S\,t_{21} = 2\,\eta\big[\eta + \eta^2\sin^2\tfrac{1}{2}\theta\big]^{1/2}G_M G_Q\sec\tfrac{1}{2}\theta$$
$$-\sqrt{3}S\,t_{22} = \tfrac{1}{2}\eta\,G_M^2 \qquad (26)$$

The same combinations of form factors occur in the tensor polarized target asymmetry as in the recoil deuteron tensor polarization.

Of these quantities, $t_{20} = T_{20}$ has been most extensively measured; it does not require a polarized beam or a measurement of the out of plane angle ϕ_2. For

measurements of A and T_{20} at forward electron scattering angles, the G_M terms are very small, and one may approximate A and T_{20} by

$$S \to \tilde{A} \equiv \quad G_C^2 + \frac{8}{9}\eta^2 G_Q^2$$

$$-\sqrt{2}S\,\tilde{T}_{20} = \frac{8}{3}\eta\,G_C G_Q + \frac{8}{9}\eta^2 G_Q^2 \tag{27}$$

Introducing $y = 2\eta G_Q/3G_C$ gives

$$\tilde{T}_{20} = -\sqrt{2}\,\frac{y(2+y)}{1+2y^2} \tag{28}$$

The minimum of $T_{20} \approx \tilde{T}_{20} = -\sqrt{2}$ is reached for $y = 1$. The node in the charge form factor, $G_C = 0$, occurs when $S \to \frac{8}{9}\eta^2 G_Q^2$, and $-\sqrt{2}\,S\,\tilde{T}_{20} \to \frac{8}{9}\eta^2 G_Q^2$, giving $\tilde{T}_{20} = -1/\sqrt{2}$.

This approximation also makes it clear that $\tilde{T}_{20}$ largely depends on the deuteron structure, rather than the nucleon electromagnetic form factors. In the nonrelativistic limit (to be discussed shortly), both G_C and G_Q are a product of the nucleon isoscalar electric form factor multiplied by the *body form factor*, which is an integral over products of the deuteron wave functions weighted by spherical Bessel functions. Hence, in this approximation, the nucleon electric form factor cancels in the ratio $y \propto G_Q/G_C$, and $\tilde{T}_{20}$ depends only on the deuteron wave function.

We note that the relations above between the form factors and the observables are model independent, so it is possible to extract form factors from the data and compare directly to theoretical calculations. The most complete form factor determination appeared recently in Ref. [30] (see also the analysis in Ref. [9]). We will discuss the data below in Sec. 3.8, after we have reviewed the experiments and the theory.

3.2. Experimental overview

The initial measurements of elastic ed scattering were by McIntyre and Hofstadter in the mid 1950s [31]. Since then many experiments have run at several laboratories; the fits of Ref. [30] include 269 cross sections from 19 references, dating from 1960 to the present‡. Polarization experiments are much more difficult. The first results were

‡ An important feature of the recent fits of the world data is that the measured cross sections were refit rather than using extracted structure functions or form factors. This is necessary since most extractions of A (B) used corrections for contributions of B (A) to their cross sections from earlier data. In some cases alternative definitions (or incorrect formulas) have been given. A minor point is the definition of σ_M; in some cases the recoil factor E'/E is included, while in our definition Eq. (23) it is not. The magnetic form factor G_M can be in units of $e/2m_d$ (our convention), $e/2m_p$, or dimensionless, with magnitude of 1.714, 0.857, or 1.0, respectively, at $Q^2 = 0$, and leading to modified coefficients in Eq. (24). Buchanan and Yearian [32] have an alternate definition of G_C, and G_Q, with $A \propto (1-\eta)^2(G_C^2 + G_Q^2)$. Benaksas *et al* [33] and Galster *et al* [34] include an extra factor $1+\eta$ in the magnetic terms in A and B, which changes the Q^2 dependence of the magnetic form factor, though not its value at $Q^2 = 0$. Ganichot *et al* [35] and Grossetête *et al* [36] both use a factor of e^2, rather than α^2, in their definitions of the Mott cross section. Cramer *et al* [37] give a dimensionally incorrect formula for their σ_0 $(= d\sigma/d\Omega|_{NS})$, with explicitly stated energy factors of $E'/(EE') = 1/E$, as opposed to our factor of E'/E^3.

published in 1984 and there are now only 20 published t_{20} data points, and 19 points for other polarization observables. The fits of Ref. [9] include a slightly larger data base, with 340 points for momentum transfers up to Q of about 1.6 GeV; this misses only a handful of the largest momentum transfer SLAC and JLab data points.

Forward-angle cross section measurements suffice to determine A, both because B is small and because of the $\tan^2 \theta/2$ dependence. The magnetic form factor G_M is determined from large angle measurements of B, since the A contribution vanishes as $\theta \to 180°$. With $Q^2 \simeq 4EE' \sin^2(\theta/2)$ and $E' = E(1 + (2E/m_d) \sin^2(\theta/2))^{-1}$, we obtain the following relations at $\theta = 180°$:

$$Q^2 = 4E^2 \left(1 + 2E/m_d\right)^{-1} \tag{29}$$

$$E = \left(Q^2 + \sqrt{Q^2(Q^2 + 4m_d^2)}\,\right)/4m_d. \tag{30}$$

One can see that the beam energies needed for high Q^2 measurements of B are quite low, with $E = 0.65, 1.02, 1.35, 1.67$, and 1.97 GeV corresponding to $Q^2 = 1, 2, 3, 4$, and 5 GeV^2, respectively. Note that throughout this review we use $Q = \sqrt{Q^2}$ to avoid confusion with the magnitude of the three momentum transfer $\mathbf{q}$, and we use units of GeV and GeV^2, not fm^{-1} or fm^{-2}.

Accurate measurements require that Q^2 be known accurately since A and B vary rapidly with Q^2. Energy or angle offsets of a few times 10^{-3} could lead to Q^2 being off by up to 0.5%. For both A and B, this leads to offsets that increase with Q^2, reaching about 2% at $Q^2 = 1$ GeV^2 and 4% at $Q^2 = 6$ GeV^2.

While cross section measurements can determine A, B, and G_M, separating the charge G_C and quadrupole G_Q form factors requires polarization measurements, most often t_{20}. Coincidence detection of the scattered electron and deuteron, which suppresses the background and allows experiments to be performed with moderate resolution, is a common technique.

3.2.1.   Experimental status of A   Several experiments have measured the structure function A at small Q. Of particular note are the high precision, 1 - 2% measurements from Monterey [38], Mainz [39], and Saclay ALS [40]. The only measurements at moderately large Q are from SLAC E101 [41], Bonn [37] and CEA [42], plus the two recent JLab experiments in Halls A [2] and C [3]. Data for several experiments are shown in Fig. 3 and summarized in Table 2; see Refs. [9], [30] or [44] for more extensive listings of data.

Fig. 3 reveals an unfortunate history of certain measurements not agreeing to within the stated uncertainties. For example, at low Q the Monterey and Mainz data overlap well, but the overlap of Mainz and Saclay ALS data indicates problems. The four largest Q Mainz points used Rosenbluth separations, with A largely determined from forward angles of 50°, 60°, 80°, and 90° at 298.9 MeV. Saclay A data were extracted from measured cross sections using previous B data. The closest corresponding Saclay points, for the same scattering angles at a beam energy of 300 MeV, have cross section about

**Table 2.** Some measurements of A. Symbols are given for data shown in the figures.

Experiment	Q (GeV)	symbol	# of points	Year and Reference
Stanford Mark III	0.48 - 0.88	□	5	1965 [32]
Orsay	0.34 - 0.48	×	4	1966 [33]
CEA	0.76 - 1.15	◇	18	1969 [42]
DESY	0.49 - 0.71	○	10	1971 [34]
Monterey	0.04 - 0.14	△	9	1973 [38]
SLAC E101	0.89 - 2.00	⊞	8	1975 [41]
Yerevan	0.12 - 0.19	*not shown**	25	1979 [43]
Mainz	0.04 - 0.39	⊙	16	1981 [39]
Bonn	0.71 - 1.14	⊡	5	1985 [37]
Saclay ALS	0.13 - 0.84	▽	43	1990 [40]
JLab Hall A	0.83 - 2.44	■	16	1999 [2]
JLab Hall C	0.81 - 1.34	●	6	1999 [3]

*Have larger errors and are consistent with the other data sets.

7% smaller; the difference is beyond the quoted experimental uncertainties. Significant differences such as this are often obscured by semilog plots or not plotting all data sets. The body of data, aside from the lowest Q Orsay point, suggests the correctness of the Saclay measurments. Theoretical predictions span the range between the two data sets, and do not help to determine which is correct. Thus, a new high precision experiment in this Q^2 range appears desirable.

The agreement between data from CEA, SLAC E101, and Bonn near 1 GeV was also unsatisfactory. In discussing these measurements, we will compare to the trend of the data as determined by the Saclay and JLab measurements. The CEA data have large uncertainties, and are systematically low by about 1σ. This experiment measured scattered electrons in a shower counter and deuterons in a spectrometer that used a quadrupole magnet with a stopper blocking out the central weak field region. In such a case it is difficult to determine the solid angle precisely, and this uncertaintly might introduce systematic errors into this data. Alternatively, since the spectra were not significantly wider than the elastic peak, it has been suggested that over-subtraction of background was a problem. However, the background rates were determined to be consistent with expected rates from random coincidences and target cell walls. Bonn measured coincidence cross sections at large electron scattering angles, $\theta_e \approx 80°$ - $140°$. Using forward angle data from SLAC E101, CEA, and Orsay, Bonn determined A and B. Slightly inconsistent results from the other experiments led to a small uncertainty on the Bonn determination of A. Thus, it is only the largest Q^2 point, for which there was only the large angle Bonn data, that has very significant disagreement with other determinations of A. Finally, the lowest Q^2 SLAC point is high.

The disagreements between the CEA, SLAC E101, and Bonn data were part of the motivation for two JLab experiments that determined A. Hall A experiment E91-026 [2] measured A for Q^2 from 0.7 to 6.0 GeV^2. Hall C experiment E94-018 [3]
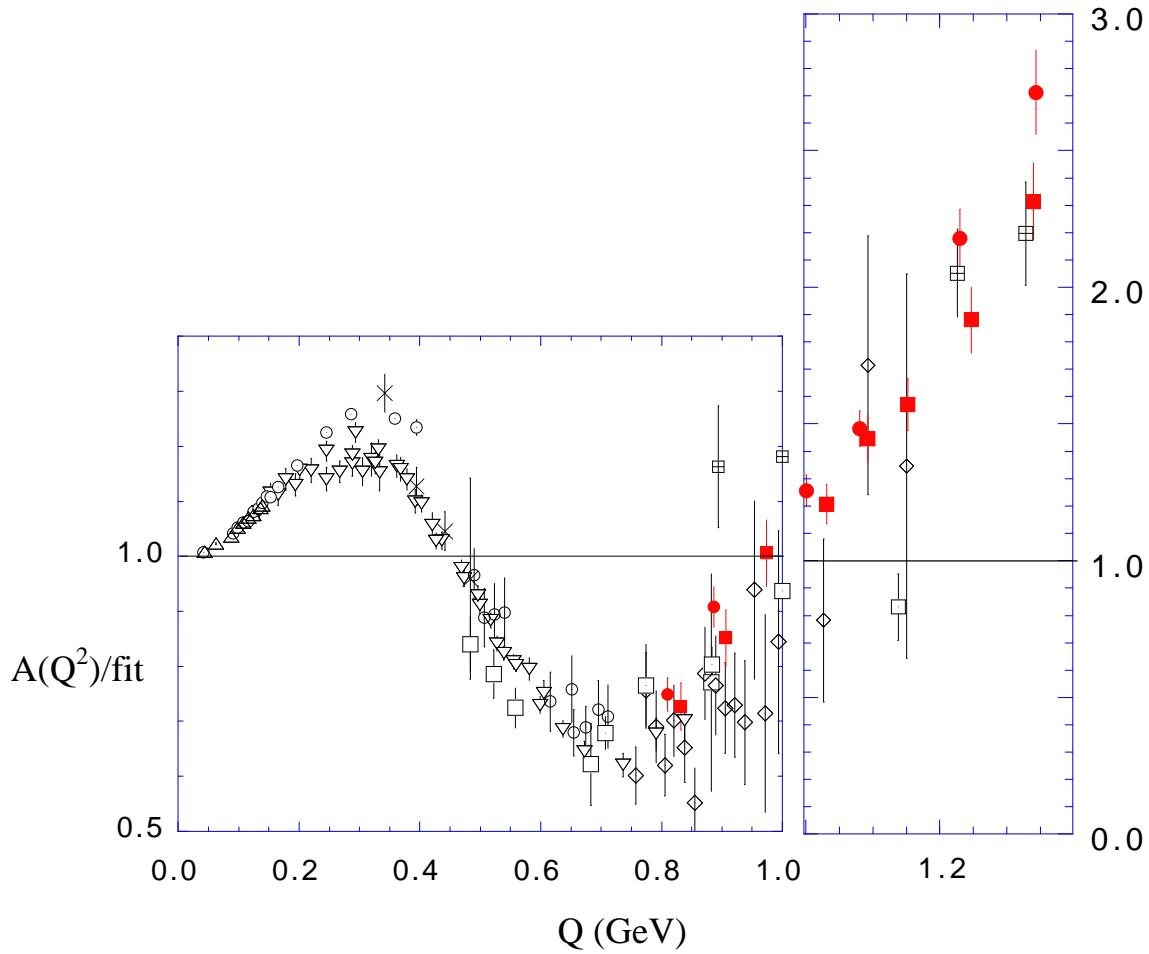
Figure 3. The data for A at low and moderate Q, normalized as explained in Section 3.3.2. The data sets are described in Table 2. Note that the right and left panels have different vertical scales. All data referred to in Table 2 are shown except the highest Q points from Refs. [2] and[41].

measured A in the same kinematics as its t_{20} points, from 0.7 to 1.8 GeV^2. The main advantages of these experiments over previous work include the continuous beam, large luminosities, and modern spectrometers. The Hall A measurements [2] used > 100 μA beams on a 15 cm cryogenic LD$_2$ target, to achieve a luminosity of approximately 5 $\times$ 10^{38}/cm^2/s, and two approximately 6 msr spectrometers. The Hall C measurements used the HMS spectrometer along with the deuteron channel built to measure t_{20} with the recoil polarimeter POLDER. A feature of this system is that the solid angles of the two spectrometers were well matched, to within a few percent.

In the overlap region, the two JLab experiments show better precision than the earlier data and generally good agreement; comparisons of theory to data should

Table 3. Some measurements of B. Symbols are given for data shown in the figures.

Experiment	Q (GeV)	symbol	# of points	Year and Reference
Stanford Mark II	0.10 - 0.13	*	2	1964 [53]
Stanford Mark III	0.48 - 0.68	□	4	1965 [32]
Orsay	0.20 - 0.28	*	3	1966 [36]
Orsay	0.34 - 0.44	*	3	1966 [33]
Stanford Mark III	0.44 - 0.63	*	5	1967 [54]
Orsay	0.14 - 0.48	*	4	1972 [35]
Naval Research Lab	0.11	*	1	1980 [55]
Mainz	0.25 - 0.39	○	4	1981 [39]
Bonn	0.71 - 1.14	▽	5	1985 [37]
Saclay ALS	0.51 - 1.04	◇	13	1985 [52]
SLAC NPAS NE4	1.10 - 1.66	⊞	9	1987 [50, 51]
JLab Hall A	0.7 - 1.4	■	6	unpublished

*These data sets are not shown (B must be inferred from the publication).

focus on these results, rather than the older data. However, these measurements also show a significant disagreement with each other. Uncertainties in each experiment are dominated by systematics of approximately 5 - 6%, with statistical precisions near 1%. The Hall C data are systematically larger than the Hall A data by just over 2σ, slightly over 10%, and there appears to be a tendency of the data sets to diverge with increasing momentum transfer. This discrepancy will be decreased by a few percent, but not eliminated, by a correction [8] to a lower, more accurate, beam energy in Hall C during the experiment. It is unclear if the discrepancy can be further resolved.

An important experimental point is the use in these experiments, and in many earlier ones, of ep elastic scattering to calibrate the solid angle acceptance; a fit to the world ep cross section data is often used [45]. However, recent high precision polarimetry results [46, 47, 48] imply that G_E^p/G_M^p is significantly smaller than previously believed, with G_E^p/G_M^p dropping nearly linearly for Q^2 from about 0.5 to 5.6 GeV². Refitting the world cross section data, with the JLab data for the form factor ratio, decreases G_E^p but enhances G_M^p by about 2% [49]. The new fits imply that the ep cross section is generally a few percent larger than would have been calculated previously, less than the systematic uncertainties of most experiments, and too small to affect comparisons of measurements of the ed cross sections and A. The effects on the theoretical deuteron form factor predictions will be addressed below.

In summary, the structure function A is reasonably well determined up to $Q^2 = 6$ GeV², if one neglects several poorer data points. There remain regions in which there are up to about 10% systematic discrepancies between data of different experiments; the resolution of these problems is at present unclear.

3.2.2. *Experimental status of B* The highest Q^2 measurements of the B structure function come from SLAC NPAS experiment NE4 [50, 51], which covered the Q^2 range

Table 4. World data for tensor polarization observables.

Experiment	Type	Q (GeV)	Observables	Symbol	# of points	Year and Reference
Bates	polarimeter	0.34, 0.40	t_{20}	$\times$	2	1984 [56]
Novosibirsk VEPP-2	atomic beam	0.17, 0.23	T_{20}	⊞	2	1985 [57, 58]
Novosibirsk VEPP-3	storage cell	0.49, 0.58	T_{20}	$\triangle$	2	1990 [59]
Bonn	polarized target	0.71	T_{20}	$\diamondsuit$	1	1991 [60]
Bates	polarimeter	0.75 - 0.91	t_{20},t_{21},t_{22}	●	3	1991 [61, 62]
Novosibirsk VEPP-3	storage cell	0.71	T_{20}	*	1	1994 [63]
NIKHEF	storage cell	0.31	T_{20},T_{22}	○	1	1996 [64]
NIKHEF	storage cell	0.40 - 0.55	T_{20}	□	3	1999 [65]
JLab Hall C 94-018	polarimeter	0.81 - 1.31	t_{20},t_{21},t_{22}	■	6	2000 [4]
Novosibirsk VEPP-3	storage cell	0.63 - 0.77	T_{20}	⊙**	5	2001 [66]

* Not shown in the figures.
** Preliminary data.

of 1.20 to 2.77 GeV^2. These measurements extended the range of previous data from Saclay [52] (which went to 1.1 GeV^2), and from Bonn [37] (which went to 1.3 GeV^2, and gave the results for A discussed above). There is good overlap in all but a few of the earliest B measurements. Measurements of B were taken as part of E91-026 for Q^2 = 0.7 to 1.4 GeV^2, but analysis is not yet final.

3.2.3.   Experimental status of polarization measurements   A summary of the world data is shown in Table 4. The first polarization measurements were from an Argonne/Bates recoil polarimeter experiment [56] and a Novosibirsk VEPP-2 experiment [57, 58] using a polarized gas jet target. In the gas jet experiment, a polarimeter measured the gas polarization after it passed through the interaction region.

There were three second generation experiments. An Argonne/Novosibirsk VEPP-3 measurement [59] pioneered the use of storage cells, increased the internal target density about a factor of 15 over the gas jet alone, and pushed out to 0.58 GeV, near the minimum in t_{20}. Because the polarization of the gas varies in the cell, due to wall and beam interactions, it was decided to normalize the gas polarization by setting the lowest Q datum, at 0.39 GeV, to theory where the uncertainties are small. Such internal targets in storage rings are now common. A Bonn polarized target experiment [60] had large uncertainties. At Bates, the AHEAD deuteron polarimeter was used [61, 62] to determine t_{20} in the range just past the minimum of t_{20} to just past the node in G_C. A continuation of the Novosibirsk experiment had large uncertainties [63], and was never published. Note that, to facilitate comparison between different experiments, the data are often "corrected" to an electron scattering angle of 70°, but this adjustment and the uncertainty it introduces are small.

Over the past several years, internal target experiments at NIKHEF [64, 65] and

Novosibirsk [66] have improved the precision of the lower Q^2 data, over a range of $Q \approx$ 0.3 - 0.8 GeV. The improvements in Novosibirsk include higher luminosity resulting from an improved atomic beam source and a modified beam tune that allows use of a higher impedance storage cell. JLab Hall C E94-018 [4] used the recoil polarimeter POLDER to measure to the highest Q^2, 1.72 GeV^2.

The overlap of the data is good, but apparent systematic shifts can be seen, as the NIKHEF and Bates measurements are more negative than the JLab and Novosibirsk measurements; note that this is not a difference between polarized targets and recoil polarimeters. The issue of determing at what Q^2 $G_C = 0$ is affected by this difference. The Bates data [61, 62] suggest a larger Q^2 than do the Novosibirsk [66] and JLab [4] data. The fits of Ref. [30] do not include the unpublished Novosibirsk data [63, 66], and average between the Bates and JLab points.

We do not discuss the data for t_{21} and t_{22}. Because of their dependence on G_M, they have not been as useful in providing new information as has t_{20}. To test time reversal invariance, one measurement of the *induced* vector polarization was made [67]. The observed result was consistent with zero.

3.3. Nonrelativistic calculations without interaction currents

3.3.1. Theory It is instructive to see how the deuteron form factors are related to the free nucleon form factors and the deuteron wave function in the nonrelativistic limit. Because the deuteron is an isoscalar target, only the isoscalar nucleon form factors

$$
\begin{aligned}
G_E^s &= G_E^p + G_E^n \\
G_M^s &= G_M^p + G_M^n
\end{aligned}
\tag{31}
$$

will contribute to the form factors. In the nonrelativistic theory, *without exchange currents or $(v/c)^2$ corrections*, the deuteron form factors are

$$
\begin{aligned}
G_C &= G_E^s D_C \\
G_Q &= G_E^s D_Q \\
G_M &= \frac{m_d}{2m_p} \left[G_M^s D_M + G_E^s D_E \right],
\end{aligned}
\tag{32}
$$

where the *body form factors* D_C, D_Q, D_M, and D_E are all functions of Q^2. If we choose to evaluate these in the Breit frame, defined by

$$
q_0 = \nu = 0, \quad D_0 = \sqrt{m_d^2 + \tfrac{1}{4}\mathbf{q}^2}, \quad d^\mu = \left\{ D_0, -\tfrac{1}{2}\mathbf{q} \right\}, \quad d'^\mu = \left\{ D_0, \tfrac{1}{2}\mathbf{q} \right\},
\tag{33}
$$

then the relativistic and nonrelativistic momentum transfers are identical, $Q^2 = \mathbf{q}^2$, and the relativistic nucleon form factors can be used without corrections. Note that, in this nonrelativistic limit, only the nucleon electric form factors contribute to the deuteron charge and quadrupole structure, while both nucleon form factors contribute to the deuteron magnetic structure.

The nonrelativistic formulae for the body form factors D involve overlaps of the wave functions, weighted by spherical Bessel functions

$$
D_C(Q^2) = \int_0^\infty dr \left[u^2(r) + w^2(r) \right] j_0(\tau)
$$

$$D_Q(Q^2) = \frac{3}{\sqrt{2}\eta} \int_0^\infty dr \, w(r) \left[u(r) - \frac{w(r)}{\sqrt{8}} \right] j_2(\tau)$$

$$D_M(Q^2) = \int_0^\infty dr \left[2\, u^2(r) - w^2(r) \right] j_0(\tau) + \left[\sqrt{2}\, u(r)w(r) + w^2(r) \right] j_2(\tau)$$

$$D_E(Q^2) = \frac{3}{2} \int_0^\infty dr \, w^2(r) \left[j_0(\tau) + j_2(\tau) \right] \tag{34}$$

where $\tau = qr/2 = Qr/2$. At $Q^2 = 0$, the body form factors become

$$D_C(0) = \int_0^\infty dr \left[u^2(r) + w^2(r) \right] = 1$$

$$D_Q(0) = \frac{m_d^2}{\sqrt{50}} \int_0^\infty r^2 \, dr \, w(r) \left[u(r) - \frac{w(r)}{\sqrt{8}} \right]$$

$$D_M(0) = \int_0^\infty dr \left[2\, u^2(r) - w^2(r) \right] = 2 - 3P_D$$

$$D_E(0) = \frac{3}{2} \int_0^\infty dr \, w^2(r) = \frac{3}{2} P_D \tag{35}$$

giving the nonrelativistic predictions

$$Q_d = D_Q(0)$$

$$\mu_d = \mu_s (2 - 3\, P_D) + 1.5\, P_D = 1.7596 - 1.1394\, P_D, \tag{36}$$

with $\mu_s = 0.8798$ the isoscalar nucleon magnetic moment. The experimental value of the deuteron magnetic moment (in these units) is 1.7139, leading to a predicted D-state probability of $P_D = 4.0\%$. However this estimate cannot be taken too seriously because the magnetic moment is *very sensitive to relativistic corrections and interaction currents* which can easily alter this result significantly. These contributions will be reviewed qualitatively later in this review.

The study of deuteron form factors is complicated by the fact that they are a *product* of the *nucleon isoscalar* form factors, G^s, and the *body* form factors, D. The dependence of the deuteron form factors on older models of the nucleon form factors is well discussed in Ref. [8]. A year ago the model of Mergell, Meissner and Drechsel [68] (referred to as MMD) gave a good fit, and could have been adopted as a standard. Figure 4 shows the MMD isoscalar electric and magnetic form factors divided by the familiar dipole form factor

$$F_D(Q^2) = \left(1 + \frac{Q^2}{0.71} \right)^{-2} \tag{37}$$

(with Q^2 in GeV^2). Note that the MMD model does not differ by more than 20% from the dipole over the entire Q^2 range, suggesting that the dipole approximation works very well (on the scale of the experimental errors – see below). However, recent measurements of the proton charge form factor are producing a surprising result, and at the time this review was being completed the picture was begining to change.

The recent JLab measurements of both the neutron and proton charge form factors now suggest that the isoscalar charge form factor may be well approximated by

$$G_E^{s\,\mathrm{JLab}}(Q^2) = \left\{ \frac{1.91\tau}{(1 + 5.6\tau)} + (1.0 - 0.1262\, Q^2) \right\} F_D(Q^2). \tag{38}$$
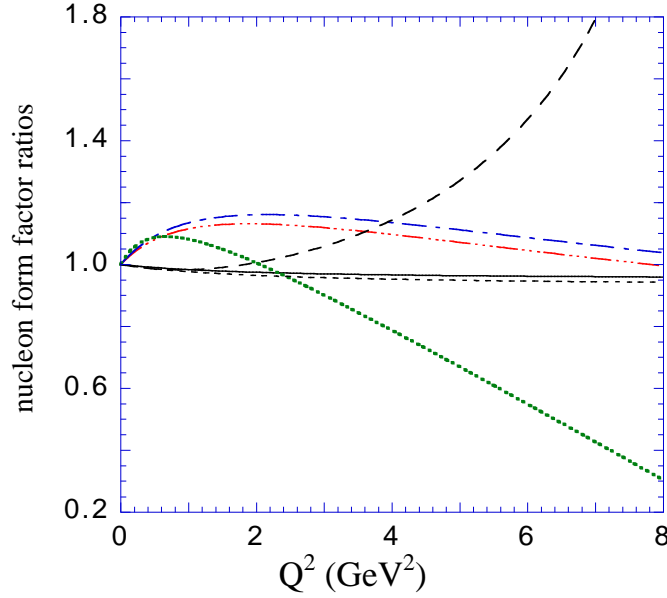
Figure 4. Ratios of the nucleon isoscalar form factors: $G_E^s(\text{MMD})/F_D$ (triple-dot-dashed line), $G_M^s(\text{MMD})/(\mu_s F_D)$ (dot-dashed line), $\mu_s G_E^s(\text{MMD})/G_M^s(\text{MMD})$ (Solid line), $G_E^{s,\text{JLab}}/F_D$ (dotted line), F_1^s/G_E^s (MMD) (short dashed line), and F_1^s/G_E^s (JLab) (long dashed line).

where F_D is the dipole form factor and $\tau = Q^2/4m_p^2$. This JLab model is a sum of the old Galster [34] fit for the nucleon charge form factor (supported by the recent measurements [69]) and a linear approximation to the new JLab $G_E^p/G_M^p$ data [46] (from which the charge form factor is obtained by assuming that $G_M^p = \mu_p F_d$). Figure 4 shows that this form factor differs significantly from the dipole (and also the previously favored MMD model), and may have a significant affect on the theoretical interpretation of the data. This will be discussed in Sec. 3.8 below. [The F_1/G_E ratios shown in the figure will be discussed in Sec. 3.6.6 below.]

Dividing the individual factors A_C, A_Q, and A_M [introduced in Eq. (24)] by $(G_E^s)^2$ gives reduced quantities that are (except for the weak dependence on the ratio of $G_{Ms}/\mu_s G_{Es}$) independent of the choice of nucleon form factor. The contribution of these reduced quantities, which we denote by a_C, a_Q, and a_M, to the total $a = A/(G_E^s)^2$ is shown in Fig. 5. The figure shows that the contribution of the magnetic term, a_M, to the total a is small for $Q^2 < 4$ GeV^2 (for most of the Q^2 range it is less than a few percent, reaching 10% at $Q^2 \simeq 0.5$ and also near 4 GeV^2). Above Q^2 of 4 GeV^2 it is larger, and very model dependent. This justifies the observation that the A structure function can be well approximated by $\tilde{A}$, as stated earlier in Eq. (27). [Note that the new JLab data for G_E^p, discussed briefly above, may enhance the magnetic contributions to A above 4 GeV^2, but will not change these conclusions qualitatively].

3.3.2. Comparison to data How well does this simple nonrelativistic theory explain the data? The high Q^2 data for A provide the most stringent test. In Fig. 6 we compare
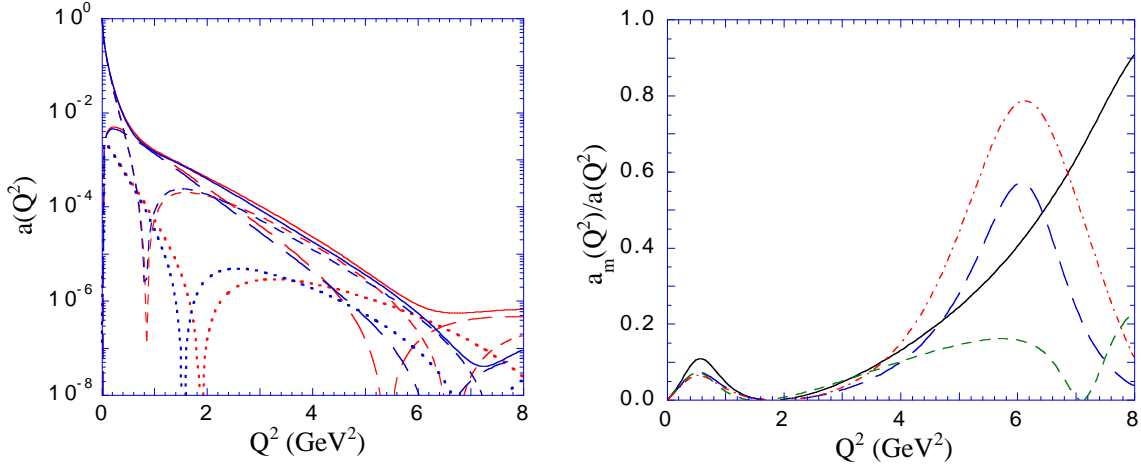
Figure 5. Plots of $a(Q^2)$ and the ratio $a_m(Q^2)/a(Q^2)$ discussed in the text. Left panel shows contributions for models AV18 and IIB-nonrelativistic: a (solid lines), a_q (long dashed lines), a_c (short dashed lines), a_m (dotted lines). In these plots the ratio G_M^s/G_E^s is fixed at μ_s. In each case IIB decreases more rapidly than AV18 at low Q^2. Right panel: IIB-RIA (solid line), AV18 (long dashed line), IIB-nonrelativistic (short dashed line), all with $G_M^s/G_E^s = \mu_s$, and AV18 with the ratio of G_M^s/G_E^s given by Eq. (38) (dot-dashed line).
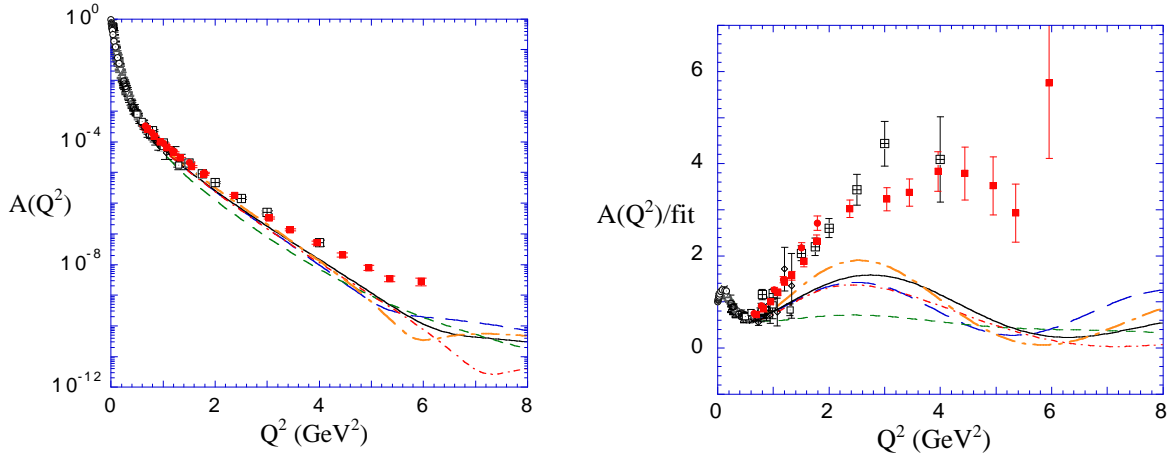
Figure 6. The structure function A for the five nonrelativistic models discussed in the text, calculated using the MMD nucleon form factors. The models are labeled as in Figs. [1] and [2]. The left panel shows data and models divided by a "fit" described in the text. See Table 2 for references to the data.

the data for A with calculations using the five nonrelativistic wave functions shown in Figs. 1 and 2. The calculations use Eq. (32) with MMD isoscalar nucleon form factors and nonrelativistic body form factors given in Eq. (34). In the right panel the data and models have been divided by the "fit" described in Eq. (39) below.
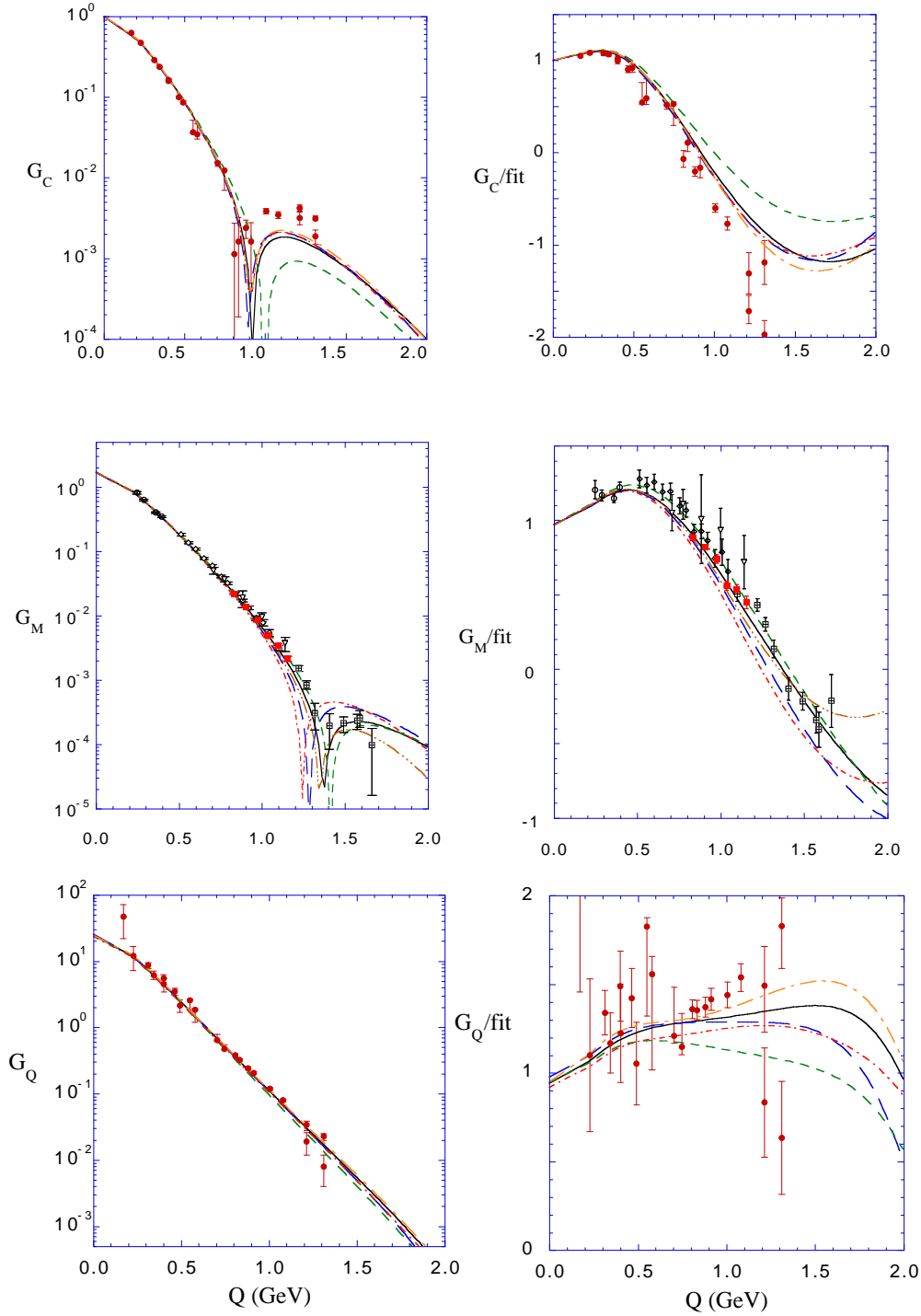
Figure 7. Deuteron form factors for the five nonrelativistic models compared to data. The data for G_C and G_Q are from analysis of the complete A and t_{20} data sets [30]. The data for G_M were extracted from the experimental measurements of B, referenced in Table 3. MMD nucleon form factors have been used with the nonrelativistic models.
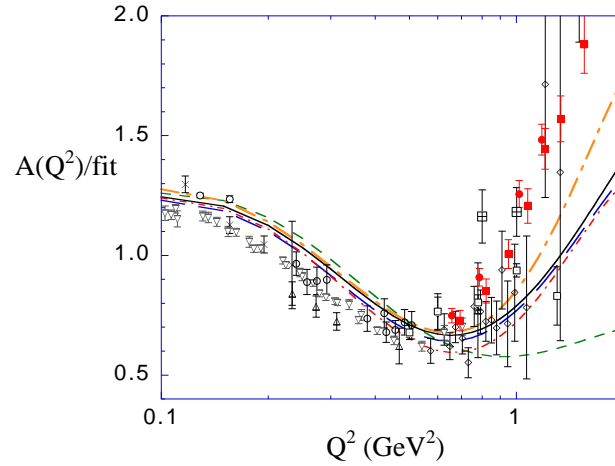
Figure 8. The structure function A for the five nonrelativistic models discussed in the text. The models are labeled as in Figs. [1] and [2]. See Table 2 for references to the data.

It is easy to see that the nonrelativistic models *are a factor 4 to 8 smaller than the data for $Q^2 > 2$ GeV^2*. Furthermore, since the difference between different deuteron models is substantially smaller than this discrepancy, it is unlikely that any *realistic* nonrelativistic model can be found that will agree with the data. If the nucleon isoscalar charge form factor were larger than the MMD model by a factor of 2 to 3 it might explain the data, but this is also unlikely since the variation between nucleon form factor models is substantially smaller than this. [If we use the fit Eq. (38) to the JLab G_{Ep} measurements the discrepancy will be even larger.] We are forced to conclude that these high Q^2 measurements *cannot be explained by nonrelativistic physics and present very strong evidence for the presence of interaction currents, relativistic effects, or possibly new physics.*

A detailed comparison of the nonrelativistic models with the three deuteron form factors, G_C, G_M, and G_Q is given in Fig. 7. The functions used to scale the data and theory in the right-hand panels of the figure are

$$G_C = e^{-Q^2/3.5} \left(1 + \frac{Q^2}{m\epsilon}\right)^{-1} \left(1 + \frac{Q^2}{0.71}\right)^{-2}$$

$$G_M = 1.7487\, e^{-Q^2/2.5} \left(1 + \frac{Q^2}{m\epsilon}\right)^{-1} \left(1 + \frac{Q^2}{0.71}\right)^{-2}$$

$$G_Q = \frac{25.8298}{1.01} \left(e^{-Q^2} + 0.01\, e^{-Q^2/100}\right) \left(1 + \frac{Q^2}{m\epsilon}\right)^{-1} \left(1 + \frac{Q^2}{0.71}\right)^{-2}. \quad (39)$$

where Q^2 is in GeV^2 and $m\epsilon = 0.936 \times 0.0022246/0.197^2$. While some of the factors in these expressions are theoretically motivated (note the presence of the dipole form of the nucleon form factor) we do not attach *any* theoretical significance to these functional

forms; they merely provide a reasonably simple way to scale out the rapid exponential decreases from the form factors. Figure 7 shows that the nonrelativistic models do a good job of predicting the form factors to a momentum transfer $Q \simeq 0.5$ GeV, beyond which departures from the data and variations of the models make the agreement increasingly unsatisfactory.§

However, careful comparison reveals that there are still (small) discrepancies between the data and the nonrelativistic theory, even at low Q^2. The data and curves from the lower panel of Fig. 6 are shown on an expanded logarithmic scale in Fig. 8. In the lowest Q^2 range from about 0.15 to 0.4 GeV^2 the data lie *below* the nonrelativistic theory, and are larger than the nonrelativistic theory only for Q^2 above 1 GeV^2. The very low Q^2 discrepancy seems to be due in part (but not entirely) to the Columb distortion corrections that have been used recently to explain the deuteron radius [44]. We will discuss these corrections in Sec. 3.6 below.

Before we turn to a detailed discussion of the possible explanations for the failure of nonrelativistic models to explain the form factors at high Q^2, we discuss the low momentum transfer results from the perspective of effective theories.

3.4. Effective field theory

The recent development of effective field theory provides a powerful method for theoretical study of low Q^2 physics. We will briefly review these results here, and return to the discussion of the high Q^2 results in the next section.

Effective field theory techniques exploit the fact that the physics at low energies $E \ll M_0$ (or large distances $\lambda \gg \lambda_0 = 1/M_0$) cannot be sensitive to the *details* of the interactions at very high energies $E \gg M_0$ (or short distances). For example, a low energy long wavelength probe may detect the presence of a small scattering center, but cannot resolve its structure (much as the far-field of a collection of electric charges depends on only one parameter, the total charge). The parameters that depend on the short-range physics may be very important, but they cannot be calculated and must be determined by a fit to the data.

Effective field theory works best if the distance scales of the (unknown) short-range physics and the (known) long-range physics are clearly separated. Then for energies well below the scale of the short-range physics (which we take to be M_0), the short-range physics is treated systematically by expanding in powers of E/M_0. In applications to the NN system, two scales have been discussed. The so-called "pionless theory" chooses $M_0 \sim m_\pi$, and therefore requires no theory of the πN interaction. This approach can work only at *very* low energies. The chiral theory chooses $M_0 \sim m_\rho$

§ We are not inclined to take the discrepancy between theory and the first G_Q point seriously; kinematic factors make it difficult to extract this point accurately and it is only one standard deviation from the theory. The large G_Q and small G_C values for the points at 0.55 GeV and 0.58 GeV result from the t_{20} data points, from [65] and [59] respectively, being about 1 standard deviation more negative than calculations and overlapping the negative limit for t_{20} of $-\sqrt{2}$. Note that the tabulated uncertainty of G_Q at $Q = 0.55$ GeV in Ref. [4] should be asymmetric, $+0.075/-0.713$, (as shown in the Fig. 7).

and attempts to describe NN scattering up to the ρ mass scale using the known pion-nucleon interaction as given by chiral symmetry. (More precisely, if the magnitude of the center of mass relative momentum $|\mathbf{p}| < M_0/2$, the nucleon lab kinetic energy will $E_{\text{lab}} < M_0^2/2m$, which is $E_{\text{lab}} < 10$ MeV for the pionless theory, and $E_{\text{lab}} < 320$ MeV for chiral perturbation theory.)

The effective range theory introduced by Bethe [70] is an early version of what we now call the pionless effective theory. Weinberg [71] first applied modern chiral perturbation theory to NN scattering. He proposed making a chiral expansion of the NN potential, and then inserting this potential into the Schrödinger equation. Later Kaplan, Savage, and Wise (KSW) [72] criticized the consistency of this approach, and introduced an alternative organizational scheme, sometimes referred to as Q counting, in which the pion interaction is to be included as a perturbative correction (as opposed to including it as part of the potential, and counting it to all orders, as proposed by Weinberg). KSW applied this method to calculation of the deuteron form factors [73]. It is now known that the tensor part of the one pion exchange interaction is too strong to be treated perturbatively, and recent work has focused on how to include the singular parts of one pion exchange in the most effective manner [74, 75]. In the following discussion we review the recent results from Phillips, Rupak, and Savage (PRS), who give a nice account of the calculations of the deuteron form factors in a pionless theory [74].

The effective Lagrangian density for a pionless effective theory of the NN interaction in any channel (the coupled $^3S_1 - ^3D_1$ for example) is

$$\mathcal{L} = - C_0 \left(\psi^{\mathrm{T}} \psi \right)^{\dagger} \left(\psi^{\mathrm{T}} \psi \right)$$
$$- \tfrac{1}{2} C_2 \left[\left(\psi^{\mathrm{T}} \psi \right)^{\dagger} \left(\nabla^2 \psi^{\mathrm{T}} \psi + \psi^{\mathrm{T}} \nabla^2 \psi - 2 \vec{\nabla} \psi^{\mathrm{T}} \cdot \vec{\nabla} \psi \right) + \mathrm{h.c.} \right]$$
$$+ \cdots , \tag{40}$$

where ψ is a (nonrelativistic) nucleon field operator and C_0, C_2, and the general coefficient C_{2n} (which fixes the strength of the terms with $2n$ derivatives) are determined from data. The coefficients C_{2n} parameterize the strength and shape of the short range interaction. The scattering amplitude predicted by (40) is a sum of bubble diagrams which can be regularized using the KSW dimensional regularization scheme with power law divergence subtraction [72]. In lowest order (LO) this bubble sum is

$$\mathcal{M} = \frac{-C_0(\mu)}{1 + \dfrac{m}{4\pi} C_0(\mu)(\mu + ip)} = \frac{4\pi}{m} \left(\frac{1}{p \cot \delta_0 - ip} \right)$$
$$= -\frac{4\pi}{m} \left(\frac{Z_d}{\gamma + ip} \right) + R(p) \tag{41}$$

where p is the magnitude of the nucleon three-momentum in the c.m. system, $R(p)$ is regular at the pole $p = i\gamma$, $\gamma = \sqrt{m\epsilon}$ with ϵ the deuteron binding energy, Z_d is related to the asymptotic normalization of the deuteron wave function, and the dependence of C_0 on the (arbitrary) renormalization point μ is dictated by the requirement that the
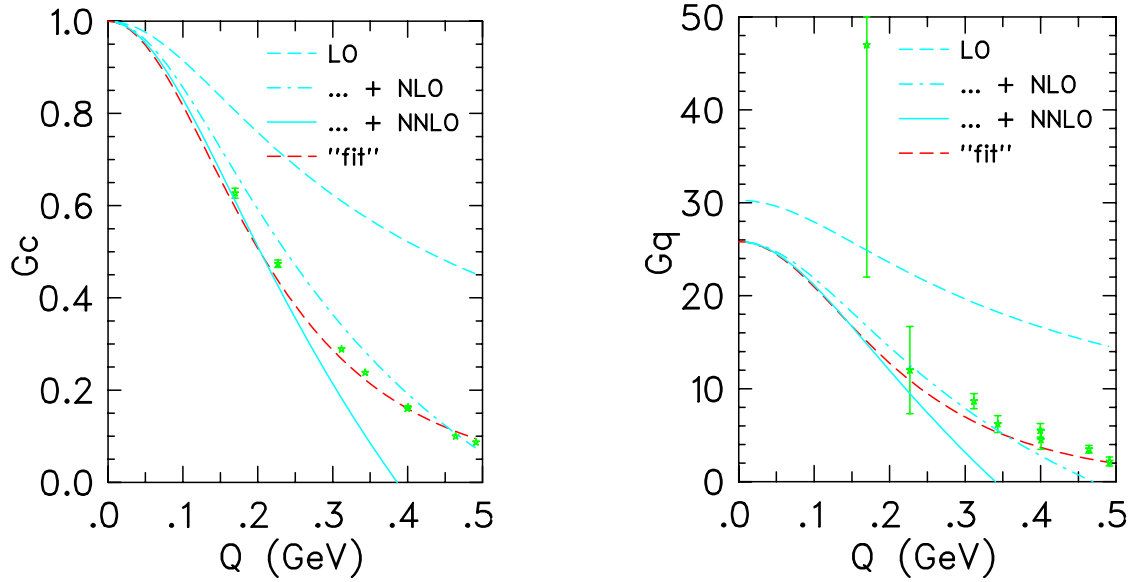
Figure 9. Predictions of the charge and quadruple deuteron form factors from the pionless effective theory, as developed by PRS [74]. The data were extracted in Ref. [30] and previously shown in Fig. 7. The "fits" are from Eq. (39).

overall result be *independent* of μ. The LO result is

$$C_0(\mu) = \frac{4\pi}{m}\left(\frac{1}{\gamma - \mu}\right), \qquad Z_d = 1, \qquad R(p) = 0. \tag{42}$$

In terms of the effective range expansion

$$p \cot \delta_0 = -\frac{1}{a} + \tfrac{1}{2}\rho_d(p^2 + \gamma^2) + w_2(p^2 + \gamma^2)^2 + \cdots \tag{43}$$

with a the scattering length and ρ_d the effective range, the LO calculation gives

$$a = 1/\gamma, \qquad \rho_d = 0. \tag{44}$$

Contributions from the next to leading order (NLO) term C_2 changes the relations in (42) and (44); in particular, the wave function renormalization constant Z_d begins to differ from unity and the effective range ρ_d to differ from zero. PRS point out that the most stable results are obtained by constraining C_0 and C_2 to give the experimental values of the deuteron parameters $\gamma^{-1} = 4.319$ fm and $Z_d - 1 = 0.690$ instead of γ and $\rho_d = 1.765$ fm. This is because the asympotic deuteron wave function is fixed by γ and Z_d

$$\psi_{\text{tail}}(r) = \sqrt{\frac{\gamma Z_d}{2\pi}} \frac{e^{-\gamma r}}{r} \tag{45}$$

and *it is the wave function and not the scattering* that largely determines the deuteron form factors and other electromagnetic observables.

Using this approach, the LO charge form factor is given entirely by the asymptotic wave function (45)

$$G_C^{(0)}(Q^2) = \frac{4\gamma}{q} \tan^{-1} \frac{q}{4\gamma}, \tag{46}$$

where $q = |\mathbf{q}|$ is the magnitude of the three momentum transferred by the electron, and working in the Breit frame (where the differences between relativistic and nonrelativistic theory is a minimum) is also equal to $\sqrt{Q^2}$. PRS show that expansion of the charge form factor up to NNLO terms is

$$G_C(Q^2) = G_C^{(0)}(Q^2) - (Z_d - 1)\left[1 - G_C^{(0)}(Q^2)\right]$$
$$- \frac{1}{6}r_N^2\, Q^2\, G_C^{(0)}(Q^2) + \cdots \tag{47}$$

and because the wave function is correctly normalized, there are no wave function effects beyond NLO (the second term). At NNLO effects from the finite nucleon size, r_N, appear. Similarly, the LO quadrupole form factor obtained by PRS is

$$G_Q^{(0)}(Q^2) = \frac{3m_d^2\,\eta_{sd}}{2\sqrt{2}\gamma q^3}\left[4q\gamma - (3q^2 + 16\gamma^2)\tan^{-1}\frac{q}{4\gamma}\right] \tag{48}$$

with η_{sd} the asymptotic S/D-state ratio, and the LO quadrupole moment, Q_d^{LO}, equal to $\eta_{sd}/\sqrt{2}\gamma^2 = 0.335$ fm^2. The expansion of G_Q to NNLO is then

$$G_Q(Q^2) = G_Q^{(0)}(Q^2) + m_d^2\,\Delta Q_d + (Z_d - 1)\left[G_Q^{(0)}(Q^2) - m_d^2 Q_d^{LO}\right]$$
$$- \frac{1}{6}r_N^2\, Q^2 G_Q^{(0)}(Q^2) + \cdots \tag{49}$$

Note that the quadrupole moment at NLO includes a contribution ΔQ_d from a four-nucleon-one-photon contact term, not determined by NN scattering, and is used to fit the experimental value of Q_d. PRS suggest that the absence of this piece of short distance physics in conventional calculations may explain their underprediction of the quadrupole moment. The finite size of the nucleon again comes in at NNLO.

With parameters largely set by other data, the deuteron charge, quadrupole, and magnetic form factors are well predicted up to about $Q = 0.2$ GeV, as shown in Fig. 9. The approach seems to converge well, but beyond NNLO more parameters enter, and there is less predictive power. The great strength of the pionless effective theory is that strips away complexity, revealing the essential physics required to understand the low Q results, and showing (for example) the central importance of the asympotic S-state normalization Z_d. However, as expected, it clearly does not work for Q much beyond 0.4 to 0.5 GeV. The theory with pions (sometimes referred to as a "pionful" theory) will work to higher Q^2 [75]. Removal of divergences from these theories is under active study.

We now return to discussion of the reasons for the failure of nonrelativistic theory at high Q^2.

3.5. Alternative explanations for the failure of nonrelativistic models

In Sec. 3.3.2 we showed that the naive nonrelativistic theory cannot explain the deuteron form factor data for $Q \geq 0.5$ GeV. In this section we classify the possible explanations for this failure, preparing the way for detailed discussions to follow in Secs.3.6 and 3.7.

The differences between the data and the nonrelativistic theory can only be explained by a combination of the following effects
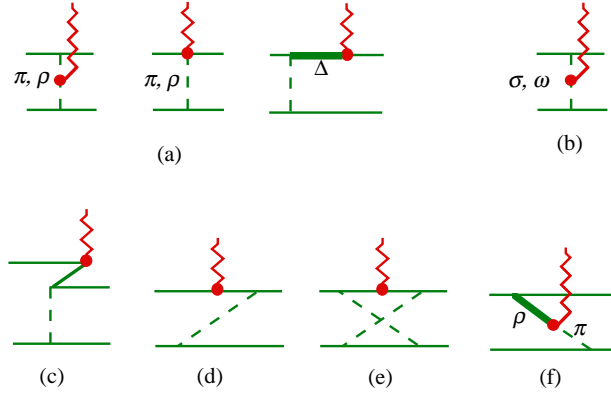
Figure 10. Exchange currents that might play a role in meson theories. (a) Large $I = 1$ π, ρ, and Δ currents that do not contribute to the deuteron form factors, and (b) possible $I = 0$ currents that are identically zero. The currents that do contribute to the deuteron form factors are shown in the second row: (c) "pair" currents from nucleon Z-graphs; (d) "recoil" corrections; (e) two pion exchange (TPE) currents; and (f) the famous $\rho\pi\gamma$ exchange current.

- interaction (or meson exchange) currents;
- relativistic effects; or
- new (quark) physics.

The only possibilities excluded from this list are variations in models of the nucleon form factors, or model dependence of the deuteron wave functions. In the previous section we argued that *neither* the current uncertainty in our knowledge of the nucleon form factors, *nor* the model dependence of the nonrelativistic deuteron wave functions are sufficient to provide an explanation for the discrepencies.

Possible interaction currents that might account for the discrepency are shown in Fig. 10. Because the deuteron is an isoscalar system, the familiar large $I = 1$ exchange currents are "filtered" out and only $I = 0$ exchange currents can contribute to the form factors. The $I = 0$ currents tend to be smaller and of a more subtle origin. The nucleon Z-graphs, Fig. 10c, and the recoil corrections, Fig. 10d, are both of relativistic origin. (The recoil graphs will give a large, incorrect answer unless they are renormalized [76, 77, 78].) The two-meson exchange currents should be omitted unless the force also contains these forces. The famous $\rho\pi\gamma$ exchange current is very sensitive to the choice of $\rho\pi\gamma$ form factor, which is hard to estimate and could easily be a placeholder for new physics arising from quark degrees of freedom.

In most calculations based on meson theory, the two pion exchange (TPE) forces and currents arising from crossed boxes are excluded, and, except for the $\rho\pi\gamma$ current (which we will regard as new physics), the exchange currents are of relativistic origin. Additional relativistic effects arise from boosts of the wave functions, the currents, and the potentials, which can be calculated in closed form or expanded in powers of $(v/c)^2$, depended on the method used. At low Q^2 calculations may be done using effective field

theories (discussed in Sec. 3.4) in which a small parameter is identified, and the most general (i.e. exact) theory is expanded in a power series in this small parameter. In these calculations relativistic effects are automatically included (at least in principle) through the power series in $(v/c)^2$. *Hence any improvement on nonrelativistic theory using nucleon degrees of freedom leads us to relativistic theory.*

Alternatively, one may seek to explain the discrepancy using quark degrees of freedom (new physics). When two nucleons overlap, their quarks can intermingle, leading to the creation of new NN channels with different quantum numbers (states with nucleon isobars, or even, perhaps, so-called "hidden color" states). These models require that assumptions be made about the behavior of QCD in the nonperturbative domain, and are difficult to construct, motivate, and constrain. At very high momentum transfers it may be possible to estimate the interactions using perturbative QCD (pQCD). Very little has been done using other approaches firmly based in QCD, such as lattice gauge theory or Skrymions (but see Ref. [79]).

We are thus led to two different alternatives for explanation of the failure of nonrelativistic models. In one approach the nucleon (hadron) degrees of freedom are retained, and relativistic methods are developed that treat boost and interaction current corrections consistently. In another approach, quark degrees of freedom are used to describe the short range physics, and techniques for handling a multiquark system in a nonperturbative (or perturbative) limit are developed. These two approaches will be reviewed in the next two sections. While the discussion appears to be focused on the deuteron form factors, it is actually more general, and will be applied later to the treatment of deuteron photodisintegration.

Are these two approaches really different? Superficially, of course, the answer must be: Yes! However, QCD tells us that all physical states must be color singlets, and a basis of states that describes any color singlet state can be constucted from *either* quarks (and gluons) *or* hadrons (this would not be true if colored states were physical). So at a deeper level it appears that either approach (hadrons or quarks) should work, and the best choice is the system that can describe the relevant physics more compactly. Further discussion of this issue is clearly beyond the scope of this review.

3.6. Relativistic calculations using nucleon degrees of freedom

This long section is divided into six parts as follows: (i) Introduction, (ii) Overview of propagator dynamics, (iii) Choice of propagator and kernel, (iv) Examples of propagator dynamics, (v) Overview of hamiltonian dynamics, and (vi) Examples of hamiltonian dynamics.
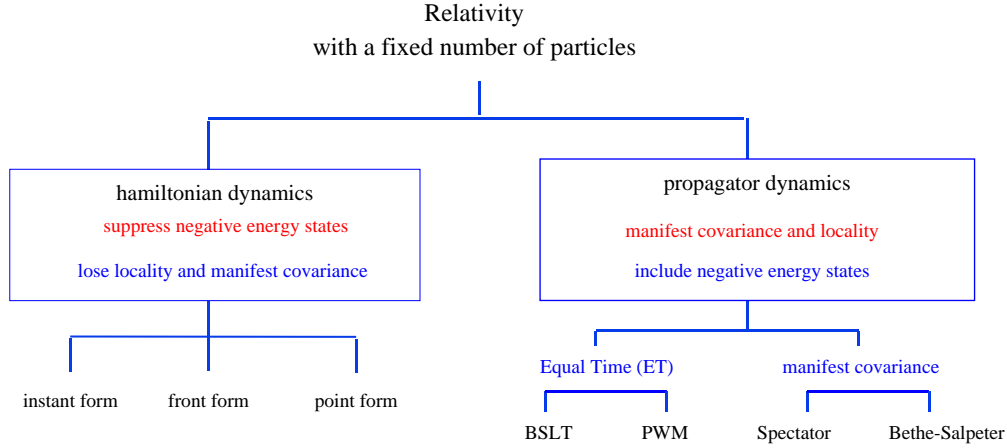
3.6.1. Introduction The inhomogeneous Lorentz group, or the Poincaré group, is described by 10 generators: three pure rotations, three pure boosts, and four pure translations. If we require the interactions to be local and manifestly covariant under the Poincaré group, we are led to a local relativistic quantum field theory with particle

production and annihilation [80]. In this case the Poincaré transformations of all matrix elements can be shown to depend only on the kinematics (i.e. they depend only on the masses and spins of the external particles). The disadvantage is that the number of particles is not conserved. If perturbation theory can be used, this approach is very successful, but in the nonperturbative regime of strong coupling meson theory it leads to an infinite set of coupled equations that cannot be solved in closed form. Numerical, nonperturbative solutions of field theory can be obtained in Euclidean space for a few special cases [81]. Methods that limit the intermediate states to a *fixed number of particles* (two nucleons in this case) are more tractable, and all modern calculations are based on the choices depicted in the decision tree shown in Fig. 11.

In deciding which method to use, if is first necessary to decide whether or not to allow *antiparticle, or negative energy* nucleons to propagate as part of the virtual intermediate state. Since nucleons are heavy and composite, so that their antiparticle states are very far from the region of interest, some physicists believe that intermediate states should be built only from positive energy nucleons, and that all negative energy effects (if any) should be included in the interaction. These methods are referred to collectively as *hamiltonian dynamics* and are represented by the left hand branch in the figure. Unfortunately, it turns out that this choice precludes the possibility of retaining the properties of locality and manifest covariance enjoyed by field theory. Alternatively, in order to keep the locality and manifest covariance of the original field theory, other physicists are willing to allow negative energy states into the propagators. These methods, represented by the right-hand branch of the figure, are referred to collectively as *propagator dynamics*. Including negative energy states tends to make calculations technically more difficult and harder to interpret physically, and those who advocate the use of hamiltonian dynamics do not believe the advantages of exact covariance justify the work it requires.

Unfortunately, these two methods are so fundamentally different that many physicists do not realize that the limitations of one may not apply to the other. For example, for some choices of propagator dynamics all 10 of the generators of the Poincaré group will depend only on the kinematics, and the Poincaré transformations of *all amplitudes can be done exactly*. With hamiltonian dynamics this is not the case; some of the 10 generators must depend on the interaction, and transformation of matrix elements under these "dynamical" transformations must be calculated. Comparison of the two methods is therefore very difficult; the language and issues of each are very different and one can be easily misled by the different appearance of the results. We cannot discuss these issues in detail in this review, and refer the reader to two recent references that survey the subject [76, 82]. Here we will give a short review of some recent calculations, and explain these differences as we go along.

3.6.2. Overview of propagator dynamics   Propagator calculations all start from the field theory description of two (in this case) interacting particles. While some may prefer to express the field theory as a path integral, it is also possible to adopt a more intuitive

Relativity
with a fixed number of particles

hamiltonian dynamics

suppress negative energy states

lose locality and manifest covariance

propagator dynamics

manifest covariance and locality

include negative energy states

instant form   front form   point form

Equal Time (ET)   manifest covariance

BSLT   PWM   Spectator   Bethe-Salpeter

Figure 11. The relativistic decision tree discussed in the text.

approach and imagine expanding the path intergral as a sum of Feynman diagrams (ignoring issues of convergence for the moment). In order to generate the deuteron bound state, which produces as a pole in the scattering matrix, it is necessary to sum an infinite class of diagrams, written as

$$
\mathcal{M}(p, p'; P) = \mathcal{V}(p, p'; P) + \int \frac{d^n k}{(2\pi)^n} \mathcal{V}(p, k; P) G(k, P) \mathcal{V}(k, p'; P)
$$
$$
+ \int \frac{d^n k}{(2\pi)^n} \int \frac{d^n k'}{(2\pi)^n} \mathcal{V}(p, k; P) G(k, P) \mathcal{V}(k, k'; P) G(k', P) \mathcal{V}(k', p'; P)
$$
$$
+ \cdots \tag{50}
$$

where $\mathcal{V}(p, p'; P)$ is the *kernel* being iterated, $G(k, P)$ the two body propagator, $\mathcal{M}(p, p'; P)$ the scattering amplitude, and the other quantities are defined below. This sum is obtained in closed form by solving the integral equation

$$
\mathcal{M}(p, p'; P) = \mathcal{V}(p, p'; P) + \int \frac{d^n k}{(2\pi)^n} \mathcal{V}(p, k; P) G(k, P) \mathcal{M}(k, p'; P). \tag{51}
$$

If the series (50) is compared to a geometric series $1 + z + z^2 + \cdots$, then the solution to the integral equation (51) can be compared to the sum of the geometric series $1/(1-z)$. The geometric series converges only when $|z| < 1$, but its unique analytic continuation, $1/(1-z)$, is valid for all z. Similiarly, it is assumed that the solution to (51) is valid even when the series (50) diverges. And just as the geometric series has a pole at $z = 1$, the solution to (51) will have a pole at $P^2 = m_d^2$, the square of the deuteron mass.

The amplitudes $\mathcal{V}$, G, and $\mathcal{M}$ are all matrices in the NN spin-isospin space, and are functions of the four-momenta $P = p_1 + p_2$ and $p = (p_1 - p_2)/2$, with p_1 and p_2 the momenta of the two particles (labeled in Fig. 12). The dimension of the volume integration is n, normally either 3+1=4 (3 space + one time dimensions) for the Bethe-Salpeter method, or 3+0=3 for the quasipotential methods described below.

If Eq. (51) has a homogenous solution at some external four momentum $P_0^2 = m_d^2$, the scattering matrix will have an s channel pole (represented in Fig. 13), signifying the
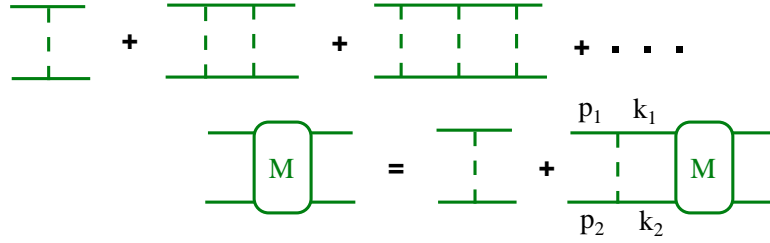
Figure 12. The summation of ladder diagrams leads to the covariant scattering equation.
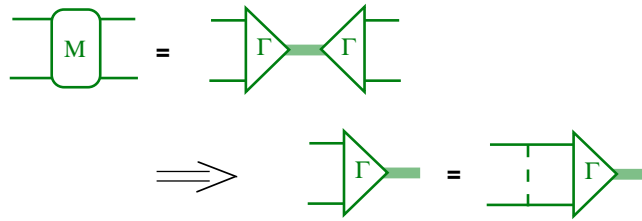
Figure 13. The bound state equation holds near the pole in the scattering amplitude.

existence of a deuteron bound state. The *vertex* function for the deuteron bound state satisfies the equation

$$\Gamma(p; P_0) = \int \frac{d^n k}{(2\pi)^n} \mathcal{V}(p, k; P) G(k, P_0) \Gamma(k; P_0) \tag{52}$$

with covariant normalization condition

$$1 = -\int \frac{d^n k}{(2\pi)^n} \Gamma(k; P_0) \frac{\partial G(k, P_0)}{\partial P_0^2} \Gamma(k; P_0)$$
$$-\int \frac{d^n k}{(2\pi)^n} \int \frac{d^n k'}{(2\pi)^n} \Gamma(k'; P_0) G(k', P_0) \frac{\partial V(k', k; P_0)}{\partial P_0^2} G(k, P_0) \Gamma(k; P_0) \,. \tag{53}$$

The covariant bound state wave function is defined by

$$\Psi(p; P_0) = G(p; P_0)\, \Gamma(p; P_0) \,. \tag{54}$$

One of the advantages of the propagator approach is that the construction of the current operator is comparatively straightforward. It follows (at least in principle) from summing all electromagnetic interactions with all the consituents everywhere in the ladder sum. For bound states described by the Bethe-Salpeter or Spectator formalisms (see the discussion below) there are two diagrams, illustrated in Fig. 14, that can be written

$$\mathcal{J}^\mu(P_0', P_0) = e \int \frac{d^n k_2}{(2\pi)^n} \, \Psi^\dagger \left(\tfrac{1}{2} P_0' - k_2; P_0' \right) \, J_N^\mu(k_1', k_2; k_1, k_2) \, \Psi \left(\tfrac{1}{2} P_0 - k_2; P_0 \right)$$
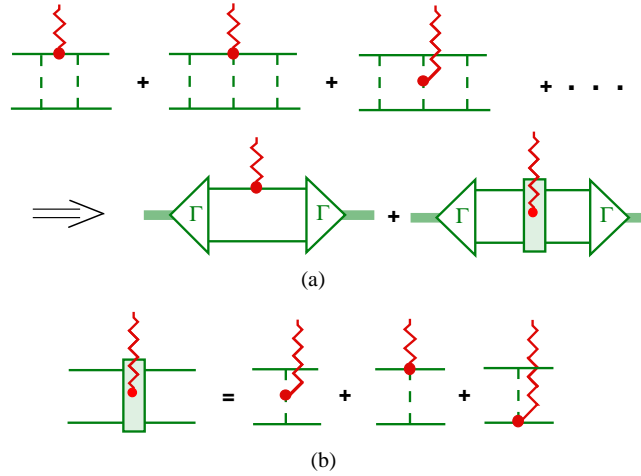
Figure 14. The current operator follows from the electromagnetic interaction of all the consituents in the ladder sum. For bound states, all of these interactions can be collected into the two covariant diagrams shown in panel (a), with the interaction current, shown in panel (b), constructed from $\gamma\phi NN$ and $\gamma\phi\phi$ couplings (where the exchanged meson is denoted by ϕ).

$$+ e \int \frac{d^n k}{(2\pi)^n} \int \frac{d^n k'}{(2\pi)^n} \, \Psi^\dagger(k'; P_0') \, I^\mu(k_1', k_2'; k_1, k_2) \, \Psi(k; P_0) \,. \tag{55}$$

In the first term, J_N^μ is the sum of the neutron and proton currents [recall Eq. (31)] and we have chosen particle 1 to interact with the photon (always possible because of the antisymmetry of the wave function). The interaction current is I^μ, and assumes a comparatively simple form if the kernel is a sum of single particle exchanges. This case is illustrated in Fig. 14.

Current conservation,

$$q_\mu \mathcal{J}^\mu(P_0', P_0) = 0 \,, \tag{56}$$

follows automatically [83] from the bound state equation (52) if the nucleon and interaction currents satisfy the following two-body Ward-Takahashi (WT) identities

$$q_\mu \, J_N^\mu(k_1', k_2'; k_1, k_2) = \tfrac{1}{2}[1 + \tau_3] \left\{ G^{-1}(k; P_0) - G^{-1}(k'; P_0') \right\}$$
$$q_\mu \, I^\mu(k_1', k_2'; k_1, k_2) = \mathcal{V}(k', k; P_0') \tfrac{1}{2}[1 + \tau_3] - \tfrac{1}{2}[1 + \tau_3] \, \mathcal{V}(k', k; P_0) \,. \tag{57}$$

Note the appearance of $\tfrac{1}{2}[1 + \tau_3]$, the isoscalar charge operator in isospin space. The J_N identity is the two-body version of the familiar one-body WT identity

$$q_\mu j_N^\mu(k_1', k_1) = e_N \left\{ S^{-1}(k_1) - S^{-1}(k_1') \right\} \,, \tag{58}$$

with $e_N = e$ (0) for the proton (neutron) and the undressed nucleon propagator normalized to $S_0^{-1}(k_1) = m - \not{k}_1$. Note that the constraint on the interaction current is *not* zero (and hence the interaction current is *not* zero) if the kernel depends on the isospin or the total four-momentum P_0.

3.6.3. Choice of propagator and kernel To fully specify a propagator dynamics, one must choose a propagator, G, a kernel, $\mathcal{V}$, and current operators J_N^μ and J_I^μ.

Four different progagators have been used in the study of the deuteron form factors. The Bethe-Salpeter (BS) equation [17] uses a fully off shell propagator for two nucleons

$$G_{BS}(p, P) = S_1(p_1)S_2(p_2) \rightarrow \frac{\Lambda_1^+ \left(\frac{W}{2} + p\right) \Lambda_2^+ \left(\frac{W}{2} - p\right)}{\left[E_p^2 - \left(\frac{W}{2} + p_0\right)^2\right]\left[E_p^2 - \left(\frac{W}{2} - p_0\right)^2\right]}, \quad (59)$$

where $\Lambda_i(p)/2m = (m_i + \not{p})/2m$ is the (off-shell) positive energy projection operator and the right hand expression is the propagator for identical particles in the rest frame (with $P = \{W, \mathbf{0}\}$, and W used as a shorthand for the four-vector P in the rest frame). This choice of relativistic equation was the first to be introduced and is perhaps the best known. It retains the full integration over all components of the relative four-momentum p, and all of the off-shell degrees of freedom (2 for spin × 2 for "ρ-spin", where $\rho = +$ are positive energy u spinor states and $\rho = -$ are negative energy v spinor states) of both of the propagating nucleons, for a total of $4 \times 4 = 16$ spin degrees of freedom. The equation has inelastic cuts arising from the production of the exchanged mesons (when energetically possible) and additional singularities when the nucleons are off-shell. These can be removed by transforming the equation to Euclidean space. However, the BS equation, when used in *ladder* approximation, does not have the correct one-body limit. Numerical comparisons of solutions obtained from the sum of *all* ladder and crossed ladder exchanges with ladder solutions of the BS equation, carried out for scalar theories, have shown that the ladder sum is inaccurate and that the one-body limit requires inclusion of crossed exchanges [84]. The BS equation has been solved in ladder approximation by Tjon and his collaborators [85], and used to calculate the deuteron form factors [86]. The fits to the NN phase shifts originally obtained from these works are unsatisfactory by today's standards.

The Spectator (or Gross) equation (denoted by S) [18] restricts one of the two nucleons to its positive energy mass-shell. If particle one is on-shell, the spectator propagator is

$$\begin{aligned} G_S(p, P) = {}& 2\pi\, \delta_+(m^2 - p_1^2)\, \Lambda_1(p_1)\, S_2(p_2) \\ & \rightarrow \frac{2\pi\, \delta\left(E_p - \frac{W}{2} - p_0\right) \Lambda_1^+(\hat{p}_1)\, \Lambda_2^+(W - \hat{p}_1)}{2E_p W(2E_p - W)} \end{aligned} \quad (60)$$

where $\hat{p}_1 = \{E_p, \mathbf{p}\}$. This has the effect of fixing the relative energy in terms of the relative three-momentum so as to maintain covariance and reduce the four dimensional integration to three dimensions [$n = 3$ in Eq. (51)]. Identical particles are treated by properly (anti)symmetrizing the kernel. The restriction of one of the particles to its positive energy mass-shell also removes the $\rho = -$ states of one of the nucleons, reducing the number of spin degrees of freedom to 2×4=8. A primary motivation and justification for this approach is that it has the correct one-body limit, and the three body generalization satisfies the cluster property [22]. The equation also has a nice nonrelativistic limit that can be easily interpreted. Numerical studies of

scalar field theories [84] show that the exact ladder and crossed ladder sum is better approximated by the ladder approximation to this equation than it is by the ladder approximation to the BS equation. The method can be extended to include gauge invariant electromagnetic interactions [83]. Its principle drawback is that the kernel has unphysical singularities which can only be removed by an *ad-hoc* prescription. Results from this method will be reviewed in the next section.

The internal momentum integration can also be restricted to three dimensions in such a way that, for equal mass particles in the rest frame, the relative energy is zero and the particles are equally off shell. The Blankenbecler-Sugar-Logunov-Tavkhelidze (BSLT) equation [19] can be defined so that the two propagating particles are on their positive energy mass-shell, reducing the number of spin-ρ-spin variables to $2\times2=4$. However, this equation does not satisfy the cluster property. The approach of Phillips, Wallace, and Mandelsweig [20, 87], which we denote by PWM, also puts the particles equally off-shell, but includes all negative energy contributions. Setting $n = 3$ in Eq. (51), the PWM propagator for equal mass particles in the c.m. system is

$$
G_{\text{PWM}}(p, P) = \int dp_0 \, \mathcal{G}_{\text{PWM}}(p, P) = \int dp_0 \left\{ S_1(p_1) S_2(p_2) + G_C(p, P) \right\}
$$

$$
\rightarrow \left\{ \frac{\Lambda_1^+(\hat{p}_+) \Lambda_2^+(\hat{p}_-)}{(2E_p - W)} + \frac{\Lambda_1^-(\hat{p}_+) \Lambda_2^-(\hat{p}_-)}{(2E_p + W)} + \frac{\Lambda_1^+(\hat{p}_+) \Lambda_2^-(\hat{p}_-)}{2E_p} + \frac{\Lambda_1^-(\hat{p}_+) \Lambda_2^+(\hat{p}_-)}{2E_p} \right\} \quad (61)
$$

with $4\times4 = 16$ spin degrees of freedom. This propagator differs from BSLT primarily by the presence of the additional G_C term [which contributes the last two terms in the curly brackets involving the "mixed" $\Lambda^+\Lambda^-$ projection operators] that includes contributions from crossed graphs approximately, and correctly builds in the one body limit. The retarded kernel to be used with this propagator, in ladder approximation, is

$$
\mathcal{V}_{\text{PWM}}(p, P) = G_{\text{PWM}}^{-1}(p, P) \left\{ \int dp_0 \mathcal{G}_{\text{PWM}}(p, P) \mathcal{V}_{BS}(p, P) \mathcal{G}_{\text{PWM}}(p, P) \right\} G_{\text{PWM}}^{-1}(p, P) \quad (62)
$$

Perhaps the principle obstacle to implementing this method is that construction of current operators is problematic, and manifest Poincaré invariance is lost (but Wallace [88] has recently shown how to compute boosts for scalar particles exactly). Calculations using this method will be described in next section.

3.6.4. Examples of propagator dynamics

We now turn to a description of two examples of propagator dynamics.

Van Orden, Devine, and Gross [VOG]. The Spectator equation has been used to successfully describe NN scattering and the deuteron bound state [21], and this work uses these results to describe the deuteron form factors [89]. The relativistic kernel used to describe the NN system consists of the exchange of 6 mesons [π, η, σ, δ (or a_0), ρ and ω]. The model includes a form factor for the off-shell nucleon [21], giving a "dressed" single nucleon propagator of the form

$$
S_d(p) = \frac{h^2(p)}{m - \not{p}} \qquad h(p) = \frac{(\Lambda_N^2 - p^2)^2}{(\Lambda_N^2 - p^2)^2 + (m^2 - p^2)^2} \, , \tag{63}
$$

where Λ_N is one of the parameters of the model. Coupling constants and form factor masses (13 parameters in all) are determined by a fit to the data and the deuteron wave functions are extracted [21]. To insure current conservation, the one-nucleon current must satisfy the Ward-Takahashi identity

$$(p' - p)^\mu j_\mu(p', p) = h(p') \left\{ S_d^{-1}(p) - S_d^{-1}(p') \right\} h(p), \tag{64}$$

and this requires an off-shell modification of the single nucleon current. The solution used by VOG is

$$j_\mu(p', p) = f_0(p', p) \left(F_1(Q^2) \gamma^\mu + \frac{F_2(Q^2)}{2m} i\sigma^{\mu\nu} q_\nu \right) + g_0(p', p) F_3(Q^2) \frac{m - \not{p}'}{2m} \gamma^\mu \frac{m - \not{p}}{2m} \tag{65}$$

where $F_3(0) = 1$ but is otherwise undefined [in the applications described below, $F_3 = F_D$ where F_D is the dipole form factor of Eq. (37)], and

$$f_0(p', p) = \frac{h(p^2)}{h(p'^2)} \left[\frac{m^2 - p'^2}{p^2 - p'^2} \right] + \frac{h(p'^2)}{h(p^2)} \left[\frac{m^2 - p^2}{p'^2 - p^2} \right]$$

$$g_0(p', p) = \left(\frac{h(p^2)}{h(p'^2)} - \frac{h(p'^2)}{h(p^2)} \right) \frac{4m^2}{p'^2 - p^2}. \tag{66}$$

While the on-shell form of the current (65) is fixed by the nucleon form factors, and the functions f_0 and g_0 are fixed by the WT identity (64), other aspects of the off-shell extrapolation of the current (65) are *not unique*. Using this one-nucleon current, and recalling that there are no currents of the type shown in Figs. 10(a) or (b) [we postpone discussion of the $\rho\pi\gamma$ current], it was shown [83] that the full two body current to use with the Spectator equation is given by the diagrams shown in Fig. 15. These diagrams are manifestly covariant, and *automatically include effects from Z-graphs or retardation* illustrated in Figs. 10(c) or (d). They are referred to as the complete impulse approximation (CIA) to distinguish them from the relativistic impulse approximation (RIA), an approximate current used in earlier calculations [26]. The RIA is obtained by multiplying diagram 15(a) by two, and is very close to the CIA.

Phillips, Wallace, Divine, and Mandelsweig [PWM]. This work is based on the Mandelsweig and Wallace equation [87], supplemented by contributions from the crossed graphs [20], as described above. It is sometimes referred to as the equal-time approach. A feature of this equation is that it includes the full strength of the Z-graphs; the $\Lambda^+\Lambda^-$ contributions shown in Eq. (61) are roughly twice as strong as the Z-graph contributions included in the Spectator equation. The PWM propagator is also explicitly symmetric, a convenience when applied to identical particles. In the published work reviewed here [20], the deuteron is described by a one boson exchange force using the parameters of the Bonn-B potential with the exception of the σ meson coupling, which is adjusted to give the correct deuteron binding energy. Lorentz invariance is broken by the approximation; the boosts of the deuteron wave functions from their rest frames are treated approximately. The PWM current is a modification of Eq. (55). In the present work retardation effects [like those illustrated in Fig. 10(d)] are omitted from the current operator; only one body terms and Z-graph contributions are included.
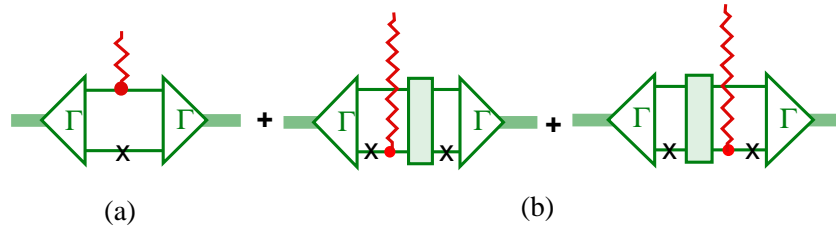
Figure 15. The complete impulse approxiation (CIA) to a ladder Spectator theory. The $\times$ denotes the on-shell particle. In diagrams (b) the kernel connects the region where one of the two particles is on-shell to the region were *both* particles are off-shell. For identical particles, it can be shown that (b) $\simeq$ (a), so that the sum of these three diagrams is approximately equal to $2\times$(a), which is referred to as the relativistic impulse approximation (RIA).

We now turn to a discussion of the other major approach detailed in Fig. 11: hamiltonian dynamics.

3.6.5. Overview of hamiltonian dynamics Approaches based on hamiltonian dynamics start from a very different point than propagator dynamics, and this is one reason it is difficult to compare the two. While propagator dynamics starts from field theory (which can be described as a quantum mechanics with an arbitrary number of particles), hamiltonian dynamics starts from quantum mechanics with a fixed number of particles. For a detailed review, see Ref. [82].

Quantum mechanics begins with a Hilbert space of states defined on a fixed space-like surface in four-dimensional space-time. The various options for choosing this space-like surface were classified by Dirac in 1949 [90]. The *instant-form* corresponds to choosing to construct states at a fixed time $t_0 = 0$, and is the choice usually made in elementary treatments. Alternatively, *front-form* quantum mechanics constructs states on a fixed-light front, customarily defined to be $t^+ = t + z = 0$. (We use units in which the speed of light, c, is unity.) More generally, the light-front may be chosen in any direction defined by $x^\mu n_\mu = 0$, with $n_\mu = \{1, \mathbf{n}\}$ and $\mathbf{n}^2 = 1$. Finally, *point-form* quantum mechanics constructs states on a forward hyperboloid, with $t^2 - \mathbf{r}^2 = a^2$; $t > 0$ [the limiting cases of $a = \infty$ gives the instant-form (with $t_0 = a$), and $a = 0$ the front-form]. These three surfaces are shown pictorially in Fig. 16. [While the point $t = 0$, $\mathbf{r} = 0$ is not on the hyperbolid, all distances between points on the hyperbolid are space-like.]

The Poincaré transformations are symmetries that leave all probabilities unchanged; they must be unitary transformations (with hermitian generators) on the space of quantum states. The 10 generators of the full Poincaré group are the hamiltonian, H, generator of time translations, three-momenta, P^i, generators of spatial translations, angular momenta, J^i, generators of rotations, and K^i, generators of boosts. They satisfy
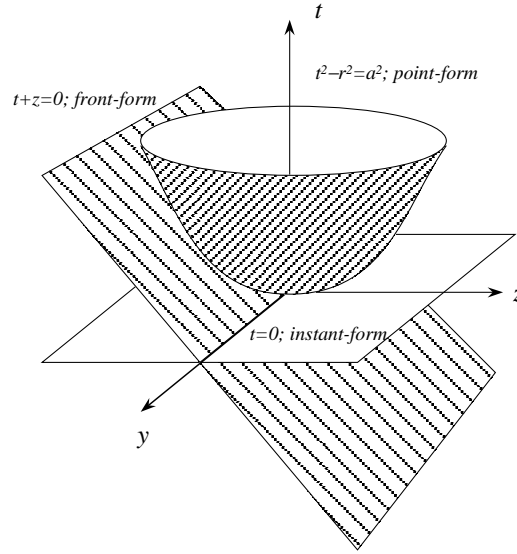
Figure 16. Drawing of the three surfaces on which states can be defined in quantum mechanics. All points on the forward hyperbolid are separated by a space-like interval.

the following commutation relations:

$$[H, P^i] = [H, J^i] = [P^i, P^j] = 0\,, \qquad [J^i, X^j] = i\epsilon_{ijk}X^k\,, \text{for } X^i = J^i, P^i, K^i$$

$$[K^i, K^j] = -i\epsilon_{ijk}J^k\,, \qquad [K^i, P^j] = -i\delta_{ij}H\,, \qquad [K^i, H] = -iP^i \tag{67}$$

For each of the forms of quantum mechanics there is a subgroup of the Poincaré transformations that leave the states invariant on the fixed surface associated with that form. This is the kinematic subgroup, and the transformations in this subgroup will not depend on the dynamics (since the dynamics describe how the states change away for the fixed surface). In the *instant-form*, space translations and rotations clearly leave the surface $t = 0$ invariant. Generators of these transformations form a subgroup of the Poincaré group, with commutation relations

$$[P^i, P^j] = 0\,, \quad [J^i, J^j] = i\epsilon_{ijk}J^k\,, \quad [J^i, P^j] = i\epsilon_{ijk}P^k\,. \tag{68}$$

Transformations of states under these transformations will not depend on the dynamics. The hamiltonian H carries the states away from the initial fixed $t = 0$ surface, and contains the dynamics. The other three generators (the boosts) will also, in general, depend on the dynamics because their commutators involve H.

The *front-form* surface $t^+ = 0$ is left invariant by translations in the x, y, and t^- directions [the generator of translations in the t^- direction is H^+ because $Ht - P_z z = (H^+ t^- + H^- t^+)/2$]. It is also left invariant by rotations and boosts in the z direction, and by the generalized boosts $E^x = K^x + J^y$ and $E^y = K^y - J^x$. These 7 generators form a subgroup of the Poincaré group, with commutation relations

$$[P^i, P^j] = [P^i, H^+] = [J^z, H^+] = [E^i, E^j] = [E^i, H^+] = [J^z, K^z] = [K^z, P^i] = 0$$

$$[J^z, P^i] = i\epsilon_{ij}P^j\,, \quad [J^z, E^i] = i\epsilon_{ij}E^j\,, \quad [E^i, P^j] = -i\delta_{ij}H^+$$

$$[K^z, H^+] = -iH^+ , \quad [K^z, E^i] = -iE^i , \tag{69}$$

where i and $j = \{x, y\} = \{1, 2\}$, and $\epsilon_{12} = 1$, $\epsilon_{21} = -1$, and $\epsilon_{11} = \epsilon_{22} = 0$. The fact that the front-form kinematic subgroup includes *seven* generators, including the boost K^z and generalized boosts E^i, makes the front-form popular. But a principle motivation for using the front-form is that it is a natural choice at very high momentum, where the interactions single out a preferred direction (the beam direction) and the dynamics evolves along the light-front in that direction. The disadvantage is that the generators that contain dynamical quantities are H^- and J^i, and this means that angular momentum conservation must be treated as a dynamical constraint.

Finally, the *point-form* hyperbolid is left invariant by the homogeneous Lorentz group itself, with commutation relations

$$[J^i, J^j] = i\epsilon_{ijk}J^k , \quad [J^i, K^j] = i\epsilon_{ijk}K^k , \quad [K^i, K^j] = -i\epsilon_{ijk}J^k . \tag{70}$$

The hamiltonian and the momentum operators P^i all carry the dynamical information.

We see that each of the forms of quantum mechanics has a different set of kinematic generators, and in no case are they all kinematic. Practitioners of hamiltonian dynamics sometimes speak as if it were impossible to treat the full Poincaré group kinematically. This is true only in the context of hamiltonian dynamics; *all* of the generators are kinematic in the BS or Spectator forms of progagator dynamics.

Dynamics is introduced whenever the states are propagated away from the surface on which they are initially defined. As in normal quantum mechanics, the deuteron will be an eigenstate that propagates in "time" without loss of probability; it will be an eigenstate of the generalized hamiltonian. In the instant-form, the rest state $\Psi_I(0)$ is an eigenstate of the momentum operators

$$\mathbf{P}\Psi_I(0) = \mathbf{0} , \tag{71}$$

and the bound state equation in the rest frame is

$$H\Psi_I(0) = m_d\Psi_I(0) . \tag{72}$$

In the front-form the rest state $\Psi_F(0)$ is an eigenstate of the operators $\mathbf{P}_\perp = \{P^x, P^y\}$ and H^+

$$\mathbf{P}_\perp\Psi_F(0) = \mathbf{0} , \qquad H^+\Psi_F(0) = m_d\Psi_F(0) , \tag{73}$$

and the dynamical bound state equation is

$$H^-\Psi_F(0) = m_d\Psi_F(0) . \tag{74}$$

Finally, in point-form the rest frame eigenfunction must satisfy the four dynamical equations

$$P^\mu\Psi_P(0) = P_o^\mu\Psi_P(0) , \tag{75}$$

Where $P^\mu = \{H, P^i\}$ and $P_o^\mu = \{m_d, \mathbf{0}\}$. In applications, the dynamical equations (72), (74) and the $\mu = 0$ component of (75) can all be taken to be the nonrelativistic Schrödinger equation in the rest frame, so the same nonrelativistic phenomenology can be used for any of these forms of mechanics.

To complete the calculation of the deuteron form factors using hamiltonian dynamics one must choose a current operator that conserves current, and construct the proper matrix elements of this operator between deuteron wave functions. This will be discussed next.

3.6.6. Examples of hamiltonian dynamics The steps taken to construct the current and calculate the form factors depend on the form of quantum mechanics used, and the taste of the investigator involved. Here we briefly describe recent work by five groups.

Forest, Schiavilla, and Riska [FSR]: Based on the work of Schiavilla and Riska [91], Forest and Schiavilla [92] have done an instant-form calculation of the deuteron form factors. The original work of Ref. [91] used on-shell matrix elements of the one body charge and current operators

$$j_N^\mu(p', p) = \left(\frac{m^2}{E(p')E(p)} \right)^{1/2} \bar{u}(p', s') \left[F_1(Q^2)\gamma^\mu + \frac{F_2(Q^2)}{2m} i\sigma^{\mu\nu}q_\nu \right] u(p, s) \tag{76}$$

expanded in powers of v/c. Here F_1 and F_2 are the Dirac and Pauli form factors, usually replaced by the familiar charge and magnetic form factors

$$G_E(Q^2) = F_1(Q^2) - \frac{Q^2}{4m^2} F_2(Q^2)$$
$$G_M(Q^2) = F_1(Q^2) + F_2(Q^2) \,. \tag{77}$$

In the recent unpublished work of Ref. [92] the calculations have been done in momentum space, where the one body current operators have been evaluated without making any (v/c) expansions, the relativistic kinetic energy $\sqrt{m^2 + \mathbf{p}^2}$ has been used in place of the usual nonrelativistic expansion $m + \mathbf{p}^2/(2m)$ [with the parameters of the AV18 potential refitted], and the boost corrections to the deuteron wave functions have been included. This work also includes two-body charge operators from π and ρ exchange using methods developed by Riska and collaborators [93].

Arenhövel, Ritz, and Wilbois [ARW]: This recent calculation [94] does a systematic v/c expansion of relativistic effects that arise from the one body current operator and from contributions from meson exchanges. The current operator (76) is approximated by

$$j_N^\mu(p', p) \simeq \begin{cases} F_1 \left(1 - \dfrac{\mathbf{q}^2}{8m^2} \right) - F_2 \dfrac{\mathbf{q}^2}{4m^2} + (2G_M - F_1) \left[\dfrac{i\sigma \cdot (\mathbf{q} \times \mathbf{p})}{4m^2} \right] & \mu = 0 \\ F_1 \dfrac{(\mathbf{p}' + \mathbf{p})^i}{2m} + G_M \dfrac{i \left[\sigma \times \mathbf{q} \right]^i}{2m} + \mathcal{O}\left[(v/c)^3 \right] & \mu = i \end{cases} \tag{78}$$

where $j_N^\mu = j_p^\mu$ or j_n^μ (with appropriate F_1 and F_2), σ is the operator in the nuclear spin space, and $\mathbf{q} = \mathbf{p}' - \mathbf{p}$ is the *three*-momentum transferred by the electron. This charge operator is correct to order $(v/c)^2$, and the $(v/c)^3$ contribution to the current operator is given in Ref. [95]. The $\mathbf{q}^2/8m^2$ correction term to the charge operator is referred to as the Darwin-Foldy term. The $\sigma \cdot (\mathbf{q} \times \mathbf{p})$ is the spin-orbit term.

There are ambiguities in all calculations based on expansions in powers of $(v/c)^2$. One ambiguity arises from the fact that the square of the three-momentum, $\mathbf{q}^2$, depends

on the frame in which it is evaluated. In the Breit frame, $\mathbf{q}^2 = Q^2$, while in the center of mass of the final deuteron (the frame preferred by ARW), $\mathbf{q}^2 = (1 + \eta)Q^2$ (recall that η was defined in Sec. 3.1). A second ambiguity surrounds the choice of G_E versus F_1. Some experts [91] advocate using G_E (because it is the correct charge operator) in place of F_1. The difference between F_1 and G_E is of higher order. These ambiguities introduce theoretical uncertainty into any calculation. The size of this uncertainty depends on both the value of Q^2 and the choice of nucleon form factors; for example the difference between using F_1 or G_E can be inferred from the ratios shown in Fig. 4 and is large for the recently measured JLab form factors and small for the MMD form factors. Uncertainties of this kind do not arise if the calculation is done covariantly, or to all orders in $(v/c)^2$.

ARW also include boost corrections originally derived to lowest order in v/c by Krajcik and Foldy [96]. The boost corrections can be written as an operation on the wave function of the form

$$B\Psi_0(r) = e^{-i\chi}\,\Psi_0(r) \simeq (1 - i\chi)\,\Psi_0(r)\,, \tag{79}$$

where $\chi = \chi_0 + \chi_V$ with

$$\chi_0 = -\left(\frac{(\mathbf{r}\cdot\mathbf{P})(\mathbf{p}\cdot\mathbf{P})}{16m^2} + \text{h.c.}\right) + \frac{[(\sigma_1 - \sigma_2)\times\mathbf{p}]\cdot\mathbf{P}}{8m^2} \tag{80}$$

the boost associated with the kinetic energy and the spin and χ_V the boost associated with the potential. In (80), $\mathbf{r}$ and $\mathbf{p}$ are the relative coordinate and relative momentum of the nucleon pair, and $\mathbf{P}$ is the three-momentum of the moving deuteron. ARW use the values of χ_V worked out by Friar [97], and also include relativistic effects from retardation, isobar currents, and meson exchange. To evaluate the latter a meson exchange model is needed, and ARW use the interactions and parameters of the Bonn OBEPQ potentials [only results from the OBEPQ B potential are presented in the next section, although Ref. [94] includes results from all three OBEPQ potentials]. Friar has emphasized that relativistic effects can be moved in and out of the wave functions and currents by unitary transformations [97, 98], so that all of these effects are ambiguous unless fully defined by the theory. Effects due to pair currents or recoil corrections, shown in Fig. 10(c) and (d), do not appear to be included. ARW state that their calculations should be good only up to $Q^2 \simeq 1.2$ GeV^2.

Corrections to the charge operator to order $(v/c)^2$ obtained from instant-form dynamics and from the Spectator form of propagator dynamics have been compared [76, 97, 98, 99]. In the cases studied, the same total result was obtained from the sum of *all* of the corrections, but the individual terms in the sum were found to have a very different form even when they appeared to come from the same physical effects.

Carbonell and Karmanov [CK]: In this front-form calculation [100] the direction of the light-front [denoted by $\omega^\mu = \{1, \mathbf{n}\}$ where $\mathbf{n}^2 = 1$] is treated as an unphysical degree of freedom. Wave functions and amplitudes may depend on ω but only those components of scattering matrix elements independent of ω will be physical. It is argued that this approach will give an explicitly covariant front-form mechanics [101]. When

applied to the deuteron form factors there are 11 spin invariants, three that are physical and 8 that depend on ω and are unphysical. In an exact calculation the 8 unphysical invariants would be zero, but in approximate calculations, such as that carried out in Ref. [100], they will not be zero. The deuteron form factors can be extracted from the three physical invariants by projecting them from the general result, as derived in Ref. [101]. For the choice $\omega^\mu = \{1, 0, 0, -1\}$ (corresponding to choosing the front-form surface $t^+ = 0$) this method shows that the charge and quadrupole form factors can be extracted from the J^+ component of the current (in common with other treatments), but also shows that the magnetic form factor *cannot be obtained only from this component* and requires a different projection (and includes contributions from contact terms). The rules for a general graph technique for calculating amplitudes in this formalism are given in Ref. [102].

Using this method the deuteron wave function will in general have 6 components, only three of which have been found to be numerically large. In addition to the familiar S and D-state components, the third large component is proportional to a new scalar function f_5, and adds the term

$$\Psi^5_{abm}(\mathbf{p}) = -\sqrt{\frac{3}{4\pi}} \frac{i}{2} f_5 \left(\sigma_1 - \sigma_2\right) \cdot \left(\hat{\mathbf{p}} \times \mathbf{n}\right) \chi^{1m}_{12} \tag{81}$$

to the deuteron wave function displayed in Eq. (6) (to obtain this form we renormalized the expression in Ref. [100] so that $f_1 = u$ and used the transformations in Ref. [10]). In Ref. [100] f_5 is calculated perturbatively using the Bonn potential from Ref. [103] without change of parameters. They find that f_5 is the largest of the three components for all momenta greater than 500 MeV, and believe that the perturbative estimate is accurate to about 20%. The physical meaning of the f_5 contribution has been studied in threshold deuteron electrodisintegration, where it contributes about 50% of important pair term contributions.

Lev, Pace, and Salmé [LPS]: The LPS [104] calculation is a recent version of a series of light-front calculations that have assumed the light-front is fixed (at $t^+ = t + z = 0$). In the past, calculations with fixed light fronts have run into a problem with the loss of angular momentum conservation, and before we review the LPS results we will discuss this issue.

In calculating form factors with fixed light fronts it has been conventional to choose a coordinate system where $q^\pm = q^0 \pm q^z = 0$ and $q_\perp = \mathbf{Q}$. Current conservation is then satisfied if only one component of the current (J^+) is non zero. Consider the matrix elements of the deuteron current, $J^+_{\lambda'\lambda}$, where λ' (λ) are the helicities of the outgoing (incoming) deuterons. One consequence of the loss of *manifest* rotational invariance is that there are *four* independent matrix elements of the J^+ current related by the constraint

$$J^+_{00} + 2\sqrt{2\eta} J^+_{+0} - J^+_{+-} - (1 + 2\eta) J^+_{++} = 0 \ . \tag{82}$$

This is a dynamical constraint often referred to as the "angular condition" [105, 106]. The deuteron form factors can be extracted from *any* choice of three of the matrix

elements $J^+_{\lambda'\lambda}$, and if condition (82) is not satisfied each choice will yield different results. The form factors will not be uniquely determined unless the angular condition is satisfied.

To avoid (or solve) this problem, LPS work in the Breit frame, where $q^\pm = \pm Q$ and $q_\perp = 0$. Current conservation then requires that $J^+ = J^-$. A current operator that satisfies these conditions was constructed in Ref. [107]. For elastic scattering this operator has the form

$$J^\alpha = \frac{1}{2}\left\{ J^{\alpha'}_{free} + L^\mu_\nu\, e^{i\pi S_x} \left(J^{\alpha'}_{free} \right)^* e^{-i\pi S_x} \right\} \qquad \begin{cases} \alpha = \alpha' & \text{for } \alpha = +, \perp \\ \alpha' = + & \text{for } \alpha = - \end{cases} \tag{83}$$

where J_{free} is the free (one body) current operator, and L^μ_ν and $e^{i\pi S_x}$ are rotations by $-\pi$ about the x axis, L^μ_ν in the vector space and $e^{i\pi S_x}$ in the spinor space. Note that the definition insures that $J^+ = J^-$ as required by current conservation. Using this current, LPS have calculated the deuteron quadrupole moment, Q_d, to 2% accuracy [108]. The calculation shown below in Sec. 3.8 uses MMD nucleon form factors and the Nijmegen II deuteron wave functions.

Allen, Klink, and Polyzou [AKP]: The deuteron form factors have also been recently calculated using the point-form of quantum mechanics [109]. Here there is no difficulty in writing down manifestly covariant matrix elements, but there is some ambiguity in deciding how to impose current conservation. AKP work in the Breit frame, choose a one body impulse current to describe the $\mu = 0, 1$, and 2 components of the current, and introduce a two body current J^z_2 (which need not be calculated) to insure current conservation. New effects come from the way the wave functions are constructed in point form ("velocity" states are constructed), and from the fact that momentum is now a dynamical generator, so that the momentum transferred to the nucleon *inside* the deuteron is not equal to the momentum transferred to the deuteron as a whole. They argue that the momentum transferred to each nucleon inside the deuteron is

$$Q^2_n = (p'_1 - p_1)^2 = Q^2 \frac{4(m^2 + \mathbf{p}^2_\perp)}{m^2_d}(1 + \eta) > Q^2(1 + \eta). \tag{84}$$

At momentum transfers $Q^2 \simeq 4$ GeV^2 this is a 25% increase, and leads to a large suppression of the form factors. This explains part of the decrease in the size of the form factors predicted by this model. The results reported below use the MMD nucleon form factors and the AV18 NN potentials.

We now turn to a brief review of methods using quark degrees of freedom.

3.7. Calculations using quark degrees of freedom

Calculations based on quark degrees of freedom must confront the fact that the deuteron is at least a six quark system. Since the six quarks are identical (because of internal symmetries) the system must be antisymmetrized, and it is not clear that the nucleon should retain its identity when in the presence of another nucleon. How does the clustering of the six quarks into the two three-quark nucleons appear at large distance scales? How do we treat the confining forces in the presence of so many quarks?
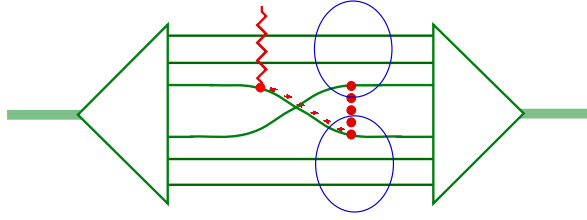
Figure 17. Diagram showing a photon coupling to a quark exchange diagram. The exchanged gluon (or meson), shown by the heavy dotted line, distributes the momentum equally between the two three-quark clusters, suggesting the result (86).

The approach to these issues depends on whether of not Q^2 is large enough to justify the use of perturbative QCD (pQCD).

3.7.1. Nonperturbative methods At modest Q^2 the momentum transferred by the gluons is small and the QCD coupling is too large for perturbative methods to be useful. In the nonperturbative regime calculations must be based on models. Many papers have been written addressing these issues, and a complete review is beyond the scope of our discussion. Here we mention only two contributions that give the flavor of the discussion. Maltman and Isgur [110, 111] studied the ground state of six quarks interacting through a qq potential previously used to explain the spectrum of excited nucleons, and found that there was a natural tendency for the quarks to cluster into two groups of three (i.e. nucleons). They obtained a reasonable description of the deuteron, and confirmed that the short range NN repulsion could be largely understood in terms of quark exchange. Later, de Forest and Mulders [112], using a very simple model, considered the effect of antisymmetrization on the structure of the form factor. Their calculations suggest that the zeros seen in form factors could be a consequence of antisymmetration alone. They also show that the factorized form of the impulse approximation obtained from nonrelativistic (and some relativistic) theories, which gives the deuteron form factors as a product of a nucleon form factor and a nuclear (or body) form factor

$$G_D(Q^2) = F_N(Q^2) \times D_1(Q^2) \,, \tag{85}$$

may not be a good description in the presence of antisymmetration. When quarks are exchanged between nucleons it is no longer possible to separate the *nucleon* structure from the *nuclear* structure. Consideration of the quark exchange diagram shown in Fig. 17 suggests a factorization formula of the form

$$G_D(Q^2) = \left[F_N([Q/2]^2)\right]^2 \times D_2(Q^2) \,. \tag{86}$$

Because nucleons are composite and identical, either of the forms (85) or (86) (or yet other relation) might hold, and there is no clearly correct way to isolate the structure of the nucleon from the structure of the bound state.

In model calculations these issues can be handled by separating the problem into two regions: at large separations $(R > R_c)$ it is assumed that the system separates into two nucleons interacting through one pion exchange, and at small distances $(R < R_c)$ the system is assumed to coalesce into a six-quark bag with all the quarks treated on an equal footing. In this review we report the results of a calculation by Dijk and Bakker [113], where references to other calculations of this type can also be found (see also the work of Buchmann, Yamauchi, and Faessler [114]).

Dijk and Bakker [DB]: This calculation is based on the quark compound bag model introduced by Simonov [115]. Here the six-quark wave function is assumed to be the sum of a hadronic part and a quark part. The hadronic part is a fully antisymmetrized product of two three-quark wave functions, each with the quantum numbers of a nucleon, and a relative NN wave function $\chi_{NN}(\mathbf{r})$

$$|\psi_h\rangle = \mathcal{A}\left[\psi_N(123)\psi_N(456)\,\chi_{NN}(\mathbf{r})\right], \tag{87}$$

where $\mathbf{r} = (\mathbf{r}_1 + \mathbf{r}_2 + \mathbf{r}_3 - \mathbf{r}_4 - \mathbf{r}_5 - \mathbf{r}_6)/3$ is the effective internucleon separation. The quark part is a sum of eigenstates $|\psi_\nu\rangle$ of a confined 6-quark system

$$|\psi_q\rangle = \sum_\nu a_\nu |\psi_\nu\rangle, \tag{88}$$

where the confined 6-quark states are zero outside of a confining radius $r = b$, which is a parameter of the calculation. In the applications, only one term $\nu = 1$ needs to be included in the sum (88). The dynamical quantities determined by the calculation are the NN wave function $\chi_{NN}(\mathbf{r})$ and the spectroscopic coefficient $a_1(E)$ which is a function of the energy E.

The NN scattering phase shifts and mixing parameters are determined by replacing the spectroscopic coefficients by boundary conditions on the surface $r = b$ and integrating the Schrödinger equation for $r > b$. The Paris potential [12] is used to describe the NN interaction in the peripheral region and is set to zero in the inner region. Two models were developed; in this review we report results from the fits to the Arndt single energy 1986 [116] solutions, which DB denote QBC86. This fit finds $b = 1$ fm. Calculation of the form factors requires an assumption about the form factor of the internal compound bag part of the wave function. They use

$$F_{c1}(Q^2) = \left(1 + 2Q^2/5\Lambda_1^2\right)^{-5} \tag{89}$$

with $\Lambda_1 = 1$ GeV obtained from a fit to the A and B structure functions. Results from this model are reported in Sec. 3.8 below.

3.7.2. Perturbative QCD If one believes the momentum transfer is high enough, perturbative QCD (pQCD) may be used to study the deuteron form factor and reactions. Here it is assumed that the problem naturally factors into a hard scattering process in which the momentum transfer is distributed more or less equally to all of the six quarks, *preceeded and followed* by soft, nonperturbative scattering that sets the scale of the interaction but does not strongly influence its Q^2 behavior. The Q^2 behavior
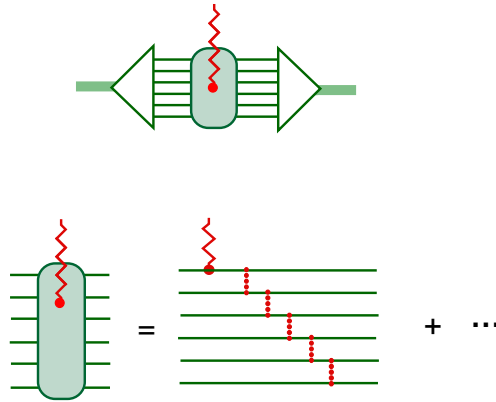
Figure 18. Feynman diagrams that give the pQCD result. Upper panel shows the separation of the form factor into the hard scattering part and the initial and final wave functions that contain the soft scattering. Lower panel shows one of the thousands (in this case) of hard scattering diagrams that make up the hard scattering part.

is therefore determined by the hard scattering, which can be calculated perturbatively. The formalism and method are reviewed in the seminal papers by Brodsky and Farrar [117] and Lepage and Brodsky [118].

These calculations of the form factor are all based on the diagrams shown in Fig. 18. In the hard scattering, the momentum transfer Q is distributed to the six quarks through the five hard gluon exchanges, the last of which carries a momentum of approximately $Q/6$. If the spin factors are included with the quark propagators, the only large Q^2 dependence comes from the $1/Q^2$ of each gluon propagator, giving the *counting rule* for the hard scattering part F_h

$$F_h(Q^2) \sim \left[Q^2\right]^{-(n_c-1)} , \tag{90}$$

where n_c is the number of constituent quarks (6 for the deuteron) and $n_c - 1$ the number of gluon propagators. This leads immediately to the prediction that the leading contribution to the deuteron form factor should go like Q^{-10}, or that $A \sim Q^{-20}$. The argument also shows that the perturbative result cannot be expected to set in until $Q/6 > 0.5$ to 1 GeV, somewhere in the region of Q^2 from 9 to 36 GeV^2. (All agree that pQCD must give correct predictions at sufficiently high Q^2, but how large this Q^2 must be is a topic of considerable controversy [119, 120].) Note that this simple argument does not set the scale of the form factor; estimates can be obtained from detailed evaluation of more than 300,000 diagrams that contribute to the hard scattering [121]. It turns out that this leading twist pQCD estimate is $10^3 - 10^4$ times smaller than the measured deuteron form factor, implying large soft contributions to the form factor, in agreement with [119, 120], and suggesting that pQCD should not be used as an explanation for the form factor. The calculation is extremely complicated and a confirmation, or refutation, is desirable.

Perturbative QCD also predicts the *spin dependence* of the hard scattering, and

these predictions provide a more stringent test of the onset of pQCD. These spin dependent predictions have implications for the individual deuteron form factors, and these were first presented in Ref. [122], and further developed in Refs. [123, 124, 125]. Application of these rules to hadronic form factors in general shows that

- Hadrons with an *even* number of quarks will be dominated by the *longitudinal* (charge) currents, while these with an *odd* number of constituents by *transverse* (magnet) currents. Hence, the dominant form factors at large Q^2 should be the nucleon magnetic form factors and the deuteron charge (or quadruple) form factors.

- The dominant form factors at large Q^2 are those that conserve helicity.

When applied to the deuteron, these rules lead to the conclusion that the helicity amplitude G_{00}^0 [c.f. Eq. (20)] dominates at large Q^2; the others are smaller by at least a power of Q. In particular, this implies that $G_{+-}^0 \sim G_C - 2\eta G_Q/3 \to (\Lambda/Q)G_{00}^0$, where Λ is the mass scale above which the nonleading terms can be neglected. Hence

$$\tilde{t}_{20}(Q^2) \to -\sqrt{2}\left\{1 + \mathcal{O}(\Lambda/Q)\right\} . \tag{91}$$

Unfortunately, this argument does not allow one to estimate the ratio B/A, since B is controlled by a different, independent helicity amplitude.

In Ref. [123] an attempt was made to improve on the constraint (91). These authors used the front-form, and evaluated the current in the light-front Breit frame where the plus component of the momentum transfer $q^+ = 0$. In this frame all three deuteron form factors may be written in terms of matrix elements of the $J^+ = J^0 + J^3$ component of the current

$$G_C = \kappa \left\{\left(1 - \tfrac{2}{3}\eta\right) G_{00}^+ + \tfrac{8}{3}\sqrt{2\eta}G_{+0}^+ + \tfrac{2}{3}(2\eta - 1)G_{+-}^+\right\}$$
$$G_M = \kappa \left\{2G_{00}^+ + 2(2\eta - 1)\frac{G_{+0}^+}{\sqrt{2\eta}} - 2G_{+-}^+\right\}$$
$$G_Q = \kappa \left\{-G_{00}^+ + 2\frac{G_{+0}^+}{\sqrt{2\eta}} - \frac{(\eta + 1)}{\eta}G_{+-}^+\right\} , \tag{92}$$

where $\kappa = [2p_+(2\eta + 1)]^{-1}$. Perturbative QCD predicts that G_{00}^+ will dominate at large Q^2, and if this happens at a scale $\Lambda << m_d$ it follows from (92) that the form factors go in the ratio of $G_C : G_M : G_Q = (1 - 2\eta/3) : 2 : -1$. This leads to a prediction for B/A and to a prediction for $\tilde{t}_{20}$ that differs from (91) at moderate Q^2. However, rotational invariance is not manifest in the light front, and there are *four* nonzero components of the J^+ current corresponding to deuteron helicity combinations of 00, ++, +0 and +− that are related by the angular condition discussed in Sec. 3.6.6 above. Carlson has recently shown [126] that the angular condition places strong constraints on the possible subleading behavior of the helicity amplitudes. Perturbative QCD predicts that the subleading amplitudes will go like

$$G_{+0}^+ \to a(\Lambda/Q)G_{00}^+ , \qquad G_{+-}^+ \to b(\Lambda/Q)^2G_{00}^+ , \qquad G_{++}^+ \to c(\Lambda/Q)^2G_{00}^+ , \tag{93}$$

where a, b, and c are dimensionless constants of the order of unity, and Λ is the scale at which pQCD begins working for the deuteron [the Gs in Eq. (93) are identical to the
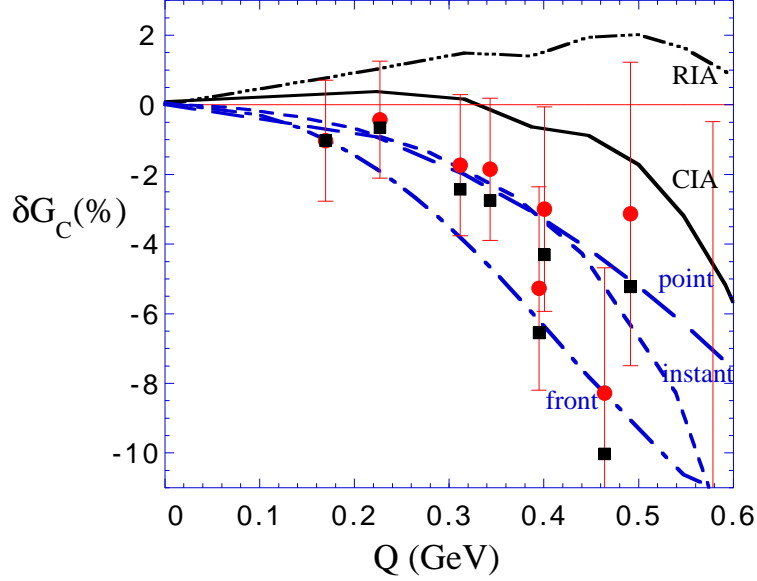
Figure 19. Corrections to the charge form factor, G_C. Each curve shows the difference $G_C(full) - G_C(nr)$ expressed as a percentage of the nonrelativistic result $G_C(nr)$. The individual cases are discussed in the text. The squares without error bars are the extracted G_C data from Ref. [30] and the circles with errors are the Coulomb corrected data as discussed in the text.

*J*s in Eq. (82)]. Assuming that $Q^2 >> \Lambda^2$ (but making no assumption about the size of Λ) the angular condition in leading order becomes:

$$\left\{ 1 + \sqrt{2}a\frac{\Lambda}{m_d} - \frac{c\Lambda^2}{2m_d^2} \right\} G_{00}^+ = 0 \ . \tag{94}$$

Solution of this equation therefore requires that $\Lambda \sim m_d$ and $Q^2 >> m_d^2$. Under these conditions the relations (92) again produce *only* the result (91).

3.8. Comparison of theory with experiment

In this section we compare theory with experiment and draw conclusions from this comparison. Our major conclusions will be restated and summarized again in Sec. 3.10 below.

3.8.1. The charge form factor at very small Q^2   Figure 19 shows how coulomb distortion of the incoming and outgoing *ed* plane waves effects the very low Q^2 data (extracted from Ref. [4]) for the charge form factor, G_C. The figure also compares this data with theory.

Corrections for Coulomb distortion change the deuteron radius from an apparant 2.113 fm (as measured in *ed* scattering) to 2.130 fm (after the correction) [44]. To remove the distortions from the data of Ref. [4], we adjust G_C by [127]

$$\delta G_C \simeq -0.003 + 0.104\, Q^2 \ . \tag{95}$$

Table 5. Features of the eight theoretical models reviewed in Secs. 3.6.4, 3.6.6, and 3.7.1.

| model	dynamics	description	consistent current
VOG [89]	propagator	Spectator	yes
PWM [20]	propagator	modified Mandelsweig-Wallace	no
FSR [92]	hamiltonian	instant-form; no v/c expansion	yes
ARW [94]	hamiltonian	instant-form; with v/c expansion	yes
CK [100]	hamiltonian	front-form; dynamical light-front	no
LPS [104]	hamiltonian	front-form; fixed light-front	no
AKP [109]	hamiltonian	point-form	no
DB [113]	nonrelativistic	quark-cluster	yes

Note that this decreases G_C at very small Q giving a larger deuteron radius, but increases G_C where the data have been extracted. The figure shows both the uncorrected and the Coulomb corrected data normalized to the nonrelativistic AV18 calculation with the MMD nucleon form factor. Note that the difference between the Coulomb corrected and uncorrected data is about half of the experimental error at $Q \simeq 0.5$ GeV.

The figure also shows the size of relativistic and interaction current corrections that arise from the instant-form calculation ARW of Ref. [94], the front-form calculation LPS of Ref. [104], the point form calculation AKP of Ref. [109], and the CIA and RIA approximations from Ref. [89]. These calculations were discussed in Sec. 3.6.4 and 3.6.6 above. At the scale of the current experimental accuracy (a few percent), the relativistic treatments *differ noticeably*. They also differ from the EFT calculation (shown previously in Fig. 9) which drops sharply below the data for $Q > 0.2$ GeV. It is important that these calculations be systematically compared and the different physical content of these approaches be isolated and understood. In particular, it would be very interesting to know why the covariant CIA and RIA have more positive corrections than those obtained from the hamiltonian forms of dynamics.

3.8.2. Overview of the high Q^2 predictions The high Q^2 predictions for the eight models reviewed in Secs. 3.6.4, 3.6.6, and 3.7.1 are shown in Figs. 20–22. The models are summarized in Table 5.

These calculations give very different results. Figure 20 shows the predictions for $A(Q^2)$, with the model dependent $\rho\pi\gamma$ exchange current intentionally omitted from all of the calculations. All of the models except the AKP point-form calculation give a reasonable description of A out to $Q^2 \sim 3$ GeV^2, beyond which they begin to depart strongly from each other and the data. Taking into account that the $\rho\pi\gamma$ exchange current *could be added to any of these models, and that this contribution tends to increase A above $Q^2 \sim 3$ GeV^2* (for the sign of the $\rho\pi\gamma$ coupling constant used in the discussion in the following paragraph), four models seem to have the right general behavior: the VOG, FSR, ARW and the quark model of DB (but there are no results for this model beyond $Q^2 = 4$ GeV^2). Ironically, none of the models favored by the high Q^2 data does
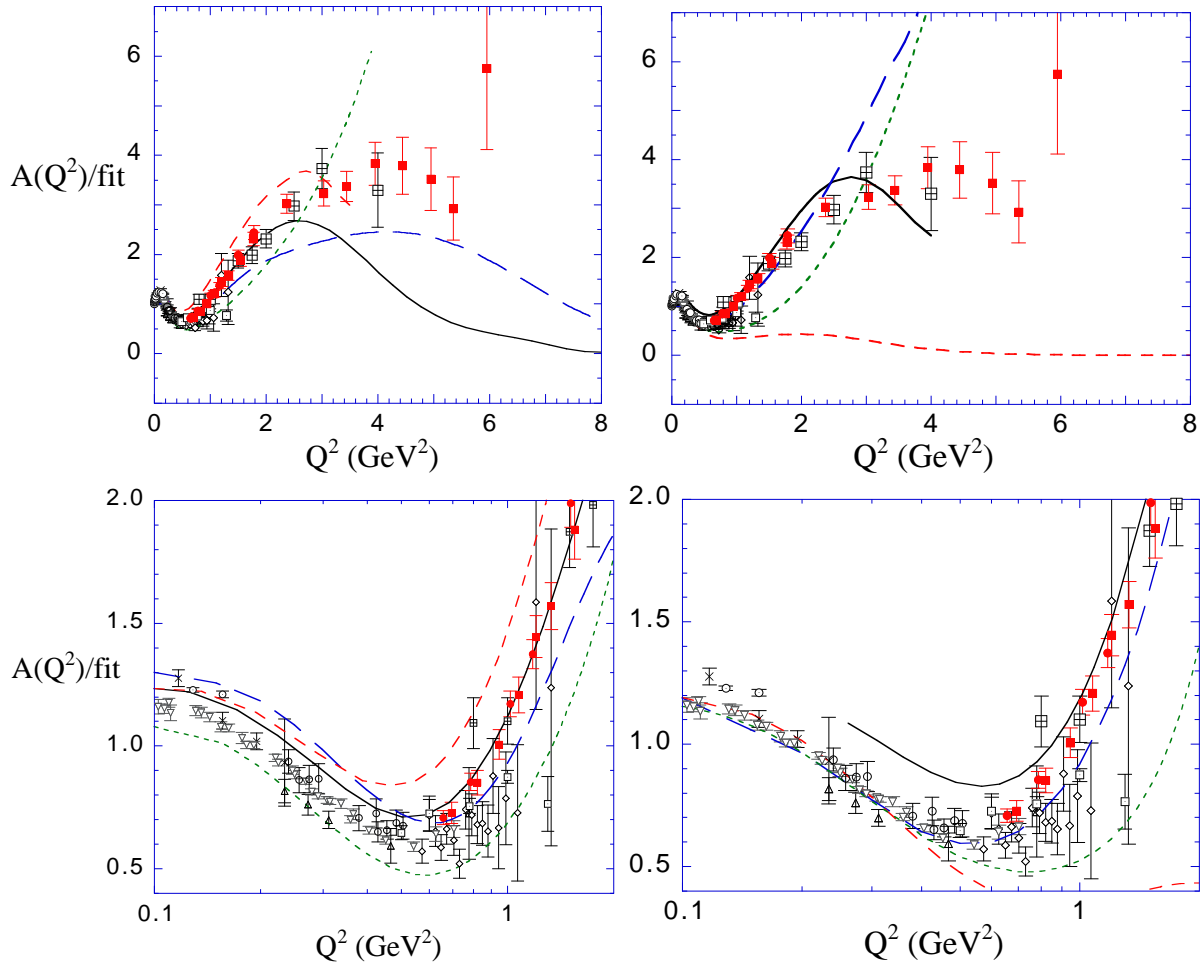
Figure 20. The structure function A for the eight models discussed in the text. Left panels show the propagator and instant-form results: FSR (solid line), VOG in RIA approximation (long dashed line), ARW (medium dashed line), and PWM (short dashed line). Right panels show the front-form CK (long dashed line) and LPS (short dashed line), the point-form AKP (medium dashed line) and the quark model calculation DB (solid line). In every case the calculations have been divided by $\tilde{A}$ calculated from the fit (39). See Table 2 for references to the data.

as well at low Q^2 as the three "unfavored" models shown in the right panels (unless the Platchkov [40] data are systematically too low). Another possibility suggested by effective field theory [74] is that the asymptotic normalization of the relativistic deuteron wave functions is incorrect, and that a small adjustment in NN parameters to insure a good value for this constant would correct the problem.

Figure 21 shows the effect of the new JLab measurements of the nucleon form factors on predictions for $A(Q^2)$. These new form factors will *decrease* predictions for A for momentum transfers in a region around $Q^2 = 4$ GeV^2 (by a factor of 2 for the model
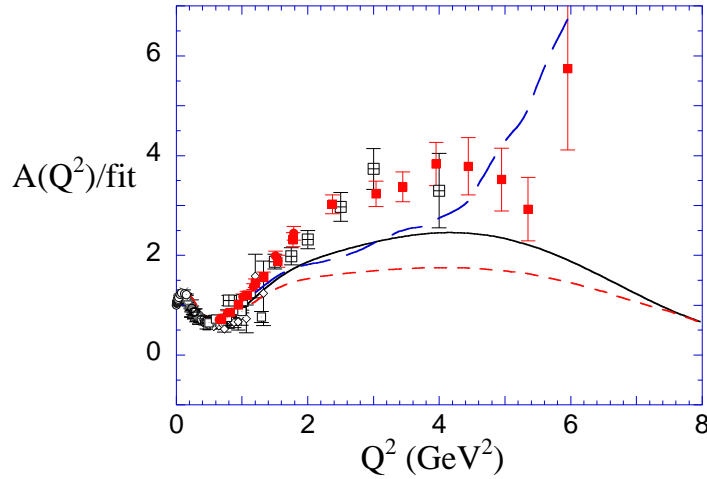
Figure 21. Effects of the new JLab measurements and the $\rho\pi\gamma$ exchange current on predictions for A. The solid line is the VOG model prediction (in RIA approximation) with MMD nucleon form factors (identical to the lon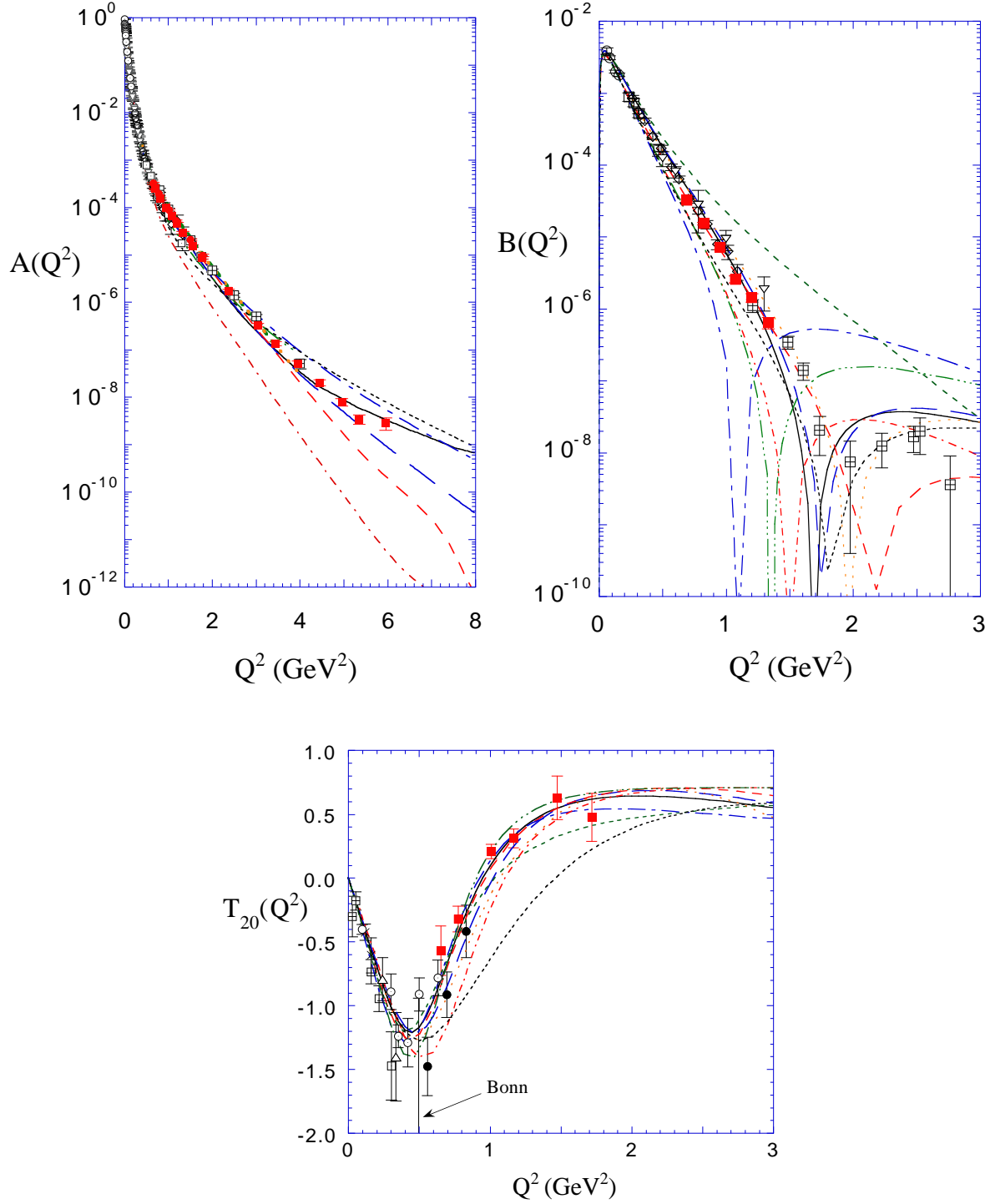g dashed curves shown in Fig. 20). The short dashed line is the VOG prediction (in RIA approximation) with JLab model nucleon form factors, Eq. (38). The long dashed curve is the full VOG calculation (CIA, $\rho\pi\gamma$ exchange current with the form factor of Ref. [129], and MMD form factors).

shown), increasing the descrepancy between predictions and the data. [However, it may improve the prediction for those models (PWM, CK, and LPS) that are currently too large in this region.] The figure also shows how the $\rho\pi\gamma$ exchange current could increase predictions at large Q^2. The difference between the solid and long dashed lines is due largely to the effect of the $\rho\pi\gamma$ exchange current (but is also do in small part to the fact that the CIA result is slightly smaller that the RIA). Unfortunately, the size of the $\rho\pi\gamma$ exchange current is very sensitive to the $\rho\pi\gamma$ form factor, as discussed in Ref. [128], and could even be too small to see at these momentum transfers (if the current estimates of the $\rho\pi\gamma$ form factor are too large). This is our reason for insisting that this contribution should be viewed as new physics — not readily predictable within a meson model.

Finally, Fig. 22 shows the predictions for the structure functions A, B, and T_{20} for the eight models discussed. The LPS calculation shows a large descrepency with the T_{20} data, but the most striking feature of these plots is the *large model dependence* of the predictions for $B(Q^2)$. The magnetic structure function provides the most stringent test, and the predictions are comparatively free of the $\rho\pi\gamma$ exchange current (which gives only a small contribution to B). Examination of the figure shows that the B predictions of the PWM, ARW, AKP, CK models fare the worst. In all, taking the predictions for the three structure functions together, the best results are obtained with the FSR, VOG, and DB models.

Figure 22. The structure functions A, B, and T_{20}. The models, in order of the Q^2 of their mimima in B, are: CK (long dot-dashed line), PWM (dashed double-dotted line), AKP (short dot-dashed line), VOG full calculation (as shown in Fig. 21 – solid line), VOG in RIA (long dashed line), LPS (dotted line), DB (widely spaced dotted line), FSR (medium dashed line), and ARW (short dashed line). See Tables 2, 3, and 4 for references to the data.
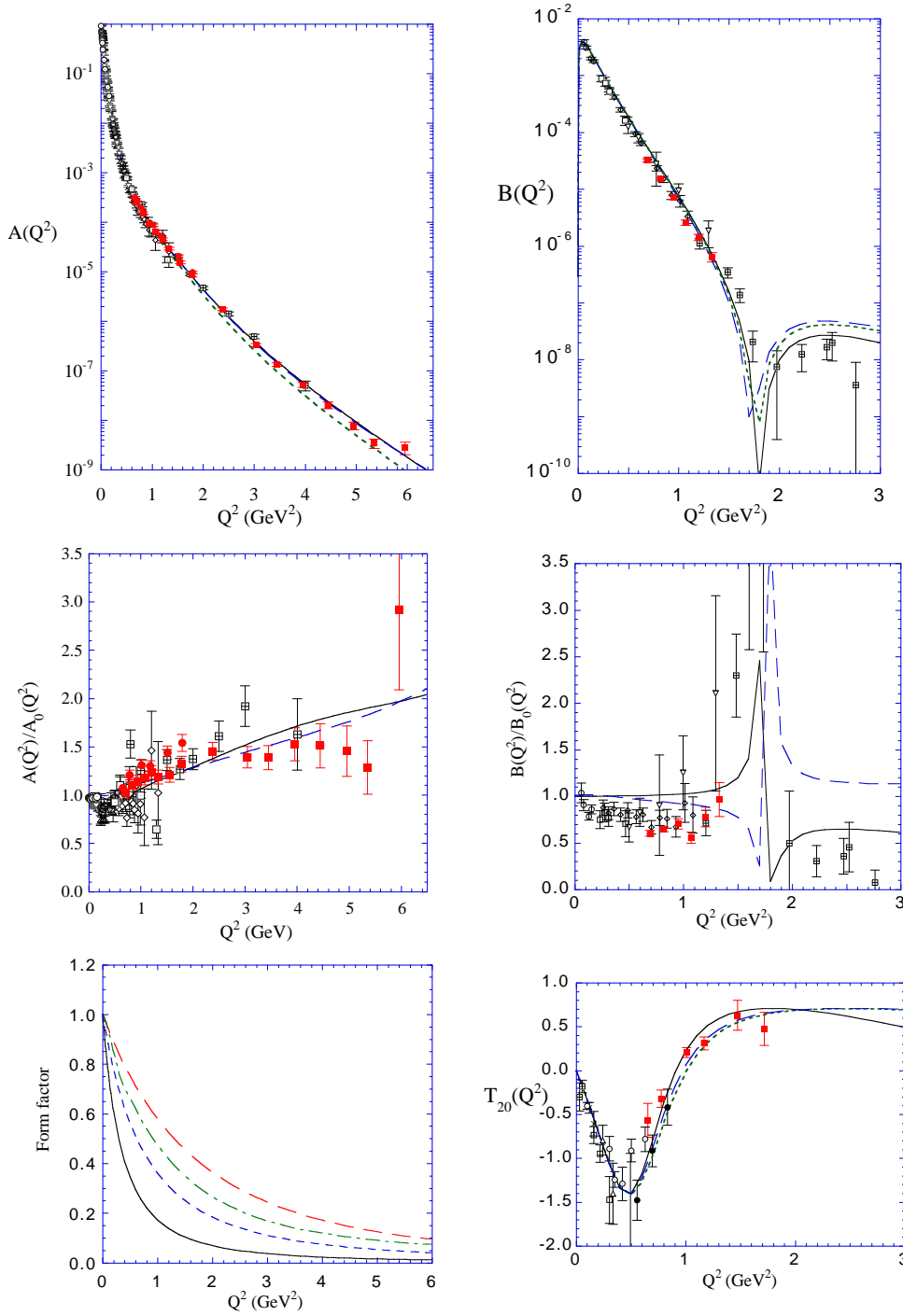
Figure 23. Upper panels (A and B) and lower right panel ($\tilde{T}_{20}$) compare data to three theoretical models based on VOG: (i) "standard" case referred to in the text (dotted line), (ii) model with the tripole F_3 (solid line), and (iii) model with the dipole $f_{\rho\pi\gamma}$ (dashed line). The center two panels show the data and models (ii) and (iii) divided by model (i). The lower left panel shows form factors: standard dipole with $\Lambda^2 = 0.71$ (solid line), dipole with $\Lambda^2 = 1.5$ (short dashed line), Rome $f_{\rho\pi\gamma}$ (dot-dashed line) [129], and the tripole with $\Lambda^2 = 5$ (long dashed line).

3.8.3. Important lessons We conclude our comparison with theory by extending our discussion somewhat beyond the limits of previously published papers. To make the point clearly, focus on the VOG calculation using the Spectator equation, and recall that current conservation *required* that the single nucleon current in this approach, Eq. (65), include a new form factor, $F_3(Q^2)$. This form factor must satisfy the constraint $F_3(0) = 1$, but is otherwise *completely unspecified*. In the published VOG calculation [89] and in all of the plots shown so far, this form factor was taken to be the standard dipole, F_D.

Figure 23 shows how agreement between theory and experiment can be significantly improved by choosing a different form for the unknown form factor F_3. This figure shows three theoretical predictions: (i) the "standard" VOG RIA prediction with $F_3 = F_D$ and *no* $\rho\pi\gamma$ exchange current, (ii) another model with *no* $\rho\pi\gamma$ exchange current, but with a tripole F_3 of the form

$$F_3(Q^2) = \frac{1}{(1 + Q^2/5)^3} \,, \tag{96}$$

and (iii) a model with $F_3 = F_D$ and a dipole $\rho\pi\gamma$ form factor

$$f_{\rho\pi\gamma}(Q^2) = \frac{1}{(1 + Q^2/1.5)^2} \,. \tag{97}$$

In both form factors Q^2 is in GeV^2. These form factors are shown in the bottom left panel of the figure.

Figure 23 shows that a good agreement between theory and experiment can be obtained with the tripole F_3 without any $\rho\pi\gamma$ exchange current, and that to some extent the $\rho\pi\gamma$ exchange current can be substituted for a hard F_3 (although F_3 is better than $f_{\rho\pi\gamma}$ at improving all three observables simultaneously). We see that we have, in some sense, achived the goals of a theory of elastic *ed* scattering based on nucleon degrees of freedom. *With small adjustments of unknown form factors associated with short range physics, the NN theory can describe all three form factors quite well.*

It seems likely that any nucleon model with a *consistent and complete* description of the current (c.f. Table 5) can do as well. The reasonable results obtained from the FSR and DB models are probably due to the fact that they have consistent, complete currents not based on an expansion in powers of $(v/c)^2$ (which must fail at high Q^2).

3.9. Future prospects

3.9.1. Future prospects for A From the discussions in Sec. 3.8 above, it is clearly of interest to extend measurements of A to higher Q^2. An *ed* coincidence experiment is straightforward, but prohibitive timewise with present accelerators. The proposed 12 GeV JLab upgrade allows one to take advantage of the approximate E^2 scaling of σ_M at constant Q^2 and high energy [130]. A large acceptance spectrometer such as MAD would be very helpful. Depending on the details of the upgrade, a one month experiment could provide data to Q^2 of 8 GeV^2.

It might also be desirable to do a new, high precision experiment at *low Q^2*. The goal of this experiment would be to resolve the discrepancy between the data sets of Refs. [39] and [40], and to check the low Q^2 limit of the relativistic calculations. These measurements require little time, but do require excellent control of systematic uncertainties, at the level of $1 - 2\%$, if they are to be meaningful.

3.9.2. Future prospects for B A hasty examination of Fig. 22 might lead one to believe that the problems with B are mainly theoretical, and that there is no need for new data. We believe this attitude would be inappropriate for two reasons. First, some of the calculations shown in the figures are in early stages of development, and will improve before any new data are available. The number of calculations is a reflection of the challenge that the high Q^2 data present, and a reflection of interest in, and knowledge of relativistic methods that is emerging from the study of these measurements. Second, and most important, measurements of B vary by 5 orders of magnitude. The existence and position of the first minimum has not yet been firmly established, and the location and existence of a possible second minimum is unknown. These minima in B (if they exist) result from cancellations of various physical effects and provide a very precise test of any theory.

As indicated above, measurements of B do not require high energy, but do require large scattering angles, as close as possible to 180°. At 180°, beam energies of 1 to 2 GeV cover a Q^2 range from 1.4 GeV^2 to 5 GeV^2.

The SLAC NE4 experiment was a heroic effort, run with *ed* coincidences. Energy resolution was limited by thick targets, 20 - 40 cm long. There was a large but manageable background of π^- in the e^- spectrometer, about 3 or 4 to 1, and an extremely large proton background from $\gamma d \rightarrow pn$ in the deuteron channel - up to two events per beam pulse were seen in the worst kinematics. Since NE4 ran at beam currents of up to 50 mA instantaneous, with a duty factor of about 0.3×10^{-3}, corresponding to an average current of about 15 μA, the JLab continuous beam structure essentially eliminates random coincidence backgrounds such as these. Background coincidence reactions included $\gamma d \rightarrow \gamma d$ and $\gamma d \rightarrow \pi^0 d$ at 180°, with the photon producing an electron detected in the electron channel. The spectrum of these photoreactions ends near the elastic peak, allowing the background contributions to be fit and determined. A JLab experiment would run with both larger spectrometer acceptance and higher luminosity to increase rates, but with a shorter target to reduce these backgrounds.

The proposed configuration [130] would use the Hall A septum magnets to detect the forward-going deuterons at angles of 3 - 6°, along with special electron channels to detect scattered electrons at about 160 - 170°. Based on the SLAC NE4 cross sections, a one month experiment can map out B to about 6 GeV^2.

3.9.3. Future prospects for t_{20} Extending t_{20} or other polarization observables to higher Q^2 is quite difficult [131, 132, 133]. There are three obvious possibilites.

Recoil tensor polarimetry requires a well calibrated polarimeter with a large figure

of merit, but no such device exists. For example, POLDER, used in the JLab Hall C t_{20} experiment, relied on the $^1H(\vec{d}, pp)n$ reaction, for which the figure of merit decreases at larger energies, leading to a practical upper limit in Q^2, that was reached in E94-018. HYPOMME [134, 135, 136] is promising, but not well enough calibrated.

The combination of polarized electron beams with recoil vector polarimeters is an untested possibility [137]. With A, B, and G_M known, p_z is calculable and can calibrate the polarimeter analyzing power, while p_x determines the form factor combination $G_C + \eta G_Q/3$. (The ratio of the two polarization components depends on this combination of form factors, times kinematic factors and divided by G_M.) Since the JLab polarized source can provide 50 – 100 μA beams, there is no luminosity problem. The difficulty with this measurement is that the polarization components are expected to be small in the Q^2 range of interest, ≈ 0.01, and $p_x/p_z \sim 5$ – 10. A one month measurement for one Q^2 of ≈ 2 - 2.5 GeV^2 can determine the *polarization components* well, but if these are small as expected, the *form factors* can only be extracted with factor of two uncertainties.

An alternative is to use asymmetries from a polarized target. However, the reduced currents that can be used with polarized targets require a large acceptance detector such as CLAS, to make up for the lack of luminosity. Also, although current polarized targets have moderately large deuteron vector polarizations, tensor polarizations are small. Furthermore, the asymmetry varies as $P_2(\hat{n}\cdot\hat{q})$, with $\hat{n}$ the polarization direction, so it is desirable to have complete azimuthal coverage, with $\hat{n}$ in the direction of $\hat{q}$ at one azimuthal angle, rather than being purely transverse. Extensive beam time would be needed, either as an external polarized target experiments at JLab, or as an internal polarized target experiment at HERMES. We note that a series of moderate Q^2 measurements are planned with the MIT Bates BLAST detector [138], for Q^2 from 0.1 to 0.9 GeV^2.

Proposed next generation colliders, such as EPIC/ERHIC, are promising due to large planned luminosities; for this experiment the lower proposed c.m. collision energies are desirable for ensuring exclusivity. The spin direction of the polarized deuteron beam must be controllable. In collider kinematics, the scattered electron and deuteron energies are close to their respective beam energies and are slow functions of Q^2, while the scattering angles for fixed Q^2 vary slowly with the beam energies. Thus, if an experiment is possible, it would attempt large azimuthal coverage of coincidence $e\vec{d}$ elastic scattering, with the outgoing particles at angles from a few to about 20° from the beam line.

3.10. Conclusions to Section 3

Comparison of theory and experiment leads to the following conclusions:

- Nonrelativistic quantum mechanics (without exchange currents or relativistic effects) is ruled out by the $A(Q^2)$ data at high Q^2. Reasonable variations in nucleon

form factors or uncertainties in the nonrelativistic wave functions cannot remove the discrepancies.

- In some relativistic approaches using NN degrees of freedom only, short range physics not calculable within the model (F_3 or $f_{\rho\pi\gamma}$, for example) can be adjusted to give good agreement with all the data.

- Different ways of calculating relativistic effects (or meson exchange currents) can give results that differ substantially from each other. Even at low Q^2, where all calculations are constrained, these differences are larger than errors in the data. This is not understood, but may be due to the failure of some models to use realistic currents.

- The deuteron form factors provide no evidence for the onset of perturbative QCD, but quark cluster models could explain the data.

Study of the experimental situation leads to the following conclusions:

- A good database of A, B, and t_{20} measurements has been obtained; while discrepancies exist they are generally not large enough to affect the theoretical interpretation.

- The minimum of B is very sensitive to details of the models, and improved measurements of B for Q^2 in the region 1.5 - 4 GeV^2 are particularly compelling. It is important to accurately map out the zero in the B structure function.

- Detailed disagreements between theories and different data sets suggests the need for precision studies at low Q^2.

4. Deuteron Electrodisintegration

4.1. Introduction

As the deuteron has no excited bound states, inelastic scattering experiments have largely consisted either of (i) measurements in which the final state mass, W, is very close to $2m$ (referred to as *threshold electrodisintegration* even when Q^2 is very large because the final state is close to the NN scattering threshold), (ii) measurements near the quasifree peak (defined by the condition that the "spectator" nucleon remain at rest), or (iii) deep inelastic scattering in which both Q^2 and W become very large. We will not discuss deep inelastic scattering in this review. For processes at modest energies near the quasielastic peak, a rough estimate of the cross section can be made using the *unrealistic* plane wave impulse approximation (PWIA) in which all final state interactions are ignored. Denoting the momentum of the outgoing struck nucleon by $\mathbf{p}_1$, the cross section in PWIA is proportional to

$$d\sigma_{\text{PWIA}} \simeq G_N^2(Q^2) \left\langle \Psi(\mathbf{p}_1 - \mathbf{q}) \right\rangle^2 \tag{98}$$

where G_N^2 is some combination of the squares of the electric and magnetic form factors of the nucleon, and $\langle \Psi(\mathbf{p}) \rangle^2$ is an average of the square of the momentum space wave
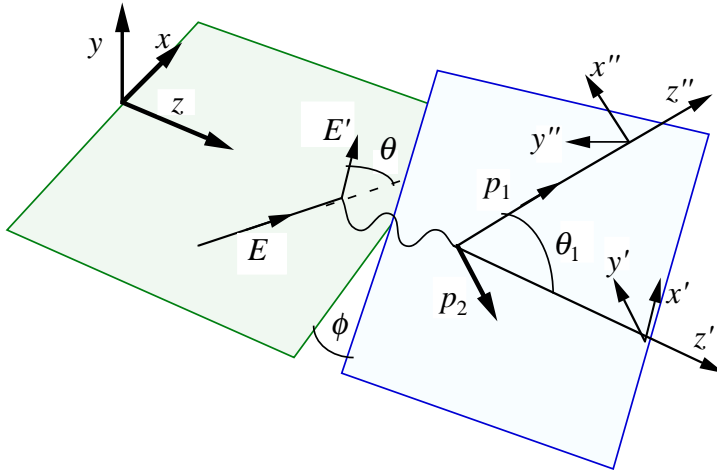
Figure 24. The kinematics of electron scattering when the initial hadronic state is broken into two fragments with momenta p_1 and p_2.

function of the deuteron with internal relative momentum **p**. Were the PWIA realistic, Eq. (98) shows that inelastic scattering in quasielastic kinematics would provide a direct measure of the (square) of the deuteron wave function. While the PWIA is overly simplistic, it does illustrate (correctly) one of the central justifications for quasielastic measurements.

Within the context of a more realistic dynamical theory, one can use response function separations and polarization observables to enhance the sensitivity to various model dependent *nonobservables*, such as momentum distributions, meson-exchange currents, and medium modifications. One strong recent interest has been to choose kinematics in which the unobserved nucleon has a large momentum; the plane wave approximation shows that this configuration enhances sensitivity to initial-state short range correlations (i.e. the wave function) and possible quark effects. A number of these experiments have been carried out at various accelerators, but no experiments at JLab have yet reported results. Thus, an experimental review of this topic is unwarrented at this time. However, because photodisintegration, electrodisintegration, and threshold electrodisintegration are closely related theoretically, we present the theoretical background for these processes below.

4.2. Cross section and polarization observables

In this subsection the cross section and polarization observables for electrodisintegration and photodisintegration to an *np* final-state are reviewed briefly. (We do not discuss pion and meson production.) The electroproduction cross sections will be obtained first, and photoproduction will then be treated as a special case.

4.2.1. Electrodisintegration The most general decomposition of the $d(e, e'p)n$ coincidence cross section was first discussed by Donnelly and Raskin [139]. Here we will follow the later work of Ref. [140]. The cross section can be shown to have the form (Eq. (95) of Ref. [140])

$$\frac{d^5\sigma}{d\Omega dE'd\Sigma} = \frac{\sigma_M}{4\pi m_d}\frac{Q^2}{\mathbf{q}_L^2}\left\{\tilde{R}_L^{(\mathrm{I})} + s_T\tilde{R}_T^{(\mathrm{I})} - \frac{1}{2}\left[\cos 2\phi\tilde{R}_{TT}^{(\mathrm{I})} + \sin 2\phi\tilde{R}_{TT}^{(\mathrm{II})}\right]\right.$$
$$+ s_{LT}\left[\cos\phi\tilde{R}_{LT}^{(\mathrm{I})} + \sin\phi\tilde{R}_{LT}^{(\mathrm{II})}\right] + 2h\,s_{T'}\tilde{R}_{T'}^{(\mathrm{II})}$$
$$\left. + 2hs_{LT'}\left[\sin\phi\tilde{R}_{LT'}^{(\mathrm{I})} + \cos\phi\tilde{R}_{LT'}^{(\mathrm{II})}\right]\right\}, \tag{99}$$

where, in the lab frame, $q = \{\nu, \mathbf{q}_L\}$, and the nine response functions are functions of $Q^2 = -q^2$, $\nu = Q^2/2mx$, and the scattering angle θ_1 of the final-state proton (measured in a coincidence experiment and integrated over in an inclusive measurement). The ejectile plane is tilted at an angle ϕ with respect to the electron scattering plane, as illustrated in Fig. 24. The Mott cross section and other variables are as defined in Eq. (23). The electron kinematic factors are

$$s_T = \frac{1}{2} + \xi^2 \qquad\qquad s_{LT} = -\frac{1}{\sqrt{2}}\left(1 + \xi^2\right)^{\frac{1}{2}}$$
$$s_{T'} = \xi\left(1 + \xi^2\right)^{\frac{1}{2}} \qquad s_{LT'} = -\frac{1}{\sqrt{2}}\xi\,, \tag{100}$$

with $\xi = |\mathbf{q}_L|Q^{-1}\tan(\theta/2)$.

One of the virtues of Eq. (99) is that the response functions $\tilde{R}$ are *covariant*, and hence (99) it can be used to describe the cross section in either the c.m. of the outgoing np pair or the laboratory frame, provided we use the appropriate form of $d\Sigma$:

$$d\Sigma|_{c.m.} = |\mathbf{p}_{1_{c.m.}}|\,d\Omega_{1_{c.m.}}$$
$$d\Sigma|_{LAB} = |\mathbf{p}_{1_L}|\mathcal{R}\,d\Omega_{1_L}\,, \tag{101}$$

where $\mathcal{R}$ is the lab recoil factor

$$\mathcal{R} = \frac{W}{m_d}\left(1 + \frac{\nu p_1 - E_1 q\cos\theta_1}{m_d p_1}\right)^{-1}_L \tag{102}$$

with W the invariant mass of the outgoing pair.

In any frame the nine response functions of (99) are related to the components of the deuteron response tensor $R_{\lambda_\gamma\lambda'_\gamma}^{(\mathrm{X})}$

$$R_{\lambda_\gamma\lambda'_\gamma}^{(\mathrm{X})} = \frac{m^2}{4\pi^2 W}\sum_{\lambda'_1\lambda_1}\sum_{\lambda_2}\sum_{\lambda'_d\lambda_d}\rho_{\lambda_1\lambda'_1}^{N\,(\mathrm{X})}\left\langle\lambda'_1\lambda_2\left|J_{\lambda_\gamma}(q)\right|\lambda_d\right\rangle\rho_{\lambda_d\lambda'_d}^d\left\langle\lambda'_d\left|J_{\lambda'_\gamma}^\dagger(q)\right|\lambda_1\lambda_2\right\rangle \tag{103}$$

with X = I or II, and

$$\tilde{R}_L^{(\mathrm{I})} = R_{00} \qquad\qquad \tilde{R}_T^{(\mathrm{I})} = R_{++} + R_{--}$$
$$\tilde{R}_{LT}^{(\mathrm{I})} = 2\mathrm{Re}(R_{0+} - R_{0-}) \qquad \tilde{R}_{TT}^{(\mathrm{I})} = 2\mathrm{Re}R_{+-}$$
$$\tilde{R}_{LT'}^{(\mathrm{I})} = 2\mathrm{Im}(R_{0+} - R_{0-}) \qquad \tilde{R}_{T'}^{(\mathrm{II})} = R_{++} - R_{--}$$
$$\tilde{R}_{LT}^{(\mathrm{II})} = 2\mathrm{Im}(R_{0+} + R_{0-}) \qquad \tilde{R}_{TT}^{(\mathrm{II})} = -2\mathrm{Im}R_{+-}$$
$$\tilde{R}_{LT'}^{(\mathrm{II})} = 2\mathrm{Re}(R_{0+} + R_{0-})\,. \tag{104}$$

All of these quantities are written in the helicity basis, with λ_γ the helicity of the virtual photon, λ_1 and λ_2 the helicities of particles 1 and 2 in the final-state, and λ_d the helicity of the initial deuteron. The matrix element of the helicity-basis current operator between helicity states is represented by $\langle \lambda_1 \lambda_2 | J_{\lambda_\gamma}(q) | \lambda_d \rangle$. In cases where the deuteron target might be polarized *only* in the $\hat{y}$ direction, and where *only* the polarization of the outgoing particle 1 might be measured, the spin density matrices for particle 1 in the final state is given by $\rho^{N(\mathrm{X})}$ and that of the deuteron in the initial state by ρ^d, where

$$\rho^d_{\lambda\lambda'} = \frac{1}{3}\left\{\delta_{\lambda\lambda'} + i\,p^d_y\left(-i\sqrt{2}\mathcal{S}_y\right)_{\lambda\lambda'}\right\} = \frac{1}{3}\begin{pmatrix} 1 & -i\,p^d_y & 0 \\ i\,p^d_y & 1 & -i\,p^d_y \\ 0 & i\,p^d_y & 1 \end{pmatrix}$$

$$\rho^{N(\mathrm{I})}_{\lambda\lambda'} = \frac{1}{2}\left(1 + p^N_y\,(\sigma_y)_{\lambda\lambda'}\right) \qquad \rho^{N(\mathrm{II})}_{\lambda\lambda'} = \frac{1}{2}\left(p^N_x\,(\sigma_x)_{\lambda\lambda'} + p^N_z\,(\sigma_z)_{\lambda\lambda'}\right) \quad (105)$$

where $\mathcal{S}_y$ is the $\hat{y}$ component of the spin-one matrix, $p^d_y = \sqrt{3/2}\,\mathrm{Im}T_{11}$ is the vector polarization of the deuteron target, p_i is the direction of the polarization of outgoing particle 1, measured with respect to the $x''y''z''$ coordinate system shown in Fig. 24, and σ_i are the Pauli matrices. Note that only those response functions of type I (denoted by the superscript) are nonzero if all of the hadrons are unpolarized; type II response functions require (for the cases considered here) measurement of the polarization of the outgoing nucleon. Further details and additional cases can be found in Ref. [140].

The familiar unpolarized inclusive cross section is easily obtained by integrating (99) in the c.m. and summing over electron polarizations. The result is

$$\frac{d^3\sigma}{d\Omega'dE'} = \sigma_M\left\{W_2(Q^2,\nu) + 2W_1(Q^2,\nu)\tan^2\theta/2\right\}, \tag{106}$$

with

$$W_1(Q^2,\nu) = \frac{|\mathbf{p}_{1c.m.}|}{4m_d}\int_{-1}^{1} d\cos\theta_{1c.m.}\ \tilde{R}^{(\mathrm{I})}_T(Q^2,\nu,\theta_{1c.m.})$$

$$W_2(Q^2,\nu) = \frac{|\mathbf{p}_{1c.m.}|Q^2}{2m_d\,\mathbf{q}_L^2}\int_{-1}^{1} d\cos\theta_{1c.m.}\ \left\{\tilde{R}^{(\mathrm{I})}_L(Q^2,\nu,\theta_{1c.m.}) + \frac{1}{2}\tilde{R}^{(\mathrm{I})}_T(Q^2,\nu,\theta_{1c.m.})\right\}, \quad (107)$$

4.2.2. Photodisintegration For real photons the longitudinal components are absent, and the cross section simplifies (there is no electron scattering plane and no electron kinematics). The most general polarization of the incoming photon, ϵ, is therefore a superposition of the circular polarization states $\epsilon_\pm$, which we write as $\epsilon = a_+\epsilon_+ + a_-\epsilon_-$ with $|a_+|^2 + |a_-|^2 = 1$. The expansion coefficients $a_\pm$ can therefore be written in terms of only three independent parameters

$$\begin{aligned} a_+ &= -\cos\beta\,e^{-i(\phi+\alpha)} \\ a_- &= \sin\beta\,e^{\,i(\phi-\alpha)} \end{aligned} \tag{108}$$

with $0 \le \beta \le \pi/2$. The coincidence cross section for a polarized photon beam is then

$$\frac{d^2\sigma}{d\Sigma_0} = \frac{1}{2}\tilde{R}^{(\mathrm{I})}_T + \frac{1}{2}\left(|a_+|^2 - |a_-|^2\right)\tilde{R}^{(\mathrm{II})}_{T'} + \mathrm{Re}(a_+a_-^*)\tilde{R}^{(\mathrm{I})}_{TT} + \mathrm{Im}(a_+a_-^*)\tilde{R}^{(\mathrm{II})}_{TT}$$

$$= \frac{1}{2}\left\{\tilde{R}^{(\mathrm{I})}_T + p_+\tilde{R}^{(\mathrm{II})}_{T'} - p_\gamma\tilde{R}^{(\mathrm{I})}_{TT}\cos 2\phi - p_\gamma\tilde{R}^{(\mathrm{II})}_{TT}\sin 2\phi\right\}, \tag{109}$$

where $p_+ = \cos 2\beta$ and $p_\gamma = \sin 2\beta$ are the fractions of right circular and linear photon polarizations, respectively, and $d\Sigma_0$ depends on the frame

$$
d\Sigma_0|_{c.m.} = d\Omega_{1_{c.m.}} \left(\frac{|\mathbf{p}_1|}{4\nu W} \right)_{c.m.}
$$

$$
d\Sigma_0|_{LAB} = d\Omega_{1_L} \left(\frac{|\mathbf{p}_1|}{4\nu m_d} \right)_L \mathcal{R} \,, \tag{110}
$$

with $\mathcal{R}$ defined in Eq. (102). We will return to the cross section (109) in Sec. 5.

4.2.3. Theoretical Issues It is important to appreciate that these formulae for the cross section are *exact* relativistic results (subject only to the one photon exchange approximation). All of our ignorance is confined to the hadronic matrix elements of the current

$$
J^{\lambda_\gamma}_{\lambda_1\lambda_2\lambda_d}(p_1 p_2, q) = \left\langle \lambda_1 \lambda_2 \left| J_{\lambda_\gamma}(q) \right| \lambda_d \right\rangle \,, \tag{111}
$$

and the structure functions (104) that are products of these currents.

In much of the older literature, particularly for studies of the $(e, e'p)$ reaction from nuclei with mass number $A > 2$ [141], the cross section is written

$$
\frac{d^5\sigma}{d\Omega dE' d\Sigma} = \mathcal{K} \, \sigma_{ep} \, S(p, E_s) \,, \tag{112}
$$

where $\mathcal{K}$ is a kinematic factor, σ_{ep} is cross section for scattering of an electron from an "off-shell" proton, and $S(p, E_s)$ is the proton spectal function (which gives the probability of finding a proton with momentum p and separation energy E_s in the target nucleus). The proton momentum distribution is obtained by integrating the spectral function over the separation energy

$$
n(p) = \int dE \, S(p, E) \,. \tag{113}
$$

Some early experiments focused on "measuring" the momentum distribution and the spectral function. While this picture has a nice physical interpretation [it is motivated by the PWIA, Eq. (98)], and presenting data this way is sometimes useful, particularly in the early phases of the program, it is important to realize that the individual structure functions that enter the exact cross section (99) are, in general, *independent* functions which are *not* proportional to each other, and that therefore Eq. (112) is *only an approximation* to the cross section [142]. Attempts to refine the definitions of σ_{ep} and $S(p, E_s)$ can have limited value at best, and at worst can lead to many unproductive debates about the precise definition of the spectral function.

Calculation of the hadronic current matrix elements (111) is complicated by requirement that the current be conserved, $q_\mu J^\mu = 0$. For elastic scattering, where the initial and final states are identical, invariance under time inversion usually guarantees that even simple approximations to the dynamics will satisfy this constraint. But building in current conservation for inelastic processes usually requires consistent treatment of both final-state interactions and interaction currents. The failure of approximate calculations (and the PWIA in particular) to satisfy current conservation

is often seen as a serious obstacle. Some *ad hoc* prescription of the kind introduced by De Forest [143], is needed.

We propose the simple prescription introduced recently in the study of deep inelastic scattering [144]. Suppose the *exact* current is composed of two parts $J^\mu = J_1^\mu + J_2^\mu$. In general, *neither* of these two parts will satisfy current conservation *alone*; that is $q_\mu J_i^\mu \neq 0$ for each i. However, since the exact current satisfies current conservation, $q_\mu(J_1^\mu + J_2^\mu) = 0$. We propose replacing each of the individual terms in the current by

$$J_i^\mu \to J_{Ti}^\mu = J_i^\mu - \frac{q^\mu\, q_\nu J_i^\nu}{q^2}\,. \tag{114}$$

This procedure is covariant, guarantees that each component conserves current (so that one can be calculated without knowing the other), and that their sum is unchanged: $J_1^\mu + J_2^\mu = J_{T1}^\mu + J_{T2}^\mu$. Perhaps the best argument can be found in Ref. [144] where it was shown (for a very simple case) that the Born term defined in this way dominates the final-state interaction term in the deep inelastic limit, resolving a long standing puzzle. Finally, note that $J_{i\epsilon_\gamma} \equiv \epsilon_{\gamma\mu}J_i^\mu = \epsilon_{\gamma\mu}J_{Ti}^\mu$ (where ϵ_γ are the virtual photon polarization vectors satisfying $\epsilon_\gamma \cdot q = 0$) so that the response tensor (103) is *unaffected* by the redefinition (114)!

We now turn to a brief discussion of threshold electrodisintegration.

4.3. Threshold Electrodisintegration

4.3.1. Overview Threshold deuteron electrodisintegration measures the $d(e, e')pn$ reaction in kinematics in which the proton and neutron, rather than remaining bound, are unbound with a few MeV of relative kinetic energy in their center of mass system. If the final-state energy is low enough, the final state will be dominated by transitions to the $^1S_0$ final state, and will be a pure $\Delta S = 1$, $\Delta I = 1$, $M1$ transition, similar to the $N \to \Delta(1232)$ transition. This transition is a companion to the B structure function; both are magnetic transitions and both are filters for exchange currents with only one isospin ($d \to d$ is $\Delta I = 0$ and $d \to {}^1S_0$ is $\Delta I = 1$). To see the similarity, compare the top right panel of Fig. 22 with the threshold measurements shown in Fig. 25. Both have a similar shape, and in both cases the uncertainties in the theoretical predictions are large.

The similarity of these two processes (elastic and threshold inelastic) also holds for the theory. These two processes can be used to separately determine the precise details of the $I = 0$ and $I = 1$ exchange currents. Once the exchange currents are fixed, they can be used to predict the results of $d(e, e'p)n$ over a wide kinematic region. Any theoretical approach that works for the form factors should also work equally well for threshold electrodisintegration, yet very few of the groups who have calculated form factors have also calculated the threshold process. This may be due in part to the fact that the $I = 1$ interaction currents are larger than the $I = 0$ interaction currents, making the threshold electrodisintegration calculation more difficult than the elastic calculation. A more definitive test of the various relativistic approaches discussed in

the previous sections will be possible once the elastic calculations are extended to the threshold inelastic process.

Previous threshold electrodisintegration experiments have reported an *average* cross section that can be obtained theoretically by integrating the relative pn energy in the final state, E_{pn}, from 0 to 3, or (in some cases) 0 to 10 MeV. The unbound $^1S_0$ final state dominates at threshold (because the $^3S_1$-$^3D_1$ scattering state is orthogonal to the deuteron state at threshold), but above threshold there are contributions from the $^3S_1$-$^3D_1$ scattering state, and eventually from the NN $L = 1$ scattering states as well. To emphasize this magnetic transition, data have been taken at large electron scattering angles, mostly 155° or 180°.
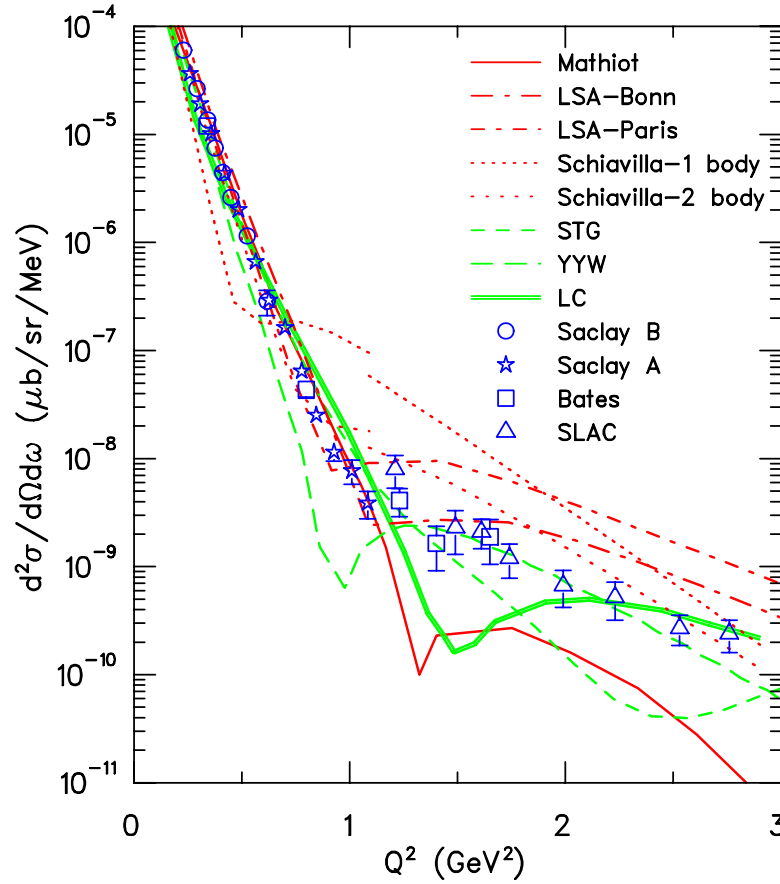
Threshold electrodisintegration provides strong evidence (perhaps the best we have) for the existence of isovector exchange currents [145]. The impulse approximation calculation of the transition to the $^1S_0$ final state has a zero arising from the negative interference between the $^3S_1 \rightarrow^1 S_0$ and $^3D_1 \rightarrow^1 S_0$ pieces of the transition that lead to a minimum at Q^2 near 0.5 GeV^2. This minimum is not seen in the data, and theoretical calculations of the $I = 1$ exchange current contribution fill in the minimum and explain the data.

4.3.2. Current status of theory and data Experiments have measured $d(e, e')pn$ threshold electrodisintegration to Q^2 about 1.6 GeV^2 with better than 1 MeV (σ) resolution, integrating up to $E_{pn} = 3$ MeV [35, 54, 146, 147, 148, 149, 150], and to nearly 3 Gev^2 with 12 - 20 MeV (FWHM) resolution, and integrating up to $E_{pn} = 10$ MeV [151, 152].‖

Figure 25 shows the smooth rapid fall off of threshold electrodisintegration cross sections for Q^2 up to about 1.2 GeV^2, and the change in slope for the higher Q^2 SLAC and Bates data. There is good agreement between the various measurements, including those not shown, considering the change in scattering angle (155° for Saclay, 160° for Bates, 180° for SLAC) and integration region for E_{pn} (0-3 MeV for Saclay and Bates data shown, 0-10 MeV for SLAC). The figure also shows results from seven theoretical calculations.

The oldest calculation shown in the figure is from Mathiot [153]. This model includes one and two body currents based on π and ρ exchange, and also contributions to the two-body current operator from the exitation of the Δ. Mathiot confirms that

‖ One possible source of confusion in any close examination of threshold electrodisintegration is the use of two different conventions for the cross section. Early articles [147, 148] and the most recent Bates article [150] report the cross section as $d^2\sigma/d\Omega d\omega = d^2\sigma/d\Omega dE'$ where ω (E') is the energy transfer (scattered electron energy). The SLAC articles [151, 152] and first Bates article [149] use instead $d^2\sigma/d\Omega dE_{np}$, where E_{np} is the total np kinetic energy in their c.m. frame, $E_{np} = W - m_d - 2.225 (MeV)$. (A typographical error at one point in [152] misidentifies E_{np} as the energy of a nucleon, rather than the two nucleons.) These cross sections are related by the Jacobian $|dE_{np}/dE'| = (m_d + 2E \sin^2(\theta/2))/W$ which numerically ranges from about 1.3 to 2.3 for the data that we present. The articles showing the "dE_{np}" cross sections appear to plot the Saclay cross sections as published, as "dE'" cross sections, rather than converted.

Figure 25. The cross section for threshold electrodisintegration of the deuteron. Data shown are from Saclay B [147], Saclay A [148], Bates [149, 150], and SLAC [151, 152]. Theory calculations are from Mathiot [153], LSA [154], Schiavilla [155], STG [156], YYW [157], and LC [158].

the one body current (the impulse approximation) produces a sharp minimum in the cross section at about $Q^2 = 0.5$ GeV^2 (in agreement with the recent Schiavilla-1 body curve shown in the figure and in complete disagreement with the data) and that the π exchange current fills this in, shifting the minimum to about 1 GeV^2. The ρ exchange is also important, shifting the mimimum to $Q^2 \simeq 1.4$ GeV^2. Contributions from the electroexication of a Δ are smaller, at least below $Q^2 \simeq 1$ GeV^2. Figure 25 shows that this calculation breaks down above $Q^2 \simeq 1$ GeV^2, probably because it does not include many of the contributions included in modern calculations. More recent calculations, also based on hadronic degrees of freedom, are from Leidemann, Schmidtt, and Arenhövel [LSA] [154] and Schiavilla. (The calculations by Schiavilla shown on the figure are based on the work of Ref. [91], but use the more recent Argonne AV18 potential. These curves were also published in the review [155].) In both of these cases the details are largely unpublished and the inelastic calculations are not as up-to-date as the corresponding elastic calculations recently done by the same groups, so it is premature to draw definite conclusions. The work of Smejkal, Truhlík, and Göller

[STG] [156] obtains exchange current contributions from the $\pi \rho a_1$ system using a chiral lagrangian, and does a good job describing the data out to 2 GeV^2. Predictions from two quark cluster models, the early model of Yamauchi, Yamamoto, and Wakamatsu [YYW] [157], and the more recent model of Lu and Cheng [LC] [158], are also shown in Fig. 25. These calculations both tend to have too much structure in the region of the shoulder, but do show that quark cluster models have the ability to describe the exchange currents needed to account for the data.

The recent improvements in relativistic theory discussed in Sec. 3.6 will lead to a new generation of calculations that will rely on threshold electrodisintegration to provide details about the nature of the $I = 1$ exchange currents. The most precise constraint on these currents comes from the $d \to {}^1S_0$ transition, and this part of the transition is partly obscured by the poor energy resolution of the existing high Q^2 measurements. A new and improved experiment at JLab with higher resolution would allow the threshold $d \to {}^1S_0$ process to be better extracted, with a better resulting determination of the isovector exchange currents. It is also important to determine whether or not there is a minimum near 1.2 GeV^2. This present indication of a minimum might be an artefact of the end of the Saclay data [148] vs. the start of the SLAC data [151, 152], along with systematic uncertainties of these and the Bates measurements [149, 150].

A high statistics high resolution measurement at large Q^2 is feasible. Measurements have been proposed [159] with 1.5 MeV resolution at a scattering angle of 160°. The experiment would use Hall A with the HRS spectrometer vacuum coupled to the scattering chamber, and a special cryotarget and collimators to enhance resolution and reduce backgrounds. Measurements were proposed for 6 points from 1 to 3.7 GeV^2.

We note that SLAC NE4 simultaneously measured the threshold electrodisintegration along with the elastic structure function B. Because the large Q^2 threshold inelastic cross section is typically an order of magnitude larger, the $d(e, e')$ measurements see essentially only the inelastic processes, and $d(e, e'd)$ is needed to determine the elastic scattering. If it is possible to maintain large solid angle for the elastic scattering, and good resolution for the threshold electrodisintegration, both data sets can be obtained simultaneously.

5. Deuteron Photodisintegration

5.1. Introduction

Deuteron photodisintegration was first investigated in the early 1930s, in order to understand the structure of the neutron. After the discovery of the neutron by James Chadwick, attention turned to its mass and structure. Was the neutron a fundamental particle, like the proton and electron, or was it a bound state of the electron and proton, different from the hydrogen atom? If it was a bound state of the proton and electron, how were the electrons confined into the small nuclear volume? Conflicting experimental evidence on the neutron mass prevented resolution of the issue until 1934,

when Chadwick and Maurice Goldhaber used deuteron photodisintegration [160] to determine that the neutron mass was slightly heavier than that of the hydrogen atom. Thus, the neutron, being heavier than the proton plus electron, was a fundamental particle, and there was no longer any basis for thinking electrons could be present in nuclei [161].

Subsequently, deuteron photodisintegration cross sections have served as a standard test case for nuclear theory. The effects, for example, of the Δ resonance in cross sections for beam energies near 300 MeV are pronounced, but until recently large discrepancies between different experimental data sets made precise tests of theories difficult [162]. The 1960s-1970s saw the start of polarization measurements. The earliest data were intermediate energy measurements of the induced proton polarization [163] and low energy measurements of the induced neutron polarization [164]. Large induced polarizations were observed [165, 166] soon afterward, particularly for energies above the Δ resonance and for center of mass angles near 90°. The combination of more extensive confirming measurements [167] for E_γ about 350 - 700 MeV, which could not be reproduced theoretically, and interest in dibaryons led to much excitement about deuteron photodisintegration in the late 1970s and early 1980s. There were many serious theoretical efforts, numerological studies involving inclusion of dibaryon resonances, and extensive experimental studies of cross sections and polarization observables.

5.2. Relation between elastic scattering and photodisintegration

Since *both* the recent deuteron form factor measurements *and* the recent high energy deuteron photodisintegration measurements have been made with 4 GeV electron beams, it is sometimes assumed that the same theory should work for both. In this review we emphasize that this need not be the case. The kinematics of elastic electron-deuteron scattering and deuteron photodisintegration are very different, and the physics being explored by these two measurements is also very different. The implications of this remarkable feature of electronuclear physics, often not fully appreciated, will be discussed briefly in this section.

The kinematics of elastic scattering and photodisintegration are compared in Fig.26, which shows $W^2 - m_d^2$ as a function of the photon (real or virtual) energy

$$W^2 - m_d^2 = 2m_d\nu \left(1 - \frac{m\,x}{m_d}\right) , \tag{115}$$

where $x = Q^2/2m\nu$ and $\nu = E_\gamma$ for real photons. The mass of the final excited state increases rapidly as x decreases below its maximum allowed value of $x = m_d/m \simeq 2$. For any energy ν or any Q^2, elastic ed scattering leaves the pn system bound, with no internal excitation energy added to the two nucleons. For quasifree scattering ($x = 1$) the mass of the final pn system grows with ν, and as x decreases below 1 the mass grows more rapidly with ν. As $x \to 0$, we approach the real photon limit. Real photons produce the maximum value of W of any given beam energy. With each 1 GeV of beam energy $W - m_d$ increases by approximately 500 MeV, driving the final state deep
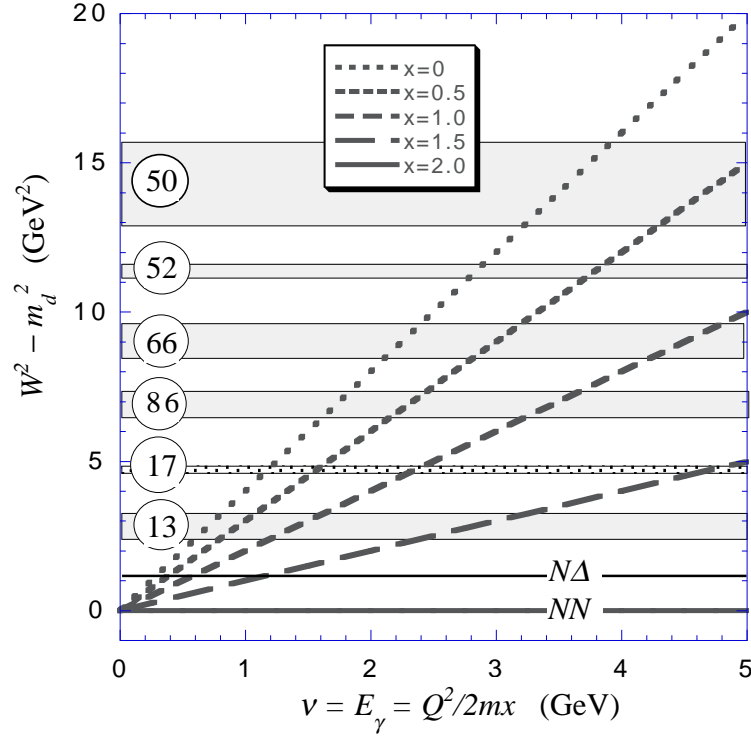
Figure 26. The variation of W^2 with the photon energy ν for various values of x, as given by Eq. (115). The shaded regions show the approximate thresholds for the production of bands of nucleon resonances, as discussed in the text and shown in Table 7. The numbers in the small circles are the number of distinct channels in each band.

Table 6. The 24 well established nucleon resonances listed in the *Particle Physics Booklet* [168] fall into the 8 bands listed below. Masses of *neighboring* resonances in each band are less than 150 MeV apart. All of these resonances can contribute to deuteron photodisintegration for $W < 4.5$ GeV. All but N_4 and Δ_4 can contribute in all combinations, giving $13 + (13 \times 12)/2 = 91$ channels with two $I = 1/2$ particles, 45 channels with two $I = 3/2$ particles, and 117 channels with one $I = 1/2$ and one $I = 3/2$ particle. The number of additional channels contributed by N_4 and Δ_4 is shown on the table and totals 33 channels. The total number of channels is 286.

	$I = 1/2$			$I = 3/2$	
N_1	N (939)		Δ_1	$P_{33}(1232)$	
N_2	$P_{11}(1440)$, $D_{13}(1520)$, $S_{11}(1535)$, $S_{11}(1650)$, $D_{15}(1675)$, $F_{15}(1680)$, $D_{13}(1700)$, $P_{11}(1710)$, $P_{13}(1720)$		Δ_2	$P_{33}(1600)$, $S_{31}(1620)$, $D_{33}(1700)$	
N_3	$G_{17}(2190)$, $H_{19}(2220)$, $G_{19}(2250)$		Δ_3	$F_{35}(1905)$, $P_{31}(1910)$, $P_{33}(1920)$, $D_{35}(1930)$, $F_{37}(1950)$	
N_4	$I_{1,11}(2600)$	14 channels	Δ_4	$I_{3,11}(2420)$	19 channels

into the resonance region. The well established nucleon resonances, all of which can be excited by 4 GeV photons, are listed in Table 6, and the bands of thresholds at which

Table 7. The thresholds for the production of pairs of baryon resonances also fall into 8 bands. *Neighboring* thresholds within each band are less than 150 MeV apart. These bands are shown in Fig. 26.

Band	mass range	members	number of channels
$B_1 = NN$	1878	$N_1 N_1$	1
$B_2 = N\Delta$	2171	$N_1 \Delta_1$	1
B_3	2464 – 2579	$\Delta_1 \Delta_1, N_2 N_2, N_1 \Delta_2$	13
B_4	2858 – 2872	$N_2 \Delta_1, N_1 \Delta_3, \Delta_1 \Delta_2$	17
B_5	3155 – 3280	$\Delta_1 \Delta_3, N_2 N_2, N_2 \Delta_2, \Delta_2 \Delta_2$	86
B_6	3452 – 3652	$N_3 \Delta_1, N_1 \Delta_4, N_1 N_4, N_2 \Delta_3,$	
		$\Delta_2 \Delta_3, \Delta_1 \Delta_4$	66
B_7	3832 – 3860	$N_4 \Delta_1, \Delta_3 \Delta_3, N_2 N_3, N_3 \Delta_2,$	52
B_8	4046 – 4440	$N_2 \Delta_4, \Delta_2 \Delta_4, N_3 \Delta_3, N_2 N_4,$	
		$\Delta_2 N_4, \Delta_3 \Delta_4, N_3 N_3$	50

these resonances are excited, either singly or in pairs, are listed in Table 7 and shown in Fig. 26. [The Fermi momentum of the struck nucleon, and the widths of the resonances, will average these thresholds over a wider kinematic region than shown.] By $E_\gamma = 1.2$ GeV, the final-state mass is already reaching $W = 2$ GeV, the nominal onset of deep inelastic scattering (DIS) from a single nucleon if we assume one of the nucleons in the deuteron remains at rest. At $E_\gamma = 4$ GeV, the final-state mass is approximately 4.5 GeV, and at least 286 thresholds for the production of pairs of baryon resonances have been crossed (and there are probably more from unseen or weakly established resonances). A photon energy of 4 GeV corresponds to np scattering with a laboratory kinetic energy of about 8 GeV! (See also the kinematic argument given by Holt [169].)

It is clearly very difficult (if not impossible) to construct a theory of high energy photoproduction in which all of the 24 established baryon resonances and their corresponding 286 production thresholds are treated microscopically. By contrast, elastic electron deuteron scattering requires a microscopic treatment of only *one channel*. All of the 286 channels also contribute to elastic scattering, of course, but in this case they are not explicitly excited, and can probably be well described by slowly varying short-range terms included in a meson exchange (or potential) model. In photodisintegration, *each of these channels is excited explicitly*. As we shall see below, it is sufficiently difficult to construct an adequate theory in the region of the Δ resonance, so it is difficult to imagine this program being extended to a realistic treatment of many resonances, including intermediate states in which multiple mesons are present. It would instead appear that an alternate framework that *averages over the effects of many hadronic states* is needed. The alternatives are to use a Glauber-like approach, or to borrow from our knowledge of DIS and build models that rely on the underlying quark degrees of freedom. We will return to these issues in our review of the theory in Sec. 5.4 below.

5.3. Cross section and polarization observables

The photodisintegration cross section was previously given in Sec. 4.2.2. Including the polarization observables defined by the density matrices of Eq. (105), and using the notation of Ref. [140], the structure functions are

$$\tilde{R}_T^{(I)} \equiv \tilde{R}_T^{(I)}(p_y^N, \mathrm{Im}T_{11}, U) = R_T + p_y^N\, R_T(y) + p_y^d\, R_T(\mathrm{Im}T_{11})$$
$$\tilde{R}_{TT}^{(I)} \equiv \tilde{R}_{TT}^{(I)}(p_y^N, U) = R_{TT} + p_y^N\, R_{TT}(y)$$
$$\tilde{R}_{T'}^{(II)} \equiv \tilde{R}_{T'}^{(II)}(p_{x'}^N, p_{z'}^N) = p_{x'}^N\, R_T(x') + p_{z'}^N\, R_T(z')$$
$$\tilde{R}_{TT'}^{(II)} \equiv \tilde{R}_{TT'}^{(II)}(p_{x'}^N, p_{z'}^N) = p_{x'}^N\, R_{TT}(x') + p_{z'}^N\, R_{TT}(z') \tag{116}$$

where the coordinate system, shown in Fig. 27 (a simplified and relabeled version of that given in Fig. 24) is constructed from the incident photon direction $\hat{k} \equiv \hat{z}$ and the outgoing proton direction $\hat{p} \equiv \hat{z}'$. Substituting the expansions (116) into the cross section formula (109), gives, in a notation suggested by Ref. [170],

$$\frac{d\sigma}{d\Omega} = \left(\frac{d\sigma}{d\Omega}\right)_0 \left[1 + p_y^N p_y + p_y^d\, T - p_\gamma(\Sigma + p_y T_1)\cos 2\phi \right.$$
$$\left. + p_+(C_{x'}p_{x'} + C_{z'}p_{z'}) + p_\gamma(O_{x'}p_{x'} + O_{z'}p_{z'})\sin 2\phi\right] \tag{117}$$

where $(d\sigma/d\Omega)_0$ is the differential cross section for unpolarized photons, and explicit expressions for the asymmetry parameters are given in Table 8. Note that the observables C_x and p_y are the real and imaginary parts of the same combination of amplitudes, so that an experimental measurement of both of these observables will fully determine this linear combination of amplitudes.¶ This is not true for any other pair of observables shown in the table. In the c.m. system

$$\left(\frac{d\sigma}{d\Omega}\right)_0 = \frac{e^2\, p_1}{8\nu_0 W}\, R_T = \frac{\alpha\, p_1}{192\pi E_1^2 \nu_0}\, f(\theta) \tag{118}$$

where

$$f(\theta) = \sum_1^6 \left[|F_{i+}|^2 + |F_{i-}|^2\right] . \tag{119}$$

The Fs are defined in Table 9

The *single* polarization observables are the induced proton polarization p_y, the linearly polarized photon asymmetry Σ, and the vector polarized (along $\hat{y}$) target asymmetry T. The quantities p_y and Σ are defined by

$$p_y = \frac{1}{p_y^N}\left(\frac{d\sigma/d\Omega_+ - d\sigma/d\Omega_-}{d\sigma/d\Omega_+ + d\sigma/d\Omega_-}\right) \qquad \Sigma = \frac{1}{p_\gamma}\left(\frac{d\sigma/d\Omega_\perp - d\sigma/d\Omega_\|}{d\sigma/d\Omega_\perp + d\sigma/d\Omega_\|}\right) \tag{120}$$

where $\pm$ refers to $p_y = \pm 1$, and in the expression for Σ the photon is polarized either in plane along the $\hat{x}$ direction ($\phi=0$, denoted $\|$) or out of plane along the $\hat{y}$ direction ($\phi = \pi/2$, denoted $\perp$). Note that the opposite phase convention for Σ ($\sigma_\| - \sigma_\perp$) is often used, and is used in the figures below. The *double* polarization transfer observables

¶ Some references, such as [170], use P_y for the induced polarization instead of p_y.
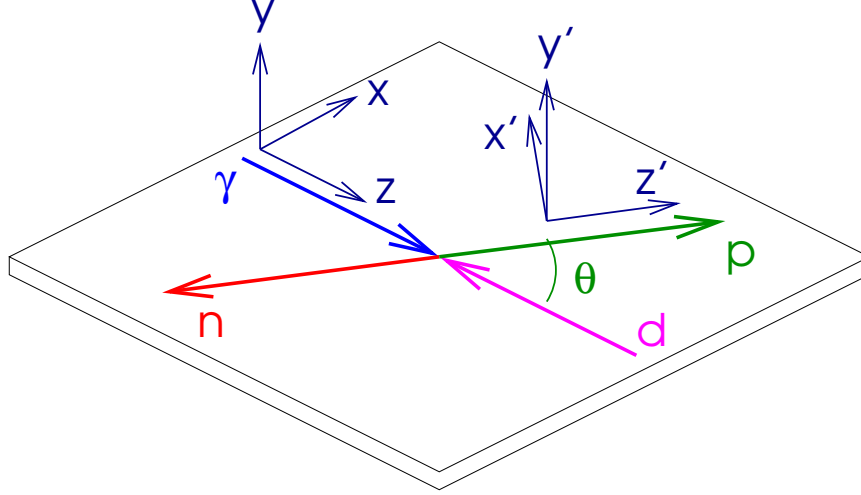
Figure 27. The cordinate system for deuteron photodisintegration. The $\hat{y} = \hat{y}'$ axis is given by $\hat{y} = \hat{k} \times \hat{p}/|\hat{k} \times \hat{p}|$, and the $\hat{x}$, $\hat{x}'$ axes are chosen to make a right handed coordinate system.

Table 8. Formulae for polarization observables. Each structure function in the second column is to be divided by R_T, and in the third column by $f(\theta)$. [The $F_{i\pm}$ are defined in Table 9.]

Observable	Structure function	Helicity amplitude combination
p_y	$R_T(y)$	$2\mathrm{Im}\sum_{i=1}^{3}\left[F_{i+}^*\,F_{(i+3)-} + F_{i-}\,F_{(i+3)+}^*\right]$
T	$R_T(\mathrm{Im}T_{11})$	$2\mathrm{Im}\sum_{i=1}^{2}\sum_{j=0}^{1}\left[F_{(i+3j)+}\,F_{(i+3j+1)+}^* + F_{(i+3j)-}\,F_{(i+3j+1)-}^*\right]$
Σ	R_{TT}	$2\mathrm{Re}\sum_{i=1}^{3}(-)^i\left[-F_{i+}\,F_{(4-i)-}^* + F_{(3+i)+}\,F_{(7-i)-}^*\right]$
T_1	$R_{TT}(y)$	$2\mathrm{Im}\sum_{i=1}^{3}(-)^i\left[-F_{i+}F_{(7-i)+}^* + F_{i-}F_{(7-i)-}^*\right]$
$C_{x'}$	$R_T(x')$	$2\mathrm{Re}\sum_{i=1}^{3}\left[F_{i+}^*\,F_{(i+3)-} + F_{i-}\,F_{(i+3)+}^*\right]$
$C_{z'}$	$R_T(z')$	$\sum_{i=1}^{6}\left\{|F_{i+}|^2 - |F_{i-}|^2\right\}$
$O_{x'}$	$R_{TT}(x')$	$2\mathrm{Im}\sum_{i=1}^{3}(-)^{i+1}\left[F_{i+}F_{(7-i)+}^* + F_{i-}F_{(7-i)-}^*\right]$
$O_{z'}$	$R_{TT}(z')$	$2\mathrm{Im}\sum_{i=1}^{3}(-)^{i+1}\left[F_{i+}\,F_{(4-i)-}^* + F_{(3+i)+}\,F_{(7-i)-}^*\right]$

are T_1 and $O_{x',z'}$ (for linearly polarized photons), and $C_{x',z'}$ (for circularly polarized photons), with the subscripts on O and C giving the polarization direction in the final state.

5.4. Theory

5.4.1. Models using meson-baryon degrees of freedom

There have been many attempts to understand low energy deuteron photodisintegration using a conventional meson-baryon framework. Since the first band of nucleon resonances is not excited until about

Table 9. The relations between the helicity amplitudes used in Refs. [140] and [170].

Amplitude	Ref. [140]	Ref. [170]
$\left\langle \pm\frac{1}{2} \pm \frac{1}{2} \mid J \cdot \epsilon_+ \mid 1 \right\rangle$	$F_{1,2}$	$F_{1\pm}/2m$
$\left\langle \pm\frac{1}{2} \pm \frac{1}{2} \mid J \cdot \epsilon_+ \mid 0 \right\rangle$	$F_{3,4}$	$F_{2\pm}/2m$
$\left\langle \pm\frac{1}{2} \pm \frac{1}{2} \mid J \cdot \epsilon_+ \mid -1 \right\rangle$	$F_{5,6}$	$F_{3\pm}/2m$
$\left\langle \pm\frac{1}{2} \mp \frac{1}{2} \mid J \cdot \epsilon_+ \mid 1 \right\rangle$	$F_{7,8}$	$F_{4\pm}/2m$
$\left\langle \pm\frac{1}{2} \mp \frac{1}{2} \mid J \cdot \epsilon_+ \mid 0 \right\rangle$	$F_{9,10}$	$F_{5\pm}/2m$
$\left\langle \pm\frac{1}{2} \mp \frac{1}{2} \mid J \cdot \epsilon_+ \mid -1 \right\rangle$	$F_{11,12}$	$F_{6\pm}/2m$

400 MeV photon energy (recall Fig. 26) it makes sense to describe the process below 400 MeV using a model of coupled NN, $N\Delta$ and $NN\pi$ channels. Laget [171] showed that the prominant shoulder in the total cross section at $E_\gamma = 300$ MeV can be largely explained by the mechanism in which a Δ is photoproduced at a nucleon followed by the reabsorption of its decaying pion by the other nucleon. He also examined many other mechanisms, including rescattering up to second order, but did not do a full calculation of the final-state interaction. Later Leideman and Arenhövel [172] treated the NN, $N\Delta$ and $\Delta\Delta$ as coupled channels and included final-state effects to all orders. Tanabe and Ohta [173] followed with a more complete treatment of the final state which is consistent with three-body unitarity. In a number of conference talks, Lee [174] reported on coupled channel calculations using N, Δ and the $P_{11}(1440)$ (Roper) resonances, which he extended to $E_\gamma = 2$ GeV. His work suggests that final-state interactions significantly enhance the cross section for photon energies above 1 GeV.

The recent calculations by Schwamb and Arenhövel and collaborators [175] include the NN, $N\Delta$ and πd channels, and also contributions from meson retardation, meson exchange currents, and the meson dressing of the nucleon lines required by unitarity. All parameters are fixed from nucleon-nucleon scattering and photoreactions such as Δ excitation from the nucleon, so no new parameters are introduced into the calculations of the deuteron photodisintegration process itself. They obtain a reasonable description of NN scattering up to lab energies of 800 MeV, particularly for the important $^1D_2$ partial wave, and emphasize that the consistent inclusion of retardation effects improves their results for photodisintegration. In another work it was shown that inclusion of the S_{11} and D_{13} resonances [176] seems to have only a small effect below about 400 MeV. These resonances enhance the total cross section by only 14% at 680 MeV, although effects on double polarization observables can be more significant. Hence there is some justification to limiting the theory of low energy photodisintegration to the channels considered in Ref. [175].

By comparison to the detailed and careful treatments developed for lower energies, calculations specifically designed to describe higher energy photodisintegration are less complete. An unpublished Bonn calculation [177] includes pole diagrams generated from π, ρ, η, and ω exchange, plus the 17 well-established nucleon and Δ resonances with mass less than 2 GeV and $J \leq 5/2$ (listed in Table 6). The calculation uses

resonance parameters taken from the Particle Data Group. Nagornyi and collaborators [178, 179] have introduced a covariant model based on the sum of pole diagrams. The latest version [179] gives the photodisintegration amplitude as a sum of contributions from only 4 Feynman diagrams: three pole diagrams coming from the coupling of the photon to the three external legs of covariant *dnp* vertex plus a contact interaction designed to maintain gauge invariance. This model divides the *dnp* vertex into "soft" and "hard" parts, with the hard part designed to reproduce the pQCD counting rules and its strength determined by a fit to the data at 1 GeV. The model has no final-state interactions or explicit nucleon resonance contributions. There is also a relativistic calculation of photodisintgration in Born approximation using the Bethe-Salpeter formalism [180, 181]. It is found that the cross section is a factor of 2 to 10 times too small, and that relativistic effects are large. All of these models are rather crude, and taken together it is not clear what one should conclude from them. The calculations each appear to emphasize some aspects of what a comprehensive meson-baryon theory of photodisintegration should entail. Perhaps we can say that conventional calculations that neglect final-state interactions seriously underestimate the cross section, but may be corrected in an approximate manner by introducing diagrams with poles in the *s* channel. S-channel pole diagrams can be regarded as a crude approximation to the missing final-state interactions. More generally, using pole diagrams with form factors that have the correct behavior at high momentum transfer may also insure that meson-baryon theories of deuteron photodisintegration will also have the correct high energy behavior [182].

5.4.2. Models based on quark degrees of freedom Perturbative QCD, discussed briefly in Sec. 3.7.2, provides explicit, testable predictions for the cross section and polarization observables. For the case of elastic scattering, the high energy (virtual) photon had to share its mommentum equally with all of the constitutents, leading to the typical diagram shown in Fig. 18. Photo (or electro) disintegration differs in that the momentum will not be distributed to *all* six quarks unless momentum is transferred to *each* nucleon, and this requires non-forward scattering, i.e. the angle $\theta_{\rm cm}$ between the three-momentum of the outgoing proton and the photon (in the c.m. system) must not be 0 or π. More precisely, if E_γ is the energy of the photon in the lab system, the square of the momentum transferred to each nucleon t_i (where $i = 1,2$) can be written

$$t_1 \equiv t = (q - p_1)^2 = m^2 - m_d E_\gamma \left(1 - \sqrt{1 - \frac{4m^2}{s}} \cos \theta_{\rm cm} \right) \rightarrow -s \, \sin^2 \tfrac{1}{2}\theta_{\rm cm}$$

$$t_2 \equiv u = (q - p_2)^2 = m^2 - m_d E_\gamma \left(1 + \sqrt{1 - \frac{4m^2}{s}} \cos \theta_{\rm cm} \right) \rightarrow -s \, \cos^2 \tfrac{1}{2}\theta_{\rm cm} \,, \qquad (121)$$

where s, the square of the c.m. energy, is

$$s = (d + q)^2 = m_d^2 + 2m_d E_\gamma \,, \qquad (122)$$
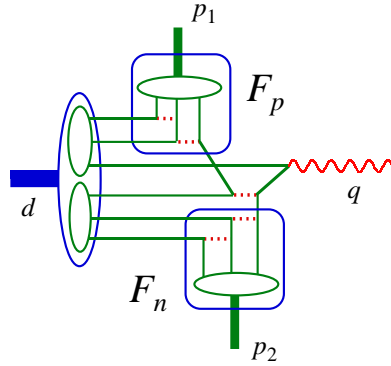
Figure 28. A "typical" pQCD diagram describing large angle photodisintegration. There are 5 hard gluons. The RNA model places the hard gluons in the rectangular boxes within nucleon form factors.

and the limits in (121) are the result for $E_\gamma \gg m_d$. If $\theta_{\rm cm} = 90°$ the momentum transferred to each nucleon is balanced and the pQCD result is reached most rapidly. A "typical" pQCD diagram leading to large angle scattering is illustrated in Fig. 28. In general we cannot expect the cross section to follow pQCD unless the minimum of the two momentum transfers t_1 and t_2 is larger than some value $t_{\rm min}$ at which pQCD holds.

If the above conditions are satisfied, then the cross section and polarization observables should satisfy results predicted by pQCD: the constituent counting rules (CCR) and hadron helicity conservation (HHC).

The CCR [117, 183] predicts the energy dependence of scattering cross sections at fixed center of mass angle

$$\frac{d\sigma}{dt} = \frac{1}{t^{n-2}} f(\theta_{\rm cm}) , \tag{123}$$

where n is the total number of pointlike particles in the initial and final states of the reaction. For deuteron photodisintegration, $n = 13$ (there is one photon and 6+6=12 quarks), and because of Eq. (121) t may be replaced by s, as is commonly done. For elastic ed scattering $n = 14$ because there are electrons in both the initial and final state, and $t = Q^2$, the momentum transfered by the electron. In this case $dt \sim Q^2 d\Omega$, and recalling Eq. (23) we have

$$\frac{1}{Q^2} \frac{d\sigma}{d\Omega} \sim \frac{g(\theta)}{Q^4} A(Q^2) \sim f(\theta) \left(\frac{1}{Q^2}\right)^{12} , \tag{124}$$

recovering the pQCD prediction $A \sim Q^{-20}$.

The second rule from pQCD is that the total helicity of the incoming and outgoing hadrons should be conserved [118]

$$\sum_i \lambda_i = \sum_f \lambda_f , \tag{125}$$

where λ_i (λ_f) are the helicities of the initial (final) hadrons. In Sec. 3.7.2 we discussed the implication of this rule for the deuteron form factors. HHC makes predictions for

Table 10. Implications of HHC for some polarization observables in $\gamma d \to pn$. The $90°$ limits require additional assumptions.

Observable	HHC limit	Approach to HHC
$d\sigma/d\Omega$	$F_{1+}^2 + F_{3-}^2 + F_{5+}^2 + F_{5-}^2$	t^{-2}
p_y	0	t^{-1}
T	0	t^{-1}
Σ	$2\mathrm{Re}\,(F_{1+}F_{3-}^* + F_{5+}F_{5-}^*)/(d\sigma/d\Omega) \;\to -1$ at $90°$	t^{-2}
T_1	0	t^{-1}
$C_{x'}$	0	t^{-1}
$C_{z'}$	$[F_{1+}^2 - F_{3-}^2 + F_{5+}^2 - F_{5-}^2]/(d\sigma/d\Omega) \;\to 0$ at $90°$	t^{-2}
$O_{x'}$	0	t^{-1}
$O_{z'}$	$-2\mathrm{Im}(F_{1+}F_{3-}^* + F_{5+}F_{5-}^*)/(d\sigma/d\Omega) \;\to 0$ at $90°$	t^{-2}

many spin observables, particularly vector polarizations [184]. Here it predicts that the amplitudes of Table 9 will have the following behavior at large t

$$
\begin{aligned}
&F_{1+},\ F_{3-},\ F_{5\pm} && \text{leading} \\
&F_{2\pm},\ F_{4\pm},\ F_{6\pm} && \text{suppressed by } t^{-1} \\
&F_{1-},\ F_{3+} && \text{suppressed by } t^{-2}
\end{aligned}
\tag{126}
$$

where we have used the fact that each helicity flip is suppressed by a power of t. The implication of HHC for the observables given in Table 8 is summarized in Table 10. The limits at $\theta_{\rm cm} = 90°$ on some of the observables require assumptions about relations between the helicity conserving variables [178, 185].

In an attempt to include some of the soft physics omitted from pQCD, and to extend the region of applicability of pQCD down to lower momentum transfers, Brodsky and Hiller introduced the idea of reduced nuclear amplitudes (RNA) [186]. In this model the gluon exchanges that contribute to identifiable subprocesses (such as nucleon form factors) are collected together and their contributions replaced by experimentally determined nucleon form factors. It is hoped that the resulting expressions will correctly include much of the missing soft physics, and will therefore be valid to lower momentum transfers than the original pQCD expressions from which they were obtained. When applied to deuteron photodisintegration, the cross section is written

$$
\frac{d\sigma}{dt} = \frac{m^2}{24\pi^2(s - m_d^2)^2} \sum |J|^2 \to \frac{1}{(s - m_d^2)^2}\, F_p^2(\hat{t}_p) F_n^2(\hat{t}_n) \frac{1}{p_T^2} f^2(\theta_{\rm cm}) \tag{127}
$$

where the phase space factor of $1/(s - m_d^2)^2$ comes for a careful reduction of the phase space factors in Eqs. (103), (110), and (121) [+], $f(\theta_{\rm cm})$ is the reduced nuclear amplitude, F_p and F_n are the proton and neutron form factors with $\hat{t}_p$ and $\hat{t}_n$ the average momentum transferred to the proton and neutron

$$
\hat{t}_p = (p_1 - d/2)^2 \qquad \hat{t}_n = (p_2 - d/2)^2 \,, \tag{128}
$$

[+] In some experimental fits the phase space factor used is $(s - m_d^2)^{3/2}\sqrt{s - 4m^2}$ instead of $(s - m_d^2)^2$.

and the square of the transverse momentum is

$$p_T^2 = \left(\frac{s}{4} - m^2\right) \sin^2 \theta_{\rm cm} . \tag{129}$$

The power of the "extra" factor of p_T^{-2} is fixed once the phase space and nucleon form factors have been taken into account. Note that this model does not attempt to normalize f.

The RNA form given in Eq. (127) is somewhat arbitrary, particularly in the specification of the form of p_T^2 *. Radyushkin [187] has argued that the elementary process not accounted for by the nucleon form factors (i.e. the absorption of a hard photon followed by exchange of a hard gluon with another quark) should include nonperturbative contributions. The effect is to replace the $1/p_T^2$ factor in Eq. (127) by a smooth function $f^2(s,t)$, which is assumed to vary slowly in energy and angle. In the fits described below, f^2 will be taken to be a constant adjusted to fit the data, implying that $d\sigma/dt \sim s^{-10}$ instead of s^{-11}.

Alternatively, if the quark exchange mechanism shown in Fig. 28 is to be taken seriously, a more detailed calculation is possible. This is the motivation for the work of Frankfurt, Miller, Sargsian, and Strikman [188, 189] where the quark exchange diagram (which the authors refer to as a quark rescattering diagram) is calculated in front-form dynamics using model wave functions for the nucleons and the deuteron. The matrix element is written as a convolution of an elementary quark exchange interaction with the initial and final nucleon wave functions. The final nucleons are free and the distribution of the initial nucleons is given by the deuteron wave function. Since the photon momentum is shared by the proton and neutron, there is little sensitivity to the high momentum part of the deuteron wave function. The elementary interaction is a quark exchange between the two nucleons, with the photon absorbed by one quark which then gives up its momentum through a hard gluon exchange with another quark. The authors show that this can be replaced approximately by the wide angle np scattering cross section (also dominated by quark exchange). The final formula obtained from these arguments is

$$\left.\frac{d\sigma}{dt}\right|_{\gamma d} = \frac{4\alpha\pi^4 m}{9(s - m_d^2)} C\left(\hat{t}_p/s\right) \left.\frac{d\sigma(s, \hat{t}_p)}{dt}\right|_{np} \left| \int \frac{d^2 p_\perp}{(2\pi)^2} \Psi_d(p_z = 0, p_\perp) \right|^2 , \tag{130}$$

where $C(-x) = x/(1-x)$ was used in the fits to the data discussed below. The authors propose using experimental data for the np cross section, but since data does not exist for the actual kinematic conditions needed, it must be extrapolated, and predictions for photodisintegration are given as a band corresponding to the uncertainties introduced by the extrapolations. The authors believe that their predictions should be valid for E_γ > 2.5 GeV, and nucleon momentum transfers $-t = -t_1$ and $-u = -t_2 > 2$ GeV^2.

The high energy approaches described above all focus on the region where both $\hat{t}_p$ and $\hat{t}_p$ are large (where perturbative arguments can serve as the foundation for the

---

* In Ref. [186] it is proposed that $p_T^2 = tu/s$. This choice of p_T leads to an increased energy dependence and worse agreement with the data.

treatment). Alternatively, we may ask what to expect when one of these momentum transfers is small (but s is still large). The authors in Refs. [190, 191] develop a model (which they refer to as the "quark-gluon string model") based on a Reggie generalization of the nucleon exchange Born term. Here the exchanged nucleon is replaced by a nucleon Reggie trajectory that represents the sum of a tower of exchanged nucleon resonances (or the exchange of three quarks dressed by an arbitrary number of gluons). The energy dependence of the predicted cross section is

$$\frac{d\sigma}{dt} \to \left(\frac{s}{s_0}\right)^{2\alpha_N(t)-2} , \tag{131}$$

where $\alpha_N(t)$ is the nucleon Reggie trajectory, with $\alpha_N(t) = -0.5 + 0.9t + 0.25t^2/2$, where t is in units of GeV^2. Recent work [191] emphasizes the importance of the nonlinear term in the Reggie trajectory. The model is intended to work for $E_\gamma > 1$ GeV, with $-t$ less than about 1 GeV^2.

We now turn to a review of the experimental data and to a comparison between theory and experiment.

5.5. Experimental Status

The world data set for cross sections (except for the most recent experiments) has been presented several times [162], and we will not review the normalization problems of older cross section data sets. Table 11 presents an extensive list of the published polarization data. About 70 publications, starting in 1960, present about 1200 data points for photodisintegration and the time reversed radiative capture reaction. Table 11 generally lists photon lab energy and proton c.m. angle (neutron c.m. angle for the p_y^n data). All of the radiative capture experiments have measured A_y^n, and for these experiments we usually give the neutron beam kinetic energy and outging photon c.m. angle; for the IUCF experiment we give their reported proton c.m. angle. Matching c.m. energies leads to $T_n = E_\gamma m_d/m_p + (m_d^2 - (m_n + m_p)^2)/2m_p$ or $T_n \approx 2E_\gamma$ at high energies. Comparison of these data indicates serious problems with backgrounds and/or estimates of systematic uncertainties in a number of cases, as will become clear in figures in the sections below.

We review some of the lower energy data in the next subsection. High energy experiments, with photon energy above ≈ 1 GeV, are covered in the following subsection.

5.5.1. Low energy photodisintegration

In this section we review selected experiments with beam energies from about pion production threshold to several hundred MeV. Tagged photon facilities, with their improved knowledge of incident beam flux, have allowed significantly improved cross section measurements in this region since the 1980s. Of particular note are extensive recent data sets from LEGS and Mainz. Figures 29 and 30 show angular distributions for the cross section, and Σ, T, and p_y at photon energies near 300 and 450 MeV, respectively.

The LEGS tagged, backscattered, and linearly-polarized photon beam was used to determined cross sections and Σ [248, 249, 250]. Five independent measurements

Table 11. Measurements of deuteron photodisintegration polarization observables.

Laboratory	Observable	E (MeV)	$\theta_{\rm cm}(°)$	# of Points	Reference
MIT	p_y	250	49	1	[163]
Livermore	p_y^n	2.75	50 - 136	5	[164]
Zürich	p_y^n	2.75	44, 94	2	[193]
Illinois	p_y^n	12 - 23	148	4	[194]
RPI	p_y^n	12 - 30	90	3	[195]
Purdue	p_y	294	72	1	[196]
Stanford	Σ	80 - 140	45, 90, 135	41	[197, 198]
Livermore	p_y^n	2.75	32 - 152	7	[199]
Frascati	Σ	235 - 404	90	8	[200]
Stanford	p_y	172 - 436	39 - 126	19	[165]
Bonn	p_y	282 - 405	74 - 98	4	[166]
Yale	p_y^n	7 - 30	48, 94	20	[201]
Yale	p_y^n	7 - 13	90	3	[202]
Tokyo	p_y	352 - 697	45 - 133	27	[167, 203, 204, 205]
Kharkov	Σ	80 - 600	75 - 150	109	[206, 207, 208, 209, 210]
Frascati	Σ	10 - 69	90	9	[211, 212]
Kharkov	p_y	375 - 700	43, 78, 90, 120	40	[213, 214, 215]
Kharkov	p_y	550 - 1125	90, 120	30	[216, 217, 218]
Yerevan	Σ	400 - 700	45, 55	5	[219]
Tokyo	T	324 - 672	72, 100, 130	24	[220, 221]
Kharkov	p_y, Σ, T_1	300 - 600	75, 90, 120	22,20,20	[222, 223, 170, 224]
Frascati	Σ	20, 29, 39, 61	14 - 165	41	[225, 226]
Bonn	Σ	233 - 818	114, 135	103	[227]
Argonne	p_y^n	6 - 14	90	6	[228]
Kharkov	Σ	40, 50, 60, 70	75, 90	8	[229]
Bonn	T	450, 550, 650	25 - 155	41	[230, 231]
Yerevan	Σ	395 - 795	45 - 95	30	[232, 233]
TRIUMPF	A_y^n	180, 270	32 - 144	18	[234, 235]
TRIUMPF	A_y^n	370, 478	45 - 155	45	[236]
Tomsk	Σ	50 - 100	45, 60, 90	13	[237, 238]
Wisconsin	A_y^n	6, 13	94	2	[239]
Novosibirsk	T_{21}	33 - 125	50	4	[240]
Yerevan	$O_{x'}^n$	300, 400, 500	130	3	[241]
Kharkov	p_y	200 - 367	25 - 110	30	[242, 243]
Yerevan	p_y, p_{xz}	306 - 436	65, 75	2×8	[244, 245]
Karlsruhe	A_y^n	19 - 50	62, 98, 131	27	[246]
Yerevan	Σ	284 - 999	45, 60, 75, 95	94	[247]
BNL LEGS	Σ	100 - 314	16 - 162	112	[248, 249, 250]
Novosibirsk	T_{20}, T_{22}	49 - 505	88	2×9	[251]
IUCF	C_{nn}, A_y, A_y^n	183	48 - 125	3×6	[252]
PSI	A_y^n	68	69 - 144	5	[253]
Mainz	Σ	160 - 410	35 - 155	140	[254]
Yerevan	Σ	787 - 1566	90	6	[255]
JLab	$p_y, C_{x'}, C_{z'}$	479 - 2411	90	10,9,8	[6]
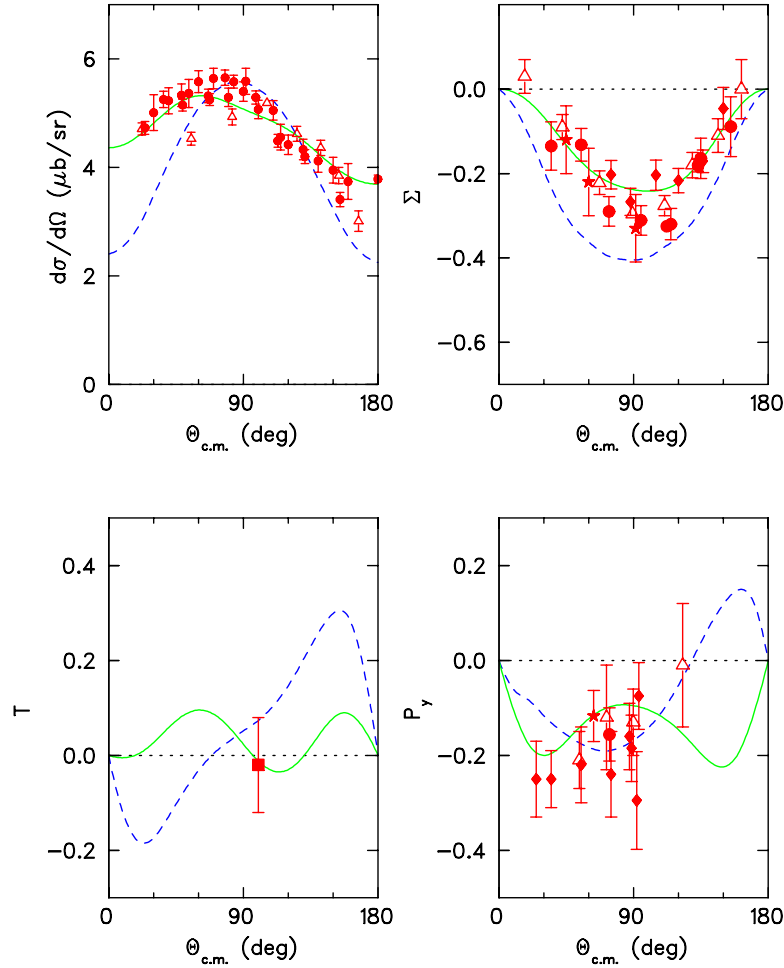
Figure 29. Four observables for $d(\gamma, p)n$ at 300 MeV. Calculations are from Schwamb and Arenhövel (solid line) [175] and Kang, Erbs, Pfeil and Rollnik (dashed line) [177]. The cross section data are from LEGS (triangles) [250] and Mainz [256] plus Bonn [257, 258, 259] (circles). The Σ data are from LEGS (triangles) [250], Mainz (circles) [254], Kharkov (diamonds) [210], and Yerevan (stars) [247]. The T datum is from Tokyo [221]. The p_y data are from Stanford (triangles) [165], Bonn (circle) [166], Yerevan (star) [245], and Kharkov (diamonds) [224, 243]. See Table 11 for related references.

used three detector systems, two targets, and two different laser frequencies. Data were taken for $E_\gamma = 100$ - 315 MeV with eight laboratory angles from 15 - 155°. Cross section statistical uncertainties range from a few percent to about 15%, with systematic uncertainties of 5%. One observation in the LEGS data is of pion contamination that may have been missed in earlier experiments, leading to increased cross sections.

The MAMI Mainz experiment [256] used the Glasgow photon tagger along with the large solid angle detector DAPHNE to determine cross sections in the ranges $E_\gamma = 100$ - 800 MeV and $\theta_{cm} = 30$ - 160°. Data were binned by 20 MeV in energy and 10° in angle. Statistical uncertainties ranged from a few percent at lower energies to about 25% at the highest energies. Systematic errors were also energy dependent, ranging from a few
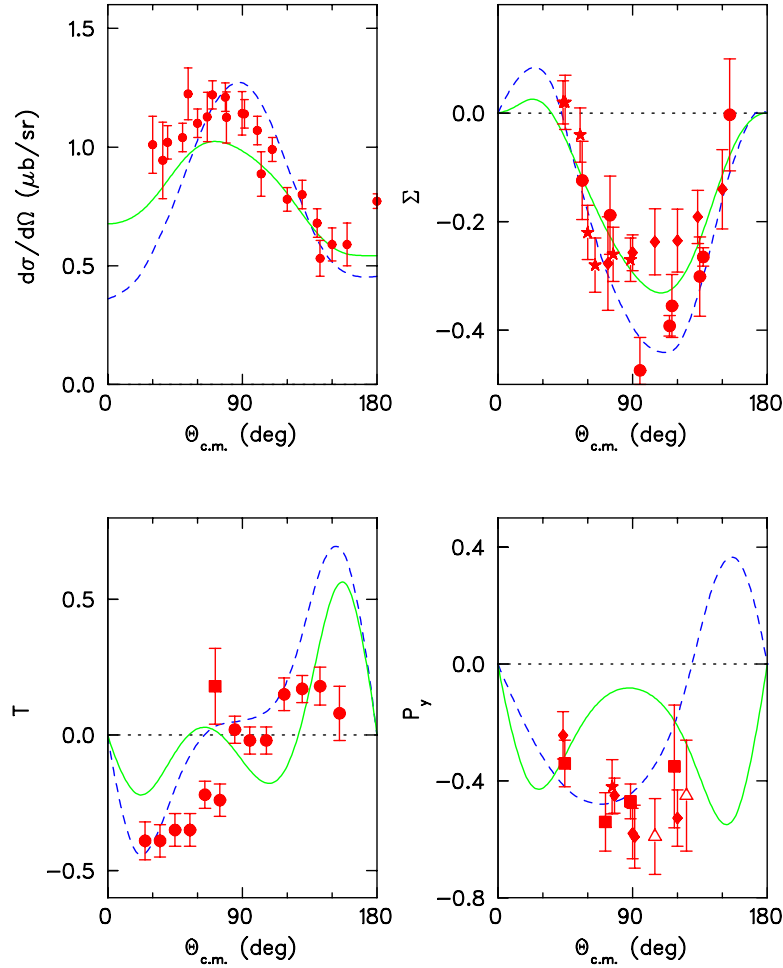
Figure 30. Four observables for $d(\gamma, p)n$ at about 450 MeV (410 MeV for Σ). Calculations are from Schwamb and Arenhövel (solid line) [175] and Kang, Erbs, Pfeil and Rollnik (dashed line) [177]. The cross section data are from Mainz [256] plus Bonn [257, 258]. The Σ data are from Mainz (circles) [254], Kharkov (diamonds) [210], and Yerevan (stars) [247]. The T data are from Tokyo (square) [221] and Bonn (circles) [231]. The p_y data are from Stanford (triangles) [165], Tokyo (squares) [205], Yerevan (star) [245], and Kharkov (diamonds) [215, 224]. See Table 11 for related references.

percent to several percent. The Σ asymmetry [254] was obtained by using a coherent bremsstrahlung radiator.

Agreement between the Mainz and LEGS cross section results is generally better than 10%. The Σ asymmetries also agree well with each other and with earlier results from Yerevan [247]. Measurements from Kharkov [206, 207, 209, 210] generally agree, except for a tendency to be slightly smaller at many beam energies.

The vector polarized target asymmetry T was measured at Tokyo [220, 221] and at Bonn [230, 231]. The two measurements generally agree, with the data appearing to follow, very roughly, a $-\sin\theta$ dependence at each energy, as do the calculations of [177].

The induced polarization p_y has been measured at a number of laboraties, with significant amounts of lower energy data from Stanford [165], Tokyo [167, 203, 204,

205], and Kharkov. There were several experiments at Kharkov, including initial measurements [213, 214, 215], high-energy measurements [216, 217, 218], simultaneous measurements of Σ, T_1, and p_y [222, 223, 170, 224], and lower-energy measurements [242, 243]. The Kharkov data do not have a desirable level of consistency. The simultaneous measurements of Σ, T_1, and p_y were taken as single-arm data, away from the photon endpoint, and may suffer from backgrounds. Polarizations below about 300 MeV, including the intermediate energy neutron measurements [234, 235, 236], appear to be well reproduced by theories. There are numerous data, particularly at $\theta_{\rm cm} = 45°$, 78°, 90°, and 120°, but there are few energies at which there are good angular distributions. The conclusion that polarizations are large, close to -1, and peak at about 500 MeV near 90° is beyond dispute.

Figures 29 and 30 show the good agreement of the recent Mainz [175] and older Bonn [177] calculations with the cross section and Σ asymmetry. Theory seems to agree with $d\sigma/d\Omega_{\parallel}$ better than $d\sigma/d\Omega_{\perp}$ [249]. The agreement is better at the lower energy, and the newer Mainz calculation is generally in better agreement. However, there is difficulty, particularly at the higher energy, with T and p_y, both imaginary parts of the interference of amplitudes. The large induced polarizations above the Δ resonance have remained a puzzle for almost 30 years, and are still not fully explained by the newest theories. The Bonn calculation was in sufficiently good qualitative agreement with all observables ($d\sigma/d\Omega$, Σ, T, *and* p_y) for energies up several hundred MeV for the authors to consider this p_y puzzle solved. However, detailed examination of Fig. 30 shows that neither the shape nor strength of the angular distribution is accurately reproduced; this will become clearer when we examine the energy dependence of p_y at $\theta_{\rm cm} = 90°$ below.

5.5.2. High energy photodisintegration Figure 31 shows the published high energy photodisintegration data, from experiments NE8 [262, 263] and NE17 [264] at SLAC, and E89-012 [5] and E96-003 [7] at JLab. These experiments determine cross sections for $\theta_{\rm cm} \approx 36°$, 52°, 69°,and 89° at energies from about 0.7 to 5.5 GeV; there are also some backward angle data up to 1.8 GeV from NE8. These data overlap well; the experiments, while all run by essentially the same collaboration, used three spectrometers in two experimental halls at two laboratories. There is also good overlap, variations of less than about 20%, with the highest energy Mainz tagged photon data [256], and with older untagged data [257, 259, 265, 266, 267].

Tagged photon measurements at low energies provide an accurate measure of beam flux, and along with the measured proton angle and energy, can determine a missing mass that allows background rejection. At high energies, smaller cross sections cannot be determined with the reduced flux of tagged photons. The Bremstrahlung endpoint technique was used for all of the SLAC and JLab measurements shown in Fig. 31.

In the endpoint technique, the measured proton momentum vector determines the incident photon energy and neutron kinematics, *assuming* the reaction is two body photodisintegration. Low momentum protons are cut from the analysis to prevent contamination from final states such as $pn\pi^0$, while high momentum protons are cut
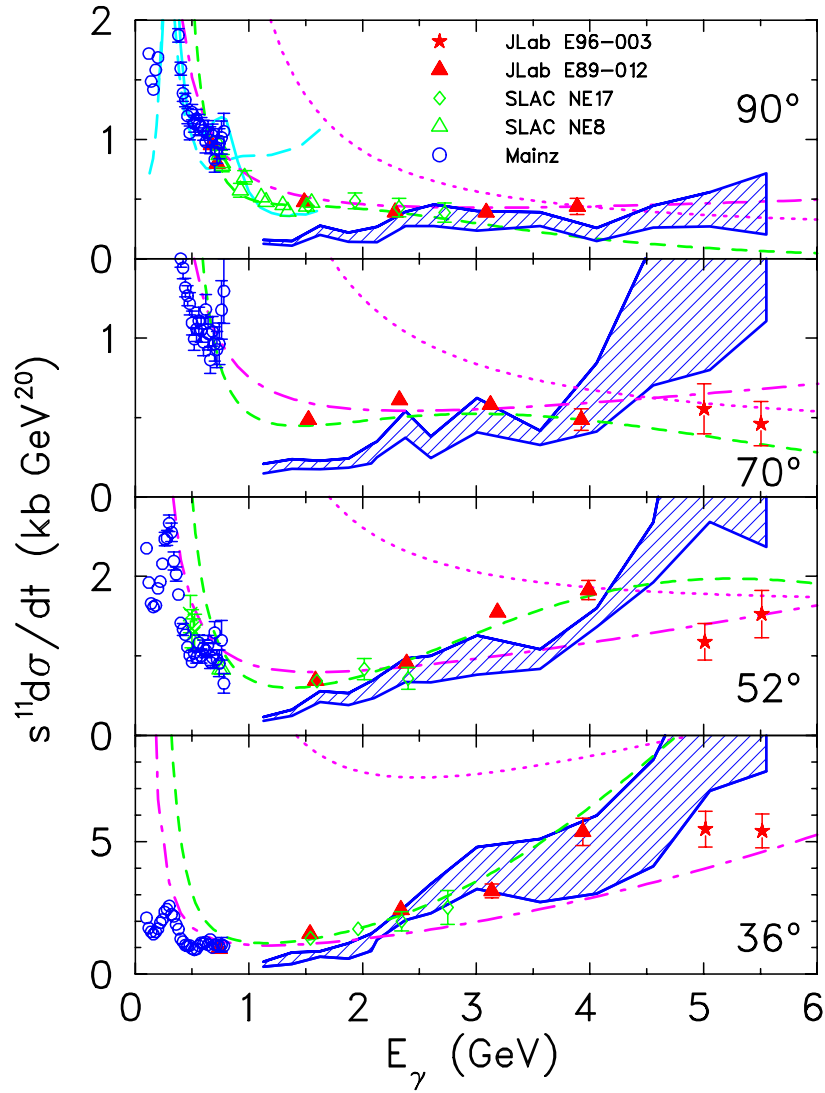
Figure 31. Photodisintegration cross section $s^{11}d\sigma/dt$ versus incident lab photon energy. The calculations are from Kang, Erbs, Pfeil and Rollnik (solid line; 90° low energy data only) [177], Lee (long dashed line; 90° low energy data only) [174], Raydushkin (dot-dashed line) [187], RNA of Brodsky and Hiller (dotted) [186], quark qluon string model (short dashed) [190, 191], and Frankfurt, Miller, Strikman and Sargsian (shaded region) [188, 189].

to eliminate the larger uncertainty in the photon flux close to the photon endpoint. Backgrounds are determined by radiator out and empty target measurements, and subtracted. Events in the region beyond the endpoint can be used to check the subtraction. The increase in time required for this subtraction makes it prohibitive for the highest energy measurements; for these the electrodisintegration background is calculated [260] and subtracted. To determine the cross section, the incident photon flux is calculated using the method of Ref. [261]. Thick radiator corrections are typically about 15% for a radiator thickness of 6% of a radiation length.

The main feature of the cross section data above about 1 GeV is the s^{-11} (s^{-10}) fall off of the cross sections $d\sigma/dt$ ($d\sigma/d\Omega$) at $\theta_{cm} = 90°$ and $69°$, in agreement with the CCR and thus with perturbative QCD expectations. In contrast, the cross sections at the forward angles $36°$ and $52°$ fall off more slowly, with approximate s^{-9} scaling at lower energies until the onset of the s^{-11} behavior at about 4 and 3 GeV beam energy, respectively. At each angle, the onset of the s^{-11} behavior corresponds to $p_T \approx 1$ GeV.

The RNA and the Radyushkin estimates in Fig. 31 were normalized to the datum at $89°$ and $E_\gamma = 4$ GeV, fixing their one free parameter. The RNA is then almost a factor of 2 too large at $36°$, and also much too large at lower energies, requiring that the soft physics missing from the RNA interfere *destructively* with the leading terms. Suggested angular dependences of $f(\theta_{cm})$ [186] would increase the RNA curve further at the forward angles, worsening agreeement with the data. In contrast, the Radyushkin estimate gives a somewhat better account of both the angular and energy dependence (even though it only goes asympotically as s^{-10}), confirming that phase space and nucleon form factors are all that is needed to account for much of the kinematic variation of the cross section. While the apparent onset of scaling at the forward angles suggests this agreement is starting to break down, we conclude the present data are insufficient to uniquely fix the asymptotic energy dependence of the cross section.

The cross section data are also reasonably well reproduced by the model of Frankfurt, Miller, Strikman and Sargsian [FMSS] [188, 189] and the quark gluon string (QGS) model [190, 191]. The predictions of FMSS are uncertain because (a) the high energy NN scattering data has an uncertain energy dependence reflecting the experimental errors, and (b) the extrapolation of the NN data required for the predictions introduces further errors. These two uncertainties combine to give the jagged region shown in Fig. 31. The QGS model describes the forward angle data up to 4 GeV reasonably well, even for values of $-t$ exceeding the nominal limits of the model. The newer work [191] predicts that the angular distributions will become increasingly symmetric at higher energies; older estimates [190] had predicted an increasing *asymmetry*.

Two experiments currently have unpublished data for cross sections at photon energies up to 2.5 GeV. JLab Hall B E93-017 [268] used the CLAS with tagged photons to determine nearly complete angular distributions. The preliminary data agree well with earlier measurements, but are much more comprehensive than previous measurements in this energy range. Hall A E99-008 [269] has taken angular distributions at eight angles with $\theta_{cm} = 30° - 143°$, at energies of 1.67, 1.95, and 2.50 GeV. Fig. 32 shows a sample angular distribution at approximately 1.6 GeV.

5.5.3. Polarization observables in high energy photodisintegration   There are only three sets of polarization data for deuteron photodisintegration at energies near and above 1 GeV. The induced polarization p_y was measured at Kharkov [216, 217, 218], the Σ asymmetry was measured at Yerevan [247, 255], and p_y and the polarization transfers $C_{x'}$ and $C_{z'}$ were measured at JLab [6]. Data for the energy dependence of these four
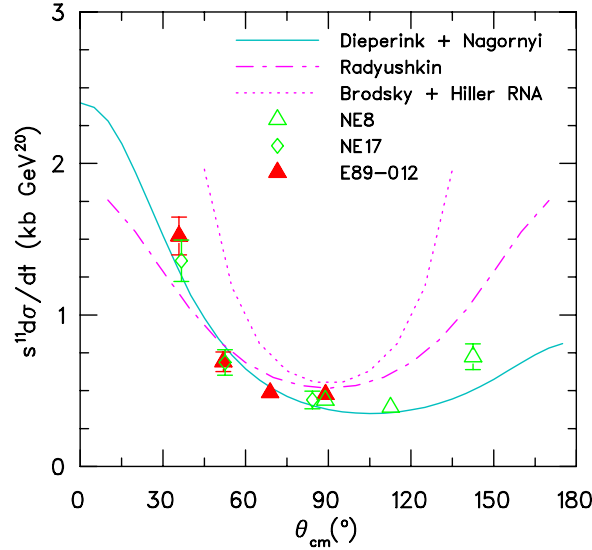
Figure 32. Deuteron photdisintegration angular distribution at $E_\gamma \approx 1.6$ GeV. Data are from SLAC experiments NE8 [262, 263] and NE17 [264], and JLab experiment E89-012 [5]. Calculations are from Dieperink and Nagornyi [179], Radyushkin [187], and the RNA of Brodsky and Hiller [186]. The Radyushkin curve has been normalized to the 4 GeV 90° datum, as in Fig. 31, while the RNA curve has been reduced 60% from that normalization to better agree with this data.

observables at a fixed $\theta_{\rm cm} = 90°$ are compared with theory in Figs. 33, 34, and 35.

The Kharkov measurements of p_y at $\theta_{\rm cm} = 90°$ and $120°$ extend up to about 1.1 GeV (see Fig. 33). These experiments were very difficult. The small duty factor at Kharkov increases instantaneous background rates a factor of about 20,000 over those at JLab. These large backgrounds made it necessary to use multiple spark chambers to track particle trajectories. It was also difficult to calibrate the polarimeter. Calibrations of a polarimeter are best done by measuring its analyzing power using the known $\vec{e}p \to e'\vec{p}$ elastic scattering reaction [6, 46, 47], but Kharkov had no polarized beam. The Kharkov measurements relied on a single elastic ep point to check false asymmetries in their polarimeter, and used analyzing powers from the literature. Finally, the polarimeter had a rear trigger scintillator; any inefficiencies in the scintillator would lead to false asymmetries. In contrast, the recent JLab experiment [6] had little background, used $\vec{e}p \to e'\vec{p}$ calibrations to determine false asymmetries and analyzing powers at each kinematic setting, and had no rear trigger scintillator. Given the clear disagreement of the Kharkov data with the recent JLab data, and noting that one of us (RG) is a spokesperson of the JLab experiment, we conclude that the highest energy set of Karkov data should not be trusted.

The induced polarizations shown in Fig. 33 confirm our comments above concerning the Bonn calculation. The large negative polarization near 500 MeV is not reproduced, and the calculation is qualitatively incorrect at higher energies. The imaginary part of the amplitude appears to be a problem in these meson-baryon calculations; presumably
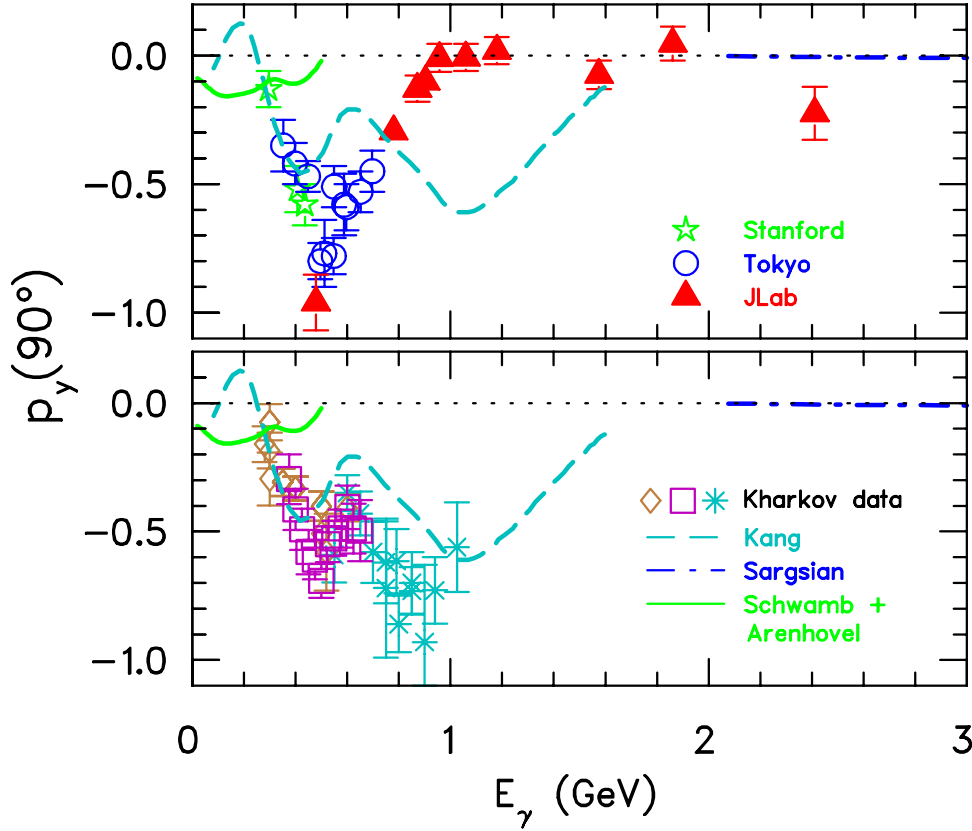
Figure 33. Induced polarization p_y for photodisintegration at $\theta_{cm} = 90°$. Data sets from Stanford [165], Tokyo [205], and JLab [6], are in the top panel. Data sets from Kharkov (squares) [215], (stars) [218], and (diamonds) [224] are in the lower panel. See Table 11 for related references. The calculations are from Kang, Erbs, Pfeil and Rollnik (dash line) [177], Sargsian (dash dot line) [270] and from Schwamb and Arenhövel (solid line) [175].

this arises from an inadequate treatment of resonances.

Taken together, these recoil polarization data only weakly confirm the predictions of HHC, which predicts that p_y and $C_{x'}$ should approach zero as $s \to \infty$, and that (with additional assumptions [178, 185] about relations between the helicity conserving amplitudes at $\theta_{cm} = 90°$) $\Sigma \to -1$ and $C_{z'} \to 0$ as $s \to \infty$. The highest energy polarization measurements of p_y show that it is consistent with vanishing at energies above about 1 GeV, the same energy at which the s^{-11} cross section scaling begins. [In the Radyushkin model p_y should be zero because the amplitudes are all real if there is no gluon exchange [271].] Similarly, the polarization transfer observables $C_{x'}$ and $C_{z'}$ both appear to peak near 1 GeV, and decrease at higher energies. However, $C_{x'}$ does not appear to vanish sufficiently rapidly; the data might be inconsistent with HHC. So p_y and $C_{z'}$ (and perhaps $C_{x'}$) seem to have close to the correct behavior, but Σ does not. The highest energy Σ asymmetry measurements from Yerevan, with data up to about 1.6 GeV, give the immediate impression that there is a minimum near 1.2 GeV and that above this energy the asymmetry is tending to increase towards 1, although
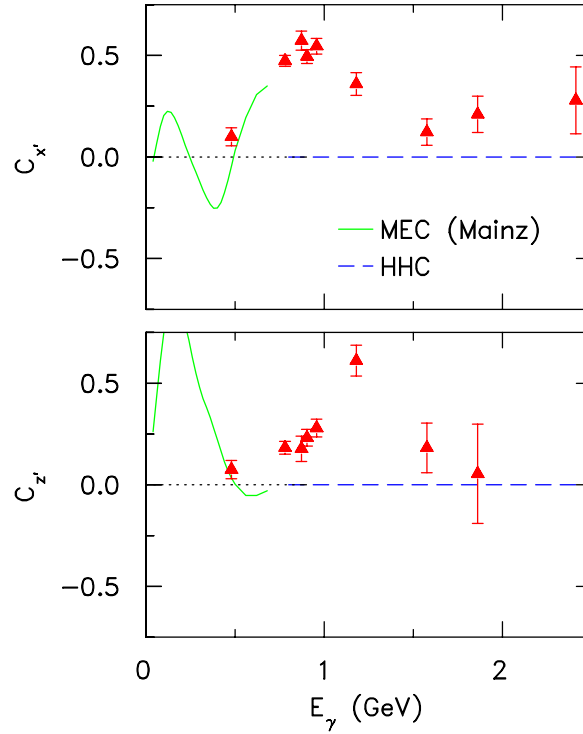
Figure 34. Polarization transfer for deuteron photodisintegration at $\theta_{cm} = 90°$. The data are from Ref. [6]. The calculation is from Schwamb and Arenhövel [175]. HHC (with some additional assumptions for $C_{z'}$) predicts that both of these amplitudes should vanish as $s \to \infty$.

the data are also statistically consistent with a constant value of about 0.3. In either case the trend is clearly not consistent with $\Sigma \to -1$.

In models based on meson-baryon degrees of freedom, the data indicate that the combined effects of resonances plus final-state interactions are small. Calculations of p_y in meson baryon theories [171, 172, 173, 176, 177] indicate that p_y at higher energies arises largely from resonance - background interference, with a small contribution from final-state interactions. Calculations generally indicate that the Δ resonance generates a large polarization, though only perhaps about 50% of the magnitude seen in the experimental data at $\theta_{cm} = 90°$. The Roper and S_{11} have small effects, while the D_{13} has a large effect [176, 177]. The D_{33}, included only by the Bonn group [177], also generates a large polarization. (Of the 17 resonances included in the Bonn calculation [177], only those mentioned above had large effects on p_y.) As discussed above, it is hard to imagine that a theoretically acceptable high energy model based on hadronic degrees of freedom will be constructed in the near future. Still, a modern relativistic calculation based on hadronic degrees of freedom would nonetheless be desirable.

A calculation of p_y has been done in the model of FMSS [270]. Since the helicity amplitudes in the nucleon-nucleon scattering for this center of mass energy range are not uniquely determined, some modelling was needed. The calculation showns that p_y is generally very small, going from a negative value at low energies to positive values at several GeV beam energy, and is consistent with the trend of the experimental results.
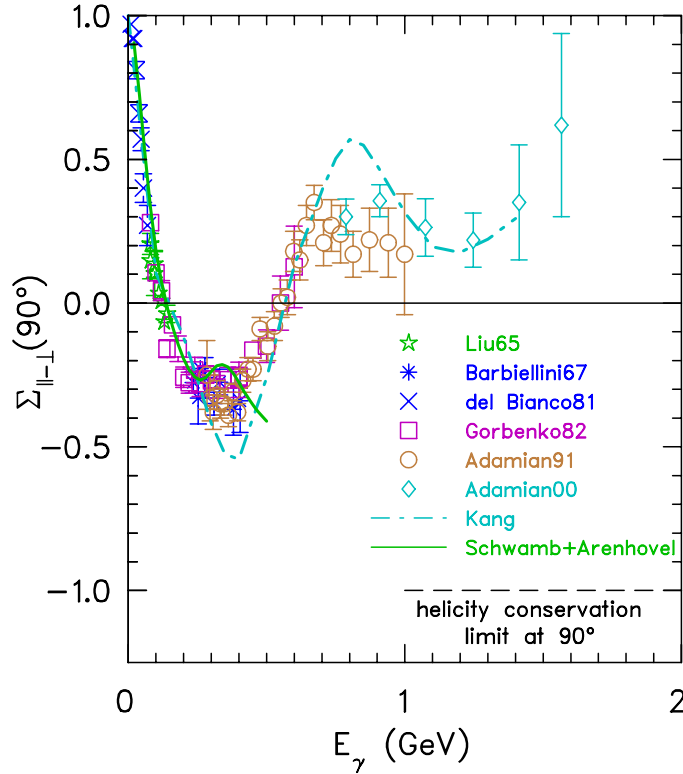
Figure 35. Polarized photon asymmetry Σ at $\theta_{\mathrm{cm}} = 90°$. The calculations are from Kang, Erbs, Pfeil and Rollnik (dot-dashed line) [177] and from Schwamb and Arenhövel (solid line) [175]. The data are from Liu65 [198], Barbiellini67 [200], del Bianco81 [212], Gorbenko82 [210], Adamian91 [247], and Adamian00 [255]. See Table 11 for related references.

The polarization observable C_x is also expected to be small, and opposite in sign to p_y, while C_z is expected to vanish.

5.6. Future prospects

The rapid falloff of photodisintegration cross sections with energy makes extension of the measurements difficult. As beam energy increases from 4 to 5, 6, and 7 GeV, the s^{-11} dependence reduces cross sections by factors of 6, 30, and 115, respectively. Only a few experiments are possible without the proposed 12 GeV upgrade to JLab. As indicated in Table 1, there are two approved experiments to continue the Hall A recoil polarization measurements to additional angles, and to beam energies near 3 GeV. Measurements of the Σ asymmetry are possible in JLab Hall B, over a range of angles and energies well over 1 GeV.

In the longer term, the JLab 12 GeV upgrade offers additional possibilities. The luminosity increase planned for Hall B would allow precise polarization measurements to continue above 2 GeV. The proposed MAD spectrometer for Hall A [272] would give about a factor of 5 improvement in solid angle, and if it has the low backgrounds

characteristic of the current HRS spectrometers, cross section measurements are possible up to 7 GeV and polarization measurements are possible up to 4 GeV.

5.7. Conclusions to Sec. 5

Review of deuteron photodisintegration suggests the following:

- A microscopic meson-baryon theory of deuteron photodisintegration must describe the NN interaction at high energies, including pion production and the contributions of hundreds of N^* channels. It is unlikely that such a theory will be constructed in the foreseeable future. The data might indicate that the effect of many resonances is to increase the cross section and decrease the polarization observables (by averaging over may phases). This suggests that it might be possible to construct an effective theory based on hadronic degrees of freedom.

- For p_T^2 greater than about 1 GeV^2, cross sections appear to follow the constituent counting rules, but it is expected that an absolute pQCD calculation of the size of the cross section would give a result much too small. Similar observations may be made for other photoreactions, and it remains to be seen how this behavior arises, and if there is a general explanation for it.

- The energy dependence of the photodisintegration cross sections has been shown to be potentially misleading indicator of the success of pQCD. Models with asymptotic behavior which differ from pQCD fit the data as well or better than pQCD. Further theoretical development and experimental tests of nonperturbative quark models would be desirable.

6. Overall Conclusions

The new high energy measurements of the deuteron form factors and the deuteron photodisintegration observables have motivated much theoretical work. In particular:

- Conventional meson theory works well in cases where all of the *active* hadronic channels that can contribute to a process are included in the calculations. This has been done for the deuteron form factors (where only the NN channel is active), but not for high energy deuteron photodisintegration where 100's of N^*N^* channels are active. At high energy any successful meson theory must include relativistic effects.

- New approaches, probably using quark degrees of freedom, are needed for high energy deuteron photodisintegration. While photodisintegration (as well as other reactions) seem to follow the scaling laws, theoretical estimates using pQCD give cross sections orders of magnitude too small. The data do not support hadronic helicity conservation. Thus scaling is no longer seen as sufficient evidence for the applicability of pQCD.

There is good evidence that, in this energy region, the deuteron is undergoing a transition from a region in which conventional hadronic degrees of freedom describe the physics to a region in which quark degrees of freedom are more appropriate.

Acknowledgments

References

[1] For a recent review, see Machleidt R and Slaus I 2001 *J. Phys. G: Nucl. Phys.* **27** R69
[2] Alexa L C *et al* 1999 *Phys. Rev. Lett.* **82** 1374
[3] Abbott D *et al* 1999 *Phys. Rev. Lett.* **82** 1379
[4] Abbott D *et al* 2000 *Phys. Rev. Lett.* **84** 5053
[5] Bochna C *et al* 1998 *Phys. Rev. Lett.* **81** 4576
[6] Wijesooriya K *et al* 2001 *Phys. Rev. Lett.* **86** 2975
[7] Schulte E *et al* 2001 *Phys. Rev. Lett.* **87** 102302
[8] Garçon M and Van Orden J W 2001 *Advances in Nucl. Phys.* **26** 293
[9] Sick I submitted to *Progress in Theoretical Physics*
[10] Buck W W and Gross F 1979 *Phys. Rev.* D **20** 2361
[11] Friar J L 1979 *Phys. Rev.* C **20** 325
[12] Lancombe M, Loiseau B, Richard J M, Vinh Mau R, Côté J, Pirès P and de Tourreil R 1980 *Phys. Rev.* C **21** 861
[13] Wiringa R B, Stoks V G J and Schiavilla R 1995 *Phys. Rev.* C **51** 38
[14] Stoks V G J, Klomp R A M, Terheggen C P F and de Swart J J 1994 *Phys. Rev.* C **49** 2950
[15] Machleidt R, Sammarruca F and Song Y 1996 *Phys. Rev.* C **53** R1483
[16] Machleidt R 2001 *Phys. Rev.* C **63** 024001
[17] Salpeter E E and Bethe H A 1951 *Phys. Rev.* **84** 1232
[18] Gross F 1969 *Phys. Rev.* **186** 1448 ; 1974 *Phys. Rev.* D **10** 223 ; 1982 *Phys. Rev.* C **26** 2203
[19] Logunov A A and Tavkhelidze A N 1963 *Nuovo Cimento* **29** 380 ; Blankenbecler R and Sugar R 1966 *Phys. Rev.* **142** 1051
[20] Phillips D R, Wallace S J, and Devine N K 1998 *Phys. Rev.* C **58** 2261
[21] Gross F, Van Orden J W and Holinde K 1992 *Phys. Rev.* C **45** 2094
[22] Stadler A and Gross F 1997 *Phys. Rev. Lett.* **78** 26
[23] Gross F 1998 *Proceedings of the Workshop on Electronuclear Physics with internal targets and the BLAST detector*, May 28–30, MIT

[24] Experimental limits on possible two photon exchange are discussed in Rekalo M P, Tomasi-Gustafsson E and Prout D 1999 *Phys. Rev.* C **60** 042202

[25] Gross F 1965 *Phys. Rev.* **136** B140

[26] Arnold R E, Carlson C E and Gross F 1980 *Phys. Rev.* C **21** 1426

[27] Donnelly T W and Raskin A S 1986 *Ann. Phys. (N.Y.)* **169** 247

[28] Jones H 1962 *Nuovo Cimento* **26** 790

[29] Jacob M and Wick G C 1959 *Ann. Phys. (N.Y.)* **7** 404

[30] Abbott D *et al* 2000 *Eur. Phys. J* A **7** 421

[31] McIntyre J A and Hofstadter R 1955 *Phys. Rev.* **98** 158

[32] Buchanan C D and Yearian R 1965 *Phys. Rev. Lett.* **15** 303

[33] Benaksas D *et al* 1966 *Phys. Rev.* **148** 1327

[34] Galster S *et al* 1971 *Nucl. Phys.* B **32** 221

[35] Ganichot D *et al* 1972 *Nucl. Phys.* A **178** 545

[36] Grossetête B, Drickey D, and Lehmann P 1966 *Phys. Rev.* **141** 1425

[37] Cramer R *et al* 1985 *Z. Phys.* C **29** 513

[38] Berard R W *et al* 1973 PLB **47** 355

[39] Simon G G *et al* 1981 *Nucl. Phys.* A **364** 285

[40] Platchkov S *et al* 1990 *Nucl. Phys.* A **510** 740

[41] Arnold R *et al* 1975 *Phys. Rev. Lett.* **35** 776

[42] Elias J E *et al* 1969 *Phys. Rev.* **177** 2075

[43] Akimov Yu K *et al* 1979 *Yad. Fiz.* **29** 649 [1979 *Sov. J. Nucl. Phys.* **29** 335]

[44] Sick I and Trautmann D 1996 *Phys. Lett.* B **375** 16 ; 1998 *Nucl. Phys.* A **637** 559

[45] Bosted P 1995 *Phys. Rev.* C **51** 409

[46] Jones M *et al* 2000 *Phys. Rev. Lett.* **84** 1398

[47] Gayou O *et al* 2001 *Phys. Rev.* C **56** 038202

[48] Gayou O *et al* to be submitted to *Phys. Rev. Lett.*

[49] Jones M private communication; Gilman R unpublished; Brash E J, Kozlov A, Li Sh, and Huber G M to be submitted to *Phys. Rev.* C

[50] Arnold R G *et al* 1987 *Phys. Rev. Lett.* **58** 1723

[51] Bosted P E *et al* 1990 *Phys. Rev.* C **42** 38

[52] Auffret S *et al* 1985 *Phys. Rev. Lett.* **54** 649

[53] Goldemberg J and Schaerf C 1964 *Phys. Rev. Lett.* **12** 298

[54] Rand R E *et al* 1967 *Phys. Rev. Lett.* **18** 469

[55] Jones E C, Bendel W L, Fagg L W and Lindgren R A 1980 *Phys. Rev.* C **21** 1162

[56] Schulze M E *et al* 1984 *Phys. Rev. Lett.* **52** 597

[57] Dmitriev V F *et al* 1985 *Phys. Lett.* B **157** 143

[58] Wojtsekhowski B B *et al* 1986 *Pis'ma Zh. Eksp. Teor. Fiz.* **43** 567 [1986 *JETP Lett.* **43** 733]

[59] Gilman R *et al* 1990 *Phys. Rev. Lett.* **65** 1733

[60] Boden B *et al* 1991 *Z. Phys.* C **49** 175

[61] The I *et al* 1991 *Phys. Rev. Lett.* **67** 173

[62] Garçon M *et al* 1994 *Phys. Rev.* C **49** 2516

[63] Popov S G *et al* 1995 *Proceedings of the 8th International Symposium on Polarization Phenomena in Nuclear Physics, Bloomington, Indiana, 1994*, AIP Conf. Proc. No. 339 (AIP, New York)

[64] Ferro-Luzzi M *et al* 1996 *Phys. Rev. Lett.* **77** 2630

[65] Bouwhuis M *et al* 1999 *Phys. Rev. Lett.* **82** 3755

[66] Nikolenko D M *et al* 2001 *Nucl. Phys.* A **684** 525c

[67] Prepost R, Simonds R M and Wiik B H 1968 *Phys. Rev. Lett.* **21** 1271

[68] Mergell P, Meissner Ulf-G and Drechsel D 1996 *Nucl. Phys.* A **596** 367

[69] Meyerhoff M *et al* 1994 *Phys. Lett.* B **327** 201 ; Eden T *et al* 1994 *Phys. Rev.* C **50** R1749 ; D. Rohe *et al* 1999 *Phys. Rev. Lett.* **83** 4257 ; Passchier I *et al* 1999 *Phys. Rev. Lett.* **82** 4988 ; Ostrick M *et al* 1999 *Phys. Rev. Lett.* **83** 276 ; Herberg C *et al* 1999 *Eur. Phys. J* A **5** 131 ;

Becker J *et al* 1999 *Eur. Phys. J* A **6** 329 ; Zhu H *et al* 2001 *Phys. Rev. Lett.* **87** 081801

[70] Bethe H A 1949 *Phys. Rev.* **76** 38

[71] Weinberg S 1990 PLB **251** 288

[72] Kaplan D B, Savage M J and Wise M B 1998 *Phys. Lett.* B **424** 390

[73] Kaplan D B, Savage M J and Wise M B 1999 *Phys. Rev.* C **59** 617

[74] Phillips D R, Rupak R, and Savage M J 2000 PLB **473** 209

[75] Phillips D R and Cohen T D 2000 *Nucl. Phys.* A **668** 45

[76] Gross F 1991 *Modern Topics in Electron Scattering* (Frois B and Sick I ed) p 219

[77] Jackson A J, Lande A and Riska D O 1975 *Phys. Lett.* B **55** 23

[78] Thompson R H and Heller H 1973 *Phys. Rev.* C **7** 2355

[79] Nyman E M and Riska D O 1986 *Proceedings of weak and electromagnetic interactions in nuclei, Heidelberg 1986* p 63

[80] Weinberg S 1995 *The Quantum Theory of Fields I* (Cambridge University Press)

[81] Simonov Yu A and Tjon J A 1993 *Ann. Phys. (N.Y.)* **228** 1 ; Nieuwenhuis T and Tjon J A 1996 *Phys. Rev. Lett.* **77** 814 ; Nieuwenhuis T 1995 Ph.D. thesis University of Utrecht; Savkli C, Tjon J A and Gross F 1999 *Phys. Rev.* C **60** 055210

[82] Keister B D and Polyzou W N 1991 *Advances in Nucl. Phys.* **20** 225

[83] Gross F and Riska D O 1987 *Phys. Rev.* C **36** 1928

[84] Tjon J A 1995 *XIVth International Conference on Few Body Problem in Physics, Williamsburg, Virginia, 1994* AIP Conf. Proc. No. 334 (AIP, New York) p 177

[85] Fleischer J and Tjon J A 1975 *Nucl. Phys.* B **84** 375 ; 1977 *Phys. Rev.* D **15** 2537 ; 1980 *Phys. Rev.* D **21** 87

[86] Hummel E and Tjon J A 1989 *Phys. Rev. Lett.* **63** 1788 ; 1990 *Phys. Rev.* C **42** 423 ; 1994 *Phys. Rev.* C **49** 21

[87] Mandelzweig V B and Wallace S J 1987 *Phys. Lett.* B **197** 469 ; Wallace S J and Mandelzweig V B 1989 *Nucl. Phys.* A **503** 673

[88] Wallace S 2001 talk at the *INT Workshop on Theories of Nuclear Forces and Few-Nucleon Systems*

[89] Van Orden J W, Devine N and Gross F 1995 *Phys. Rev. Lett.* **75** 4369

[90] Dirac P A M 1949 *Rev. Mod. Phys.* **21** 392

[91] Schiavilla R and Riska D 1991 *Phys. Rev.* C **43** 437

[92] Forest J and Schiavilla R 2001 (private communication – to be published)

[93] Schiavilla R, Pandharipande V R and Riska D O 1989 *Phys. Rev.* C **40** 2294 ; Carlson J, Riska R O, Schiavilla R and Wiringa R B 1990 *Phys. Rev.* C **42** 830

[94] Arenhövel H, Ritz F and Wilbois T 2000 *Phys. Rev.* C **61** 034002

[95] Ritz F, Göller H, Wilbois T and Arenhövel H 1997 *Phys. Rev.* C **55** 2214

[96] Krajcik R A and Foldy L L 1974 *Phys. Rev.* D **10** 1777

[97] Friar J L 1977 *Ann. Phys. (N.Y.)* **104** 380

[98] Friar J L 1980 *Phys. Rev.* C **22** 796

[99] Gross F 1978 proceedings of the *8th International Conference on Few Body Problems* (Springer-Verlag Lec. Notes in Physics #82, Zingl H *et al* ed), p. 46. [The factor $\sqrt{2}u + 2$ in Eq. (12) should read $\sqrt{2}u + w$.]

[100] Carbonell J and Karmanov V A 1999 EPJA **6** 9

[101] Karmanov V A and Smirnov A V 1992 *Nucl. Phys.* A **546** 691 ; 1994 *Nucl. Phys.* A **575** 520

[102] Carbonell J, Desplanques B, Karmanov V A and Mathiot J -F 1998 *Phys. Reports* **300** 215

[103] Machleidt R, Holinde K and Elster Ch 1987 *Phys. Reports* **149** 1

[104] Lev F M, Pace E and Salmé G 2000 PRC **62** 064004

[105] Grach I L and Kondratyuk L A 1984 *Yad. Fiz.* **39** 316 ; 1984 *Sov. J. Nucl. Phys.* **39** 198

[106] Chung P L, Coester F, Keister B D and Polyzou W N 1988 *Phys. Rev.* C **37** 2000

[107] Lev F M, Pace E and Salmé G 1998 *Nucl. Phys.* A **641** 229

[108] Lev F M, Pace E and Salmé G 1999 *Phys. Rev. Lett.* **83** 5250

[109] Allen T W, Klink W H and Polyzou W N 2001 PRC **63** 034002

[110] Maltman K and Isgur N 1983 *Phys. Rev. Lett.* **50** 1827

[111] Maltman K and Isgur N 1984 *Phys. Rev.* D **29** 952

[112] de Forest T and Mulders P J 1987 *Phys. Rev.* D **35** 2849

[113] Dijk H and Bakker B L G 1988 *Nucl. Phys.* A **494** 438

[114] Buchmann A, Yamauchi Y and Faessler A 1989 *Nucl. Phys.* A **496** 621

[115] Simonov Yu A 1981 *Phys. Lett.* B **107** 1

[116] Arndt R A *et al* 1987 *Phys. Rev.* D **35** 128

[117] Brodsky S J and Farrar G R 1973 *Phys. Rev. Lett.* **31** 1153 ; 1975 *Phys. Rev.* D **11** 1309

[118] Lepage G P and Brodsky S J 1980 *Phys. Rev.* D **22** 2157 ; Brodsky S J and Lepage G P 1981 *Phys. Rev.* D **24** 2848

[119] Isgur N and Llewellyn-Smith C 1989 *Nucl. Phys.* B **317** 526

[120] Radyushkin A V 1991 *Nucl. Phys.* A **523** 141c

[121] Farrar G R, Huleihel K and Zhang H 1995 *Phys. Rev. Lett.* **74** 650

[122] Carlson C E and Gross F 1984 *Phys. Rev. Lett.* **53** 127

[123] Brodsky S J and Hiller J R 1992 *Phys. Rev.* D **46** 2141

[124] Kobushkin A and Syamtomov A 1994 *Phys. Rev.* D **49** 1637

[125] Cao Jun and Wu Hui-fang 1997 *Phys. Rev.* C **55** 2191

[126] Carlson C E (private communication)

[127] Sick I (private communication)

[128] Ito H and Gross F 1993 *Phys. Rev. Lett.* **71** 2555

[129] Cardarelli F, Grach I L, Narodetsky I, Salme G and Simula S 1995 *Phys. Lett.* B **359** 1

[130] Petratos G G, *Deuteron and Helium Form Factor Measurments at Jefferson Lab*, contribution to the Jefferson Lab 12 GeV Upgrade; (private communication)

[131] Garçon M 1990 *Nucl. Phys.* A **508** 445c

[132] Gilman R 1988 *Jefferson Lab Workshop on Physics & Instrumentation with 6 - 12 GeV Beams* p 275

[133] Kox S (unpublished)

[134] Tomasi-Gustafsson E *et al* 1995 *Nucl. Instrum. Methods* A **366** 96

[135] Ladygin V P *et al* 1998 *Nucl. Instrum. Methods* A **3404** 129

[136] Tomasi-Gustafsson E *et al* 1999 *Nucl. Instrum. Methods* A **420** 90

[137] Arnold R E, Carlson C E and Gross F 1981 *Phys. Rev.* C **23** 363

[138] Zhou Z *et al* MIT Bates Blast experiment 00-03

[139] Raskin A S and Donnelly T W 1989 *Ann. Phys. (N.Y.)* **191** 78

[140] Dmitrasinovic V and Gross F 1989 *Phys. Rev.* C **40** 2479 ; 1991 *Phys. Rev.* C **43** 1495(E)

[141] Marchand C *et al* 1988 *Phys. Rev. Lett.* **60** 1703

[142] Jeschonnek S and Van Orden J W 2000 *Phys. Rev.* C **62** 044613

[143] De Forest T 1983 *Nucl. Phys.* A **392** 232

[144] Batiz Z and Gross F 1988 *Phys. Rev.* C **58** 2963

[145] Hoekert J, Riska D O, Gari M and Huffman A 1973 *Nucl. Phys.* **217** 14

[146] Simon G G *et al* 1979 *Nucl. Phys.* A **324** 277

[147] Bernheim M *et al* 1981 *Phys. Rev. Lett.* **46** 402

[148] Auffret S *et al* 1985 *Phys. Rev. Lett.* **55** 1362

[149] Lee K S *et al* 1991 *Phys. Rev. Lett.* **67** 2634

[150] Schmitt W M *et al* 1997 *Phys. Rev.* C **56** 1687

[151] Arnold R G *et al* 1990 *Phys. Rev.* C **42** R1

[152] Frodyma M *et al* 1993 *Phys. Rev.* C **47** 1599

[153] Mathiot J F 1984 *Nucl. Phys.* A **412** 201

[154] Leidemann W, Schmitt K-M and Arenhövel H 1990 *Phys. Rev.* C **42** R826

[155] Carlson J and Schiavilla R 1998 *Rev. Mod. Phys.* **70** 743

[156] Smejkal J, Truhlík E and Göller H 1997 *Nucl. Phys.* A **624** 655

[157] Yamauchi Y, Yamamoto R and Wakamatsu M 1984 *Phys. Lett.* B **146** 153

[158] Lu L C and Cheng T S 1996 *Phys. Lett.* B **386** 69

[159] Jourdan J, Warren G, *et al* Jefferson Lab proposal 00-103

[160] Chadwick J and Goldhaber M 1934 *Nature* **134** 237

[161] Bethe H 1999 *Rev. Mod. Phys.* **71** S6

[162] See Rossi P *et al* 1989 *Phys. Rev.* C **40** 2412 , and references therein

[163] Feld B T, Maglić B C, and Parks J 1960 *Nuovo Cimento Supp.* **10** 241

[164] John Walter and Martin Frederick V 1961 *Phys. Rev.* **124** 830

[165] Liu F F, Lundquist D E, and Wiik B H 1968 *Phys. Rev.* **165** 1478

[166] Kose R, Martin B, Runkel R, Wahlen H, and Kissler K H 1969 *Z. Phys.* **220** 305

[167] Kamae T *et al* 1977 *Phys. Rev. Lett.* **38** 468

[168] Groom D E, *et al* 2000 *Eur. Phys. J* C **15** 1

[169] Holt R J 1990 *Phys. Rev.* C **41** 2400

[170] Barannik V P *et al* 1986 *Nucl. Phys.* A **451** 751

[171] Laget J M 1978 *Nucl. Phys.* A **312** 265

[172] Leidemann W and Arenhövel H 1987 *Nucl. Phys.* A **465** 573

[173] Tanabe H and Ohta K 1989 *Phys. Rev.* C **40** 1905

[174] Lee T-S H 1992 *Few Body Syst. Supplement* **6** 526 ; Lee T-S H 1991 *Argonne National Laboratory Preprint* PHY-6886-TH-91; Lee T-S H 1991 *Argonne National Laboratory Preprint* PHY-6843-TH-91

[175] Schwamb M and Arenhövel H 2001 *Preprint* nucl-th/0105033; Schwamb M and Arenhövel H 2001 *Nucl. Phys.* A **690** 682 ; Schwamb M and Arenhövel H 2001 *Nucl. Phys.* A **690** 647 ; Schwamb M , Arenhövel H, Wilhelm P, and Wilbois Th 1998 *Phys. Lett.* B **420** 255

[176] Schwamb M, Arenhövel H, Wilhelm P 1995 *Few Body Syst.* **19** 121

[177] Kang Y, Erbs P, Pfeil W, and Rollnik H 1990 *Abstracts of the Particle and Nuclear Intersections Conference*, (MIT, Cambridge, MA); Kang Y 1993 Ph.D. thesis Bonn

[178] Nagornyi S I, Kasatkin Yu A, and Kirichenko I K 1992 *Yad. Fiz.* **55** 345 [1992 *Sov. J. Nucl. Phys.* **55** 189]

[179] Dieperink A E L and Nagornyi S I 1999 *Phys. Lett.* B **456** 9

[180] Kazakov K Yu and Shulga D V *Preprint* nucl-th/0101059.

[181] Kazakov K Yu and Shimovsky S Eh 2000 *Phys. Rev.* C **63** 014002

[182] Carlson Carl E 1990 *Nucl. Phys.* A **508** 481c

[183] Matveev V *et al* 1973 *Nuovo Cimento Lett.* **7** 719

[184] Carlson Carl E and Chachkhunashvili M 1992 *Phys. Rev.* D **45** 2555

[185] Afanasev A (private communication); Sivers D (private communication)

[186] Brodsky S J and Hiller J R 1983 *Phys. Rev.* C **28** 475 ; 1984 *Phys. Rev.* C **30** 412(E)

[187] Radyushkin A (private communication)

[188] Frankfurt L L, Miller G A, Sargsian,M M and Strikman M I 2000 *Phys. Rev. Lett.* **84** 3045

[189] Frankfurt L L, Miller G A, Sargsian M M, and Strikman M I 2000 *Nucl. Phys.* A **663** 349

[190] Kondratyuk L A *et al* 1993 *Phys. Rev.* C **48** 2491

[191] Grishina V Yu *et al* 2001 *Eur. Phys. J* A **10** 355

[192] White C *et al* 1994 *Phys. Rev.* D **49** 58

[193] von Bösch R, Lang J, Müller R, and Wölfli W 1963 *Helv. Phys. Acta* **36** 657

[194] Frederick David E 1963 *Phys. Rev.* **130** 1131

[195] Bertozzi W *et al* 1963 *Phys. Rev. Lett.* **10** 106

[196] Loeffler F J, Palfrey, Jr. T R, and White, Jr. T O 1963 *Phys. Rev.* **131** 1844

[197] Liu F F 1964 *Phys. Lett.* **11** 306

[198] Liu F F 1965 *Phys. Rev.* **138** B1443

[199] Jewell R W, John W, Sherwood J E, and White D H 1965 *Phys. Rev.* **139** B71

[200] Barbiellini G, Bernardini C, Felicetti F, and Mortas G P 1967 *Phys. Rev.* **154** 988

[201] Nath R, Firk F W K, and Schultz H L 1972 *Nucl. Phys.* A **194** 49

[202] Drooks L J 1976 Ph.D. thesis Yale University
[203] Kamae T *et al* 1978 *Nucl. Phys.* B **139** 394
[204] Ikeda H *et al* 1979 *Phys. Rev. Lett.* **42** 1321
[205] Ikeda H *et al* 1980 *Nucl. Phys.* B **172** 509
[206] Gorbenko V G *et al* 1979 *Pis'ma Zh. Eksp. Teor. Fiz.* **30** 130 [1979 *JETP Lett.* **30** 118]
[207] Gorbenko V G *et al* 1980 *Pis'ma Zh. Eksp. Teor. Fiz.* **32** 387 [1980 *JETP Lett.* **32** 362]
[208] Gorbenko V G *et al* 1981 *Pis'ma Zh. Eksp. Teor. Fiz.* **33** No.5 [1981 *JETP Lett.* **33** 297]
[209] Gorbenko V G *et al* 1982 *Yad. Fiz.* **35** 1073 [1982 *Sov. J. Nucl. Phys.* **35** 627]
[210] Gorbenko V G *et al* 1982 *Nucl. Phys.* A **381** 330
[211] Del Bianco W, Jeremie H, Irshad M, and Kajrys G 1980 *Nucl. Phys.* A **343** 121
[212] Del Bianco W *et al* 1981 *Phys. Rev. Lett.* **47** 1118
[213] Bratashevskiĭ A S *et al* 1980 *Yad. Fiz.* **31** 860 [1980 *Sov. J. Nucl. Phys.* **31** 444]
[214] Bratashevskiĭ A S *et al* 1980 *Yad. Fiz.* **32** 418 [1980 *Sov. J. Nucl. Phys.* **32** 216]
[215] Bratashevskiĭ A S *et al* 1980 *Pis'ma Zh. Eksp. Teor. Fiz.* **31** 295 [1980 *JETP Lett.* **31** 270]
[216] Bratashevskiĭ A S *et al* 1981 *Pis'ma Zh. Eksp. Teor. Fiz.* **34** 410 [1982 *JETP Lett.* **34** 389]
[217] Bratashevskiĭ A S *et al* 1982 *Pis'ma Zh. Eksp. Teor. Fiz.* **36** 174 [1982 *JETP Lett.* **36** 216]
[218] Bratashevskiĭ A S *et al* 1986 *Yad. Fiz.* **44** 960 [1986 *Sov. J. Nucl. Phys.* **44** 619]
[219] Adamian F V *et al* 1981 *Yerevan Preprint* YERE-505-48-81
[220] Ishii T *et al* 1982 *Phys. Lett.* B **110** 441
[221] Ohashi Y *et al* 1987 *Phys. Rev.* C **36** 2422
[222] Bratashevskiĭ A S *et al* 1982 *Pis'ma Zh. Eksp. Teor. Fiz.* **35** 489 [1982 *JETP Lett.* **35** 605]
[223] Bratashevskiĭ A S *et al* 1986 *Yad. Fiz.* **43** 785 [1986 *Sov. J. Nucl. Phys.* **43** 499]
[224] Ganenko V B *et al* 1992 *Z. Phys.* A **341** 205
[225] De Pascale M P *et al* 1982 *Phys. Lett.* B **114** 11
[226] De Pascale M P *et al* 1985 *Phys. Rev.* C **32** 1830
[227] Dahl Ernst A 1982 *Bonn Preprint* IR-82-26
[228] Holt R J, Stephenson K, and Specht J R 1983 *Phys. Rev. Lett.* **50** 577
[229] Barannik V P, 1983 *Yad. Fiz.* **38** 1108 [1983 *Sov. J. Nucl. Phys.* **38** 667]
[230] Althoff K H *et al* 1984 *Z. Phys.* C **26** 175
[231] Althoff K H *et al* 1989 *Z. Phys.* C **43** 375
[232] Adamian F V *et al* 1984 *Pis'ma Zh. Eksp. Teor. Fiz.* **39** 239 [1984 *JETP Lett.* **39** 286]
[233] Agababyan K Sh *et al* 1985 *Yad. Fiz.* **41** 1401 [1985 *Sov. J. Nucl. Phys.* **41** 888]
[234] Cameron J M *et al* 1984 *Phys. Lett.* B **137** 315
[235] Cameron J M *et al* 1986 *Nucl. Phys.* A **458** 637
[236] Hugi M *et al* 1987 *Nucl. Phys.* A **472** 701
[237] Vnukov I E *et al* 1986 *Pis'ma Zh. Eksp. Teor. Fiz.* **43** 510 [1986 *Sov. J. Nucl. Phys.* **43** 659]
[238] Vnukov I E *et al* 1988 *Yad. Fiz.* **47** 913 [1988 *Sov. J. Nucl. Phys.* **47** 581]
[239] Soderstrum J P and Knutson L D 1987 *Phys. Rev.* C **35** 1246
[240] Mostovoy M V *et al* 1987 *Phys. Lett.* B **189** 181
[241] Adamian F V *et al* 1988 *J. Phys. G: Nucl. Phys.* **14** 831
[242] Zybalov A A *et al* 1990 *Yad. Fiz.* **51** 23 [1990 *Sov. J. Nucl. Phys.* **51** 21]
[243] Zybalov A A *et al* 1991 *Nucl. Phys.* A **533** 642
[244] Avakyan R O *et al* 1990 *Yad. Fiz.* **52** 312 [1990 *Sov. J. Nucl. Phys.* **52** 198]
[245] Avakyan R O *et al* 1990 *Yad. Fiz.* **52** 618 [1990 *Sov. J. Nucl. Phys.* **52** 396]
[246] Fink G *et al* 1991 *Nucl. Phys.* A **530** 331
[247] Adamian F V *et al* 1991 *J. Phys. G: Nucl. Phys.* **17** 1189
[248] Blanpied G *et al* (The LEGS Collaboraton) 1991 *Phys. Rev. Lett.* **67** 1206
[249] Blanpied G *et al* (The LEGS Collaboraton) 1995 *Phys. Rev.* C **52** R455
[250] Blanpied G *et al* (The LEGS Collaboraton) 1999 *Phys. Rev.* C **61** 024604 ; we use the net results
       of LEGS data release L1-3.0 (March 1994)
[251] Mishnev S I *et al* 1993 *Phys. Lett.* B **302** 23

[252] Pate S *et al* 1993 *Phys. Rev. Lett.* **70** 3205
[253] Tuccillo M *et al* 1994 *Nucl. Phys.* A **580** 253
[254] Wartenberg S *et al* 1999 *Few Body Syst.* **26** 213
[255] Adamian F *et al* 2000 *Eur. Phys. J* A **8** 423
[256] Crawford R *et al* 1996 *Nucl. Phys.* A **603** 303
[257] Dougan P *et al* 1976 *Z. Phys.* A **276** 55
[258] Althoff *et al* 1983 *Z. Phys.* C **21** 149
[259] Arends J *et al* 1984 *Nucl. Phys.* A **412** 509
[260] Tiator L and Wright L E 1982 *Nucl. Phys.* A **379** 407 ; Wright L E and Tiator L 1982 *Phys. Rev.* C **26** 2349
[261] Matthews J L and Owens R O 1973 *Nucl. Instrum. Methods* **111** 157
[262] Napolitano J *et al* 1988 *Phys. Rev. Lett.* **61** 2530
[263] Freedman S J *et al* 1993 *Phys. Rev.* C **48** 1864
[264] Belz J E *et al* 1995 *Phys. Rev. Lett.* **74** 646
[265] Myers H *et al* 1961 *Phys. Rev.* **121** 630
[266] Ching R and Schaerf C 1966 *Phys. Rev.* **141** 1320
[267] Baba K *et al* 1983 *Phys. Rev.* C **28** 286
[268] Rossi P, De Sanctis E, *et al* JLab proposal E93-017
[269] Gilman R, Holt R, Meziani Z E *et al* Jefferson Lab proposal E99-008; Schulte E *et al* to be published
[270] Sargsian M (private communication)
[271] Afanasev A and Radyushkin A (private communication)
[272] LeRose J *et al* (unpublished)